Technische Universität Dortmund
Fakultät für Chemie

Dissertation
zur Erlangung des akademischen Grades eines
Doktors der Naturwissenschaften

Dynamic chromatin association of RCC1 during the cell cycle

Martin Bierbaum

30. Mai 2011

1. Gutachter: Prof. Dr. Philippe Bastiaens
2. Gutachter: Prof. Dr. Alfred Wittinghofer

Erklärung

Ich versichere hiermit, dass ich die vorliegende Dissertation selbstständig und ohne unzulässige fremde Hilfe erbracht habe. Ich habe keine anderen als die angegebenen Quellen und Hilfsmittel benutzt, sowie wörtliche und sinngemäße Zitate kenntlich gemacht.

Dortmund, 30. Mai 2011

Contents

1 Introduction

The cell is the fundamental unit that is capable of carrying out the defining functions of life. Cells in multicellular organisms as well as groups of unicellular organisms can organize into complex structures. At the same time, each cell needs to organize its components into elaborate subcellular structures such as cellular organelles. The morphogenesis of such μm-sized subcellular structures depends on the assembly of complexes from nm-sized biomolecules. Despite their stability, subcellular structures are in constant flux on level of their building blocks, whose interactions are highly dynamic. Cellular structure therefore needs to be maintained in a dynamic equilibrium by constant energy dissipation.

The dynamic interaction of biomolecules needs to be regulated and coordinated in space and in time. One example for a system the cell uses to achieve this is controlled by the small G-protein Ran. Ran is a soluble protein that is found throughout the entire cell, however, the activity of Ran is spatially regulated such that there is a high concentration of active Ran close to chromatin. This spatial distribution of active Ran is referred to as the "Ran gradient", and is essential for processes such as nucleocytoplasmatic transport, mitotic spindle assembly, and nuclear envelope formation.

Two enzymes determine the activity of Ran: Regulator of Chromosome Condensation 1 (RCC1) activates Ran, and Ran GTPase activating protein (RanGAP) induces its inactivation. By binding to chromatin, RCC1 is spatially partitioned from RanGAP, which is localized away from chromatin. This partitioning of enzyme activities is essential to create the Ran gradient at various stages of the cell cycle. For the stable generation of the Ran gradient, the steady state concentration of RCC1 on chromatin needs to be higher than its concentration in the cytoplasm. During interphase, this is ensured by active transport of RCC1 into the nucleus and its retention by the nuclear envelope. Chromatin binding is therefore theoretically dispensable for RCC1 localization during interphase. During mitosis, however, chromatin binding is essential to ensure proper enzyme partitioning as there is no active transport mechanism and no nuclear envelope to sequester RCC1 on chromatin anymore. Thus, it is an interesting question whether chromatin affinity of RCC1 is regulated during the cell cycle. An increased chromatin affinity could play an important role in maintaining the chromosomal localization of RCC1 during mitosis.

Chromatin binding does not only guarantee correct localization during mitosis but might also influence the enzymatic properties of RCC1 itself. Several observations suggest that the complex of Ran and RCC1 binds to chromatin, and that the activation of Ran is coupled to chromatin. This opens the possibility that the residence time of RCC1 on chromatin is an important kinetic parameter of the reaction between RCC1 and Ran. Consequently, the activation level of Ran might be controlled by regulation of RCC1's chromatin affinity at different stages of the cell cycle.

In this thesis, my aim is to determine whether the chromatin binding properties of RCC1 differ at different stages of the cell cycle. Furthermore, I intend to analyze whether chromatin binding and the activation of Ran by RCC1 are linked mechanistically. This requires a method, which is capable of measuring chromatin binding of RCC1 in living cells. Fluorescence recovery after photobleaching (FRAP) measurements and closely related photoactivation measurements have been used to measure chromatin binding of several proteins. However, the analysis of such measurements usually assumes a simplified geometry, which is not given in mitotic cells. Consequently, these measurements are not ideal to compare chromatin binding in interphase and mitotic cells. Furthermore, these methods have a limited temporal resolution, making it difficult to resolve fast processes such as diffusion and highly transient binding interactions. Therefore, I attempt to establish fluorescence correlation spectroscopy (FCS) as a method to measure chromatin binding of fluorescently labelled RCC1 in living cells. Initial experiments suggested that binding interactions between RCC1 and chromatin contribute to RCC1 mobility and to the shape of FCS measurements. To analyze FCS data quantitatively, I develop a model that describes FCS measurements as a function of diffusion of RCC1 and its binding to chromatin and that allows to determine the underlying biophysical parameters by curve fitting.

This thesis is divided into five major parts. Chapter 2 gives a summary of the current knowledge about the biochemistry and cell biology of the Ran system and describes the basics of FRAP and FCS. Chapter 3 describes the binding diffusion model for FCS experiments. Chapter 4 presents experiments that study the mobility of RCC1 during interphase and mitosis with the aim of characterizing chromatin binding at those stages of the cell cycle. Furthermore, measurements of the mobility of Ran and the interactions of Ran and RCC1 are presented, which test the hypothesis that both proteins interact on chromatin. A discussion of the experimental results is given in chapter 5. Finally, a detailed description of the experimental methods follows in chapter 6.

2 Background

2.1 Ran

The small G-protein Ran is involved in the regulation of nucleocytoplasmic transport, mitotic spindle assembly, and nuclear envelope assembly, three prominent morphogenetic processes that are essential for all eukaryotic cell types. The common feature of these processes is that they all require the cell to identify and locate its chromatin. In nucleocytoplasmic transport, the cytoplasm needs to be distinguished from the chromatin-containing nucleus. In mitotic spindle assembly and nuclear envelope formation, cytoskeletal and membrane structures need to be assembled specifically around chromatin. In these processes, Ran acts as a signal transducer between chromatin and the cell by spatially organizing biochemical reactions around chromatin.

2.1.1 Biochemistry of Ran

Ran belongs to the family of small guanine nucleotide binding proteins (small G-proteins) and shares the biochemical properties that are characteristic for this family of proteins (reviewed in [1, 2]). Small G-proteins bind either guanosine triphosphate (GTP) or guanosine diphosphate (GDP) and have the intrinsic capacity to hydrolyse GTP to GDP, which is why they are sometimes referred to as small guanosine triphosphate hydrolases (GTPases). This nomenclature is, however, controversial since the intrinsic GTPase activity of most small G-proteins is very low ($5 \cdot 10^{-5}\,\mathrm{s}^{-1}$ in the case of Ran) and the ability to bind guanine nucleotides is therefore considered as their most significant property. Hence, I will use the term small G-protein.

Depending on their nucleotide binding state, small G-proteins adopt different conformations. In the GTP-bound state, also called the active state, small G-proteins interact specifically with so-called effector proteins. Through the interaction with effector proteins, small G-proteins influence numerous cellular processes including the control of cell growth and division (Ras-family of small G-proteins), endocytosis (Rab-family), vesicular transport (Arf-family), and the regulation of the cytoskeleton (Rho-family).

Because of this nucleotide-dependent property, small G-proteins are considered to be molecular switches. The transition from one nucleotide binding

state to the other occurs either by exchange of bound GDP to GTP or by hydrolysis of bound GTP to GDP, respectively. The intrinsic rates of both reactions are very low, therefore small G-proteins require accessory enzymes to catalyse the transitions. Guanine nucleotide exchange factors (GEFs) catalyse the nucleotide exchange and GTPase activating proteins (GAPs) stimulate GTP hydrolysis. In the case of Ran, the GAP function is carried out by the protein RanGAP, while the GEF function is fulfilled by Regulator of Chromosome Condensation 1 (RCC1) [3–6]. Binding of Ran to RCC1 or RanGAP causes a 10^5-fold increase in the rate of each respective reaction [7]. Due to the counteracting activities of GEFs and GAPs, small G-proteins constantly cycle between active and inactive states. The reaction system comprising a G-protein, a GEF, and a GAP therefore is referred to as a GTPase cycle.

The GTPase cycle can be interrupted by specific mutations in Ran [7]. The mutation Q69L removes a glutamine in the active site of Ran and renders Ran unable to hydrolyse GTP. Consequently, RanQ69L is in a constitutively active state. On the other hand, the mutation T24N reduces the nucleotide affinity of Ran. The nucleotide-free RanT24N forms a high-affinity complex with RCC1 that acts as a dominant inhibitor of Ran activation.

The GTPase stimulating effect of RanGAP can be further enhanced by Ran-binding protein 1 (RanBP1) and Ran-binding protein 2 (RanBP2) [8, 9]. The former is a soluble protein while the latter is a component of the nuclear pore complex. Both proteins are also classified as Ran effectors that are involved in the controlled release of nuclear cargo (see below).

RanGAP and RCC1 are spatially partitioned in cells. By covalent conjugation to the small ubiquitin-like modifier protein (SUMO), the normally cytoplasmic RanGAP is recruited to the cytoplasmic side of the nuclear pore complex during interphase and to the mitotic spindle during mitosis [10, 11]. In contrast, RCC1 is localized to chromatin during interphase and mitosis [12]. The spatial partitioning of these two enzymes is crucial for the cellular roles of Ran, as it results in a depletion of active Ran in the cytoplasm and an accumulation of active Ran close to chromatin. This asymmetric distribution of active Ran is referred to as the Ran gradient. In this context, it is important to note that Ran is not associated with lipid membranes by lipophilic post-translational modifications, in contrast to various other members of the family of small G-proteins. Instead, Ran is a soluble protein whose ability to diffuse freely is crucial for generation of the Ran gradient.

2.1.2 Cellular processes regulated by Ran

Nuclear transport

Eukaryotic cells are characterized by a cell nucleus that contains the cell's genome and spatially separates DNA replication and transcription from protein synthesis. This compartmentalization of processes endows the cell with an additional layer of regulation for processes such as gene expression or signal transduction. The nuclear and cytoplasmic compartments are separated by the nuclear envelope (NE), a double membrane that is continuous with the endoplasmic reticulum (ER). Transport of molecules across the nuclear envelope occurs through nuclear pore complexes (NPCs) (recently reviewed in [13–15]).

NPCs are large multiprotein assemblies located at sites where the inner and outer membrane of the NE join together. In cryo electron microscopy, the NPC appears as a ring-like structure consisting of eight radially arranged spokes. The ring has a diameter of approximately 125 nm and encircles a central opening with a minimum diameter of approximately 35 nm [16–18]. NPCs consist of multiple copies of approximately 30 different proteins, collectively referred to as nucleoporins (Nups), totaling a molecular mass of approximately 50 MDa for the central spokes [19, 20]. Several subgroups of Nups are distinguished, depending on their structure and location within the NPC. The FG Nups (phenyl-glycine rich nucleoporins) are a subgroup of Nups containing phenyl-glycine repeats connected by hydrophilic linker sequences. FG Nups line the walls of the NPC and fill the pore with a dense array of their unstructured FG repeat regions [21, 22]. The array of FG repeats has hydrogel-like properties and is thought to act as a selective permeability barrier, which restricts passage of molecules above a certain size [23–27]. Molecules up to a size of approximately 40 kDa can pass the NPC by passive diffusion [28–30]. Molecules above that size need to bind to specific transport receptor proteins (NTRs) that interact with the FG repeats inside the pore to mediate transport of their cargo through the NPC [31, 32]. Importantly, movement of NTRs and their cargo within the nuclear pore is energy-independent, bidirectional, and not inherently biased towards the nucleus or the cytoplasm [33].

A variety of NTRs exist, yielding a large number of cargo-specific transport pathways. This offers the possibility to regulate nuclear transport for each cargo or a subgroup of cargo proteins independently. With more than 20 members in higher eukaryotes, the karyopherin family constitutes the majority of all known NTRs and is responsible for the transport of a large number of different cargo molecules (reviewed in [13]). A well studied representative of this family is the karyopherin importin β, which mediates import of its cargo

into the nucleus [34]. Cargo recognized by importin β contains a nuclear localisation signal (NLS) consisting of one or two clusters of four to five basic amino acid sequences. Depending on the number of basic clusters, monopartite and bipartite NLS are distinguished [35, 36]. Importin β usually does not bind to the NLS directly but requires the adapter protein importin α to do so [37]. Multiple isoforms of importin α exist, thus increasing the number of different importin β dependent import pathways [38].

Directionality of nuclear transport is achieved by differential regulation of cargo binding and release on the two sides of the nuclear pore (figure 2.1). Active Ran regulates the cargo binding properties of karyopherins [39]. Karyopherins of the importin subfamily release their cargo upon Ran binding, which results in a retention of importin cargos in the nucleus due to the high nuclear concentration of active Ran [40]. The complex of importin β and active Ran can translocate back to the cytoplasm, where it is dissociated by RanBP1, terminating the import process [41]. Conversely, karyopherins of the exportin family require active Ran to bind their cargo, forming a trimeric complex with Ran and the cargo. Inactivation of Ran outside of the nucleus leads to a release of exportin cargo into the cytoplasm [42]. The export process is terminated by RanBP1- and RanBP2-dependent dissociation of export complexes from the NPC [43]. GDP-bound Ran can relocalize to the nucleus by binding to the small nuclear transport factor 2 (NTF2/p10), thus completing one transport cycle [44, 45].

To conclude, the asymmetric distribution of active Ran confers directionality to nuclear transport. Ran controls transport directionality by modulating the cargo binding affinity of nuclear transport factors. Repeated cycles of GTP hydrolysis are required to maintain the asymmetric distribution of active Ran. Therefore, GTP hydrolysis indirectly provides the energy needed to concentrate cargo in either the nuclear or the cytoplasmic compartment.

Mitotic spindle assembly

The mitotic spindle is a bipolar array of microtubules (MTs) that assembles during cell division and is responsible for distributing duplicated chromosomes onto the two daughter cells. Spindle MTs attach to the centromere regions of the chromosomes via multiprotein complexes known as kinetochores. Specialized organelles, referred to as microtubule organizing centres (MTOC) or centrosomes, form the base of the spindle poles in most but not all cell types (for reviews of spindle structure, see [46–48]).

Spindle assembly relies on a reorganization of the MT cytoskeleton during mitosis. MTs are dynamic filaments that can switch between phases of growth

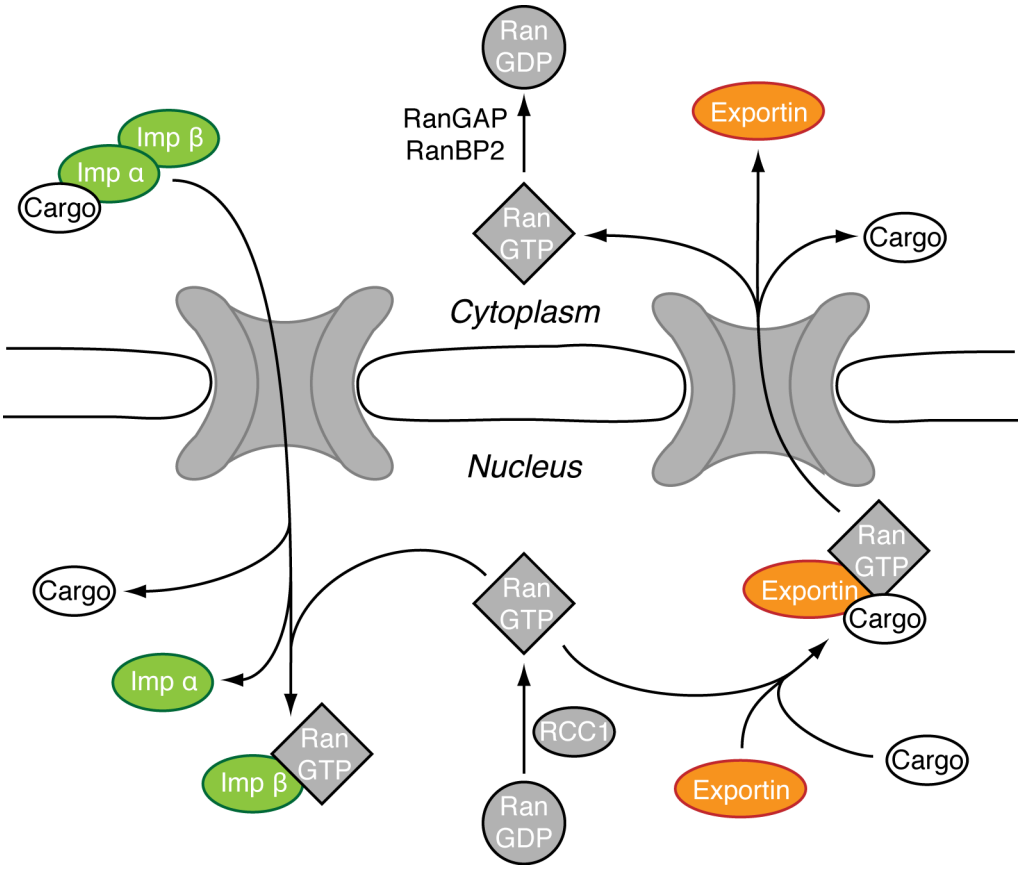

Figure 2.1: Ran imposes directionality on nuclear transport by regulating cargo binding of karyopherins. Cargo destined for the nucleus binds to specific NTFs in the cytoplasm (shown here for the importin α/β complex) and translocates through the NPC. In the nucleus the cargo-importin complex is dissociated by binding of GTP-bound Ran to importin β. In the nucleus, GTP-bound Ran forms a trimeric complex with exportins and cargo destined for the cytoplasm. After translocation through the NPC, Ran is inactivated by RanGAP, which results in the dissociation of the cargo-exportin-Ran complex. The asymmetric distribution of GTP-bound Ran between nucleus and cytoplasm is maintained by the partitioning of RanGAP and RCC1 between the two compartments. NTF2-mediated import of GDP-bound Ran has been omitted for clarity.

and shrinkage [49]. During mitosis, the transition frequency from growth to shrinkage is increased, rendering MTs more dynamic and facilitating the quick rearrangement of MT architecture. Two pathways of spindle assembly can be distinguished: In the centrosome dependent pathway, each of the two centrosomes nucleates an aster of MTs, which dynamically search the cytoplasm until they eventually are stabilized by attaching to kinetochores. This mechanism is referred to as the "search and capture" model of spindle assembly [50]. In the chromatin dependent pathway, MTs are nucleated in the vicinity of chromatin and subsequently attach to kinetochores, where they continue to polymerize and eventually get incorporated into the bipolar spindle array [51–54]. Chromatin has an active role in both pathways by promoting MT nucleation and stability in its vicinity. This biases the growth of centrosome-nucleated MTs towards kinetochores, and induces spindle assembly in cells and cell extracts lacking centrosomes [51, 55].

Ran is a mediator of the effect of chromatin on MT dynamics. This was first demonstrated in *Xenopus laevis* egg extracts, where addition of active Ran induces spindle assembly by modulating MT dynamics [56–61]. Due to the partitioning of RanGAP and RCC1, a concentration gradient of active Ran surrounds chromatin, as has been demonstrated in *X. laevis* egg extracts and mitotic HeLa cells [62–64]. This gradient is thought to regulate MT dynamics as a function of distance to chromatin.

The interaction of active Ran with importins in the mitotic cytoplasm is thought to release spindle assembly factors (SAFs) that are normally inactivated by binding to importins (figure 2.2). SAFs released from importins locally modulate MT dynamics [65, 66]. Interestingly, the Ran-importin β complex is distributed in a gradient that extends further from chromatin than the gradient of active Ran alone, possibly explaining the long-range effect of chromatin on MT stabilization [63].

The currently best studied example for a SAF is the MT associated protein TPX2, which has multiple functions in spindle assembly. First, TPX2 controls MT dynamics by promoting the nucleation of new filaments and by bundling existing filaments [67]. Second, TPX2 regulates the mitotic kinase Aurora A, which phosphorylates multiple targets in the mitotic spindle. TPX2 is required to localize Aurora A to the mitotic spindle, acts as a coactivator in the autocatalytic activation of Aurora A, and protects Aurora A from proteolytic degradation [68–72]. Both functions are inhibited by binding of TPX2 to importin α and β, making TPX2 a target of Ran regulation during mitosis [73–75]. Another SAF regulated by binding to importins is the cyclin-dependent kinase 11 (Cdk11), which stabilizes MTs in a Ran-dependent manner [76].

Ran also uses exportins as effectors to locally assemble protein complexes.

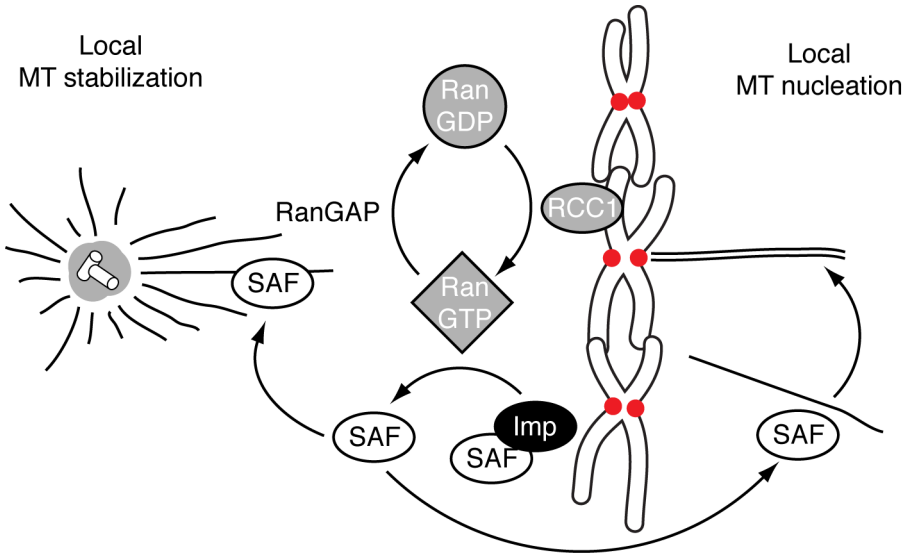

Figure 2.2: Model for the role of Ran in mitotic spindle assembly. Due to the partitioning of RCC1 and RanGAP, GTP-bound Ran is distributed in a concentration gradient around chromatin. This results in the localized release of SAFs from importins (Imp). SAFs either promote spindle assembly through local stabilization of centrosome-nucleated MTs (as shown to the right) or through localized nucleation of new MTs (as shown to the left), which subsequently attach to the kinetochores (red dots).

For example, Ran recruits the exportin Crm1 to kinetochores, which contributes to the attachment of MTs to kinetochores. Recruitment of Crm1 results in the localisation of RanGAP and RanBP2 at kinetochores. However, the reason why active Ran recruits its own negative regulator is not clear [77].

Spindle assembly is commonly seen as an example of self-organisation, i.e. the energy-dependent assembly of an ordered structure independent of a template [78]. Self-organisation strictly requires energy dissipation, which is provided in the form of GTP or ATP hydrolysis by Ran, microtubules, and motor proteins. In this context, the Ran gradient generates structure by promoting certain biochemical reactions in a manner that is dependent on the distance to chromatin. The Ran gradient during mitosis can be regarded as a way of compartmentalizing the cytoplasm around chromatin without the need for a nuclear envelope.

Nuclear envelope assembly

At the onset of mitosis, during the transition from prophase to prometaphase, the nuclear envelope breaks down and its components dissolve into the ER membrane network. After chromosome segregation, a new NE has to be assembled around the chromatin of each daughter cell (reviewed in [79]).

An early step in NE reassembly is the coating of chromosomes with an ER-like membrane network, which happens as early as anaphase, i.e. shortly after the duplicated chromosomes have started to segregate [80, 81]. Reconstitution of this process in *X. laevis* egg extracts has demonstrated a requirement for Ran and importin β. Ran-coated beads can replace chromatin and serve as a seed for NE assembly, a process that is inhibited by excess amounts of importin β [82–84].

Two mechanisms of how Ran controls assembly of the NE and particularly of the NPC have been studied. First Ran induces NE assembly by dissociating complexes between importin β and certain Nups, similar to its mechanism in nuclear transport and spindle assembly [85]. This enables the Nups to associate with chromatin, where they induce NPC assembly. The association of Nups and importin β in this case requires importin α as an adapter and occurs via a NLS on the Nup. The second mechanism is independent of this cargo-like binding to importin α, but seems to require the interaction of importin β with the FG-repeats of FG Nups [84]. This suggests that chromatin-bound Ran is needed to recruit complexes of importin β and FG Nups to the sites of NPC assembly.

An interesting aspect of Ran's role in NE assembly seems to be that Ran does not act as a diffusible molecule but locally on chromatin in contrast to its role in nuclear transport and spindle assembly. It remains an open question whether a switch from a gradient-like to a localized distribution of active Ran occurs at the time of NE assembly and how it is regulated.

2.2 RCC1

RCC1 was first identified in the *ts*BN2 hamster cell line. This cell line has a serine to phenylalanine mutation in RCC1, which results in the degradation of RCC1 at elevated temperatures (39.5 – 40°C) [86]. As *ts*BN2 cells exhibit premature chromosome condensation at the non-permissive temperature, it was originally thought that RCC1 was directly involved in the regulation of chromosome condensation, hence its name [87]. Later, it was demonstrated that RCC1 catalyses nucleotide exchange of Ran [3]. Premature chromosome condensation following the loss of RCC1 is in fact a consequence of premature

activation of the CDK1/cyclin B kinase [88, 89]. Although the exact mechanism of this misregulation is unknown, it most likely is caused by defects in nuclear transport that necessarily occur when RCC1 is depleted [90].

2.2.1 Structure and mechanism

Structurally, RCC1 has a seven-bladed propeller fold, in which seven sequence repeats of a length of 50-60 amino acids each form seven four-stranded antiparallel β-sheets that are arranged in a propeller like fashion (see figure 2.3). This fold gives the protein a very compact structure, from which only the flexible N-terminal tail sticks out [91]. RCC1 is a member of a subfamily of structurally related proteins characterized by RCC1-like sequence repeats that can be found in both prokaryotic and eukaryotic genomes [92]. In human cells, at least three isoforms of RCC1 are expressed, named RCC1 α, β, and γ, and ranging in length from 421 to 452 amino acid residues. These isoforms differ in the length of their N-terminal tail, which varies from 24 amino acid residues (RCC1 α) to 55 amino acid residues (RCC1 β). The different isoforms are probably generated by alternative mRNA splicing [93].

The nucleotide exchange reaction between RCC1 and Ran is described by a four-step mechanism involving the initial formation of a ternary complex of nucleotide-bound Ran and RCC1, which relaxes into a binary complex of Ran and RCC1 by nucleotide dissociation. The binary complex can be converted into a ternary complex again by association of a new nucleotide. Dissociation of nucleotide-bound Ran and RCC1 completes the reaction [94]. In contrast to other small G-proteins and their respective GEFs, the ternary complex of GDP- or GTP-bound Ran and RCC1 is relatively stable with a dissociation constant of approximately $1\,\mu$M. It has, however, a reduced affinity for nucleotides compared to Ran alone and is therefore readily converted into the binary complex. In fact, binding of RCC1 to nucleotide-bound Ran increases the nucleotide dissociation rate from $10^{-5}\,\mathrm{s}^{-1}$ to $21\,\mathrm{s}^{-1}$ in the case of GDP and from $10^{-4}\,\mathrm{s}^{-1}$ to $19\,\mathrm{s}^{-1}$ in the case of GTP. It is noteworthy that the exchange reaction is not inherently biased towards generation of GTP-bound Ran. In fact, Ran has a 10-fold higher affinity for GDP than for GTP. Production of GTP-bound Ran is purely a consequence of the excess concentration of GTP in cells.

RCC1 interacts with Ran through one face of its β propeller structure, and facilitates nucleotide dissociation from Ran by pushing aside the P loop, which is required to bind the phosphates on the nucleotide [5]. Because of overlapping binding sites on Ran, RCC1 competes with other Ran binding proteins such as RanBP1-related proteins and NTF2. Consequently, RanBP1 inhibits RCC1

catalyzed nucleotide exchange on Ran [8]. It is therefore possible that Ran activation by RCC1 is modulated by RanBP1-related proteins *in vivo*.

2.2.2 Nuclear import

RCC1 accumulates in the nucleus during interphase. This occurs via two different mechanisms. First, RCC1 contains a bipartite NLS in its N-terminal tail, which enables it to specifically bind to the importin α3 isoform [95, 96]. As a result, RCC1 is imported into the nucleus by an importin and Ran-dependent mechanism and stimulates its own import by activating Ran in the nucleus. Second, RCC1 also enters and accumulates in the nucleus if its NLS is removed. Passage of a truncated RCC1 through the NPC does not require its binding to importins but presumably involves interactions between RCC1 and Nups. Nuclear accumulation of truncated RCC1 is probably driven by its chromatin binding [97].

Binding of RCC1 to importin α3 is modulated by the length of the N-terminal tail and by N-terminal phosphorylation. RCC1 is phosphorylated on serine 11 and possibly also on serine 2 by the CDK1/cyclin B kinase during mitosis [98, 99]. Phosphorylation does not affect RCC1's catalytic activity, but reduces its affinity for importin α3. RCC1 γ is the isoform that is most strongly phosphorylated. Consequently, RCC1 γ has a reduced affinity for importin α3 as compared to the short isoform RCC1 α [93]. The functional significance of the cell-cycle dependent regulation of importin binding is not clear, although it has been argued that it affects binding of RCC1 to chromatin (see below).

2.2.3 Chromatin binding

The atomic structure of a crystallized complex of RCC1 and a nucleosome core particle shows that RCC1 binds to chromatin by directly interacting with DNA and histones (figure 2.3) [100]. The nucleosome core particle comprises approximately 145 base pairs of DNA wrapped around an octamer of histone proteins. The histone octamer consists of two copies each of the core histone proteins H2A, H2B, H3 and H4 [101]. RCC1 uses two loops of one of its β sheets to bind an acidic patch on the histone H2A/H2B dimer, and interacts with nucleosomal DNA through one of those loops and its N-terminal tail. This mode of interaction is consistent with previous biochemical data that showed that DNA binding requires the N-terminal tail, histone binding occurs independently of the N-terminal tail of RCC1, and that binding of RCC1 does not require the N-terminal tails of the histones [102, 103]. In contrast to an older model of chromatin binding, RCC1 does not interact with chromatin

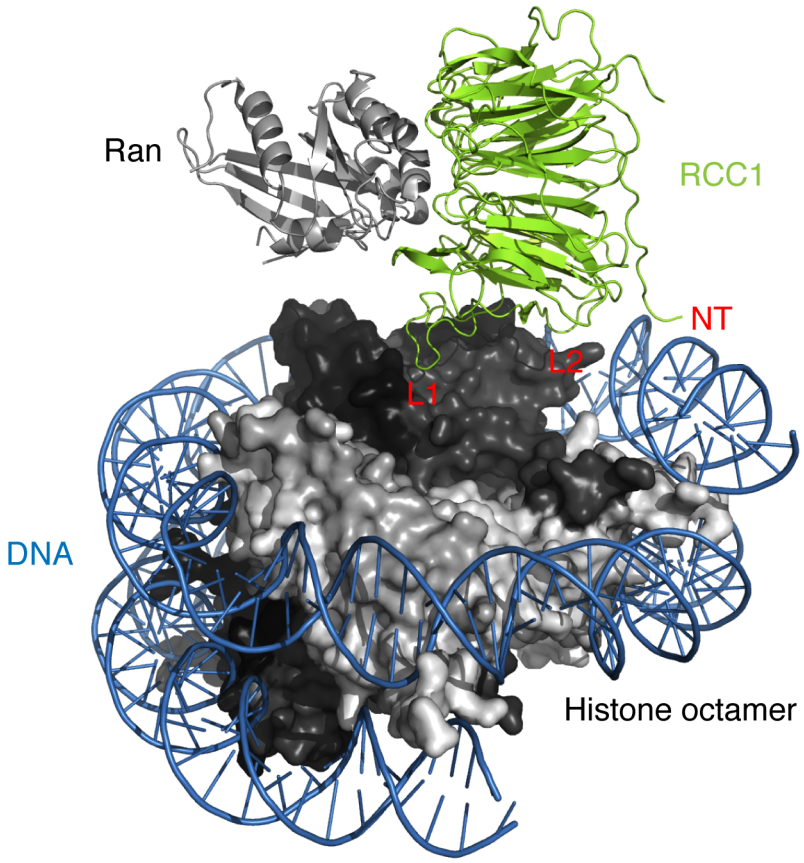

Figure 2.3: Model of the Ran-RCC1 complex bound to a nucleosome core particle. This model is generated by aligning the RCC1 structures in the structure of the Ran-RCC1 complex (PDB code 1I2M) and the structure of the RCC1-nucleosome complex (PDB code 3MVD) [5, 100]. Ran and RCC1 are shown as a cartoon representations in light grey and green, respectively. The three sites at which RCC1 interacts with the nucleosome are labelled red. L1 and L2 are the two loops that interact with histones H2A/H2B and DNA. NT is the N-terminal DNA binding region. The histone octamer is shown as a surface representation with the H2A/H2B dimers in dark grey and the H3/H4 dimers in light grey. DNA is shown in blue.

through one face of its β propeller structure such that the Ran and chromatin interaction sites would be opposite of each other. Instead, the RCC1 propeller wheel sits perpendicular to the nucleosome histone face, possibly allowing Ran to contact both RCC1 and the nucleosome.

Human RCC1 is methylated on the α-amino group of its N-terminal serine residue. The methylation occurs after cleavage of the N-terminal methionine and requires proline and lysine residues at positions 3 and 4, respectively. RCC1 mutants that cannot be methylated bind less strongly to chromatin, indicating that methylation contributes to the interaction between the N-terminal tail and nucleosomal DNA [104]. The enzyme responsible for methylation has been identified in HeLa cells and has been named N-terminal RCC1 methyltransferase (NRMT). NRMT accumulates in the nucleus during interphase and methylates at least five other targets [105].

Importin binding and N-terminal phosphorylation are also thought to affect chromatin binding of RCC1. The importin $\beta/\alpha 3$ dimer can compete with chromatin binding of RCC1 [93]. Competition between importin binding and chromatin binding could potentially lead to mislocalization of RCC1 during mitosis. The inhibition of the importin interaction by mitosis-specific phosphorylation might therefore be a way to ensure the correct localisation of RCC1 [98, 99]. It has also been suggested that phosphorylation modulates the binding to chromatin directly. However, the exact effect remains disputed. According to Hutchins *et al.* phosphorylation ensures that RCC1 retains a dynamic binding to chromatin during mitosis rather than a stable, immobile binding [98]. On the other hand, Li and Zheng have suggested that phosphorylation results in a more stable binding to chromatin [99].

Regulation of RCC1 by chromatin binding

The major function of chromatin binding is to ensure the correct localization of RCC1, especially during mitosis. Consequently, mislocalization of RCC1 by interference with its chromatin binding ability causes a misregulation of the Ran system and results in defects in spindle assembly [106]. However, chromatin binding might also influence the enzymatic activity of RCC1 directly. This is suggested by measurements with purified proteins, which show that addition of purified core nucleosomes or histones H2A/H2B stimulates the catalytic activity of RCC1 by a twofold increase in the nucleotide dissociation rate [103]. Because this effect is relatively small compared to the 10^5-fold increase caused by RCC1 alone, it is unclear whether it has physiological relevance.

Li *et al.* have argued that the nucleotide exchange reaction is coupled to chromatin by binding of the binary complex of Ran and RCC1 to chromatin

[107]. This model is supported by the observation that the nucleotide-free RanT24N accumulates on chromatin and microinjection of excess RanT24N causes a reduced mobility of RCC1 in nuclei. Consistent with this model, it has also been shown that Ran binds to chromatin via the histones H3/H4 [108].

Recruitment of the binary complex to chromatin suggests that the chromatin affinity of RCC1 is an important parameter of the nucleotide exchange reaction. An indication that the residence time of RCC1 on chromatin affects its catalytic activity comes from a study of RCC1 mobility during early stages of apoptosis [109]. Here, induction of apoptosis in HeLa cells causes phosphorylation of histone H2B and results in a reduction of the mobility of RCC1 on chromatin. This correlates with a reduction in the levels of active Ran and an eventual breakdown of the Ran gradient during apoptosis.

2.3 Methods to measure protein mobility

The microscopic imaging of cells expressing fluorescently-tagged proteins allows to study the localisation of these proteins with subcellular resolution. However, conventional imaging techniques only give information about the steady-state distribution of proteins because they lack the spatial and temporal resolution to follow the movement of individual molecules. In the following section, I will discuss two fluorescence microscopy based techniques that are commonly used to acquire information about the mobility of biomolecules in living cells.

2.3.1 Fluorescence recovery after photobleaching

Fluorescence recovery after photobleaching (FRAP) exploits the limited photostability of fluorophores. By applying a high dose of excitation light, fluorophores are photobleached, i.e. they are irreversibly rendered nonfluorescent, in a selected area of a sample. This effectively perturbs the steady-state distribution of visible fluorophores. After the photobleaching pulse the relaxation of the distribution of visible fluorophores back into the steady-state is observed by time-lapse imaging. The relaxation kinetics are usually determined by measuring the fluorescence recovery in the bleached area. The recovery kinetics of fluorescently tagged proteins in living cells are mainly dependent on diffusion, specific binding interactions with other components of the cell, the spatial distribution of the observed protein, and the geometry of the bleached area.

By fitting a model based on the diffusion equation to the recovery kinetics, FRAP measurements can be used quantitatively to estimate an effective diffusion constant [110]. This approach has for example been used to analyse the

mobility of nuclear proteins involved in transcription and splicing [111]. Models for the analysis of binding reactions and diffusion have also been presented and have been applied to measure the dynamics of the interaction between transcription factors and chromatin [112, 113]. These models, however, assume a distribution of binding sites that is cylindrically symmetric with respect to the bleached area. This is for example given in the case of chromatin during interphase, which is (as a first approximation) homogeneously distributed in the nucleus, and a circular bleached area that is small compared to the size of the nucleus. The assumption is not valid during mitosis, where chromatin is concentrated in the metaphase plate. Consequently, quantitative FRAP measurements of chromatin binding have only been performed in interphase nuclei.

The steady-state distribution of fluorophores can also be perturbed by the use of photoactivatable fluorophores, for example the photoactivatable variant of green fluorescent protein (paGFP) [114]. This approach has been utilized to study the nuclear mobility of RCC1 and several other chromatin-binding proteins [115]. This demonstrated that 98 % of all RCC1 molecules are bound to chromatin in steady-state and that chromatin binding of RCC1 is transient with a dissociation rate constant of $> 0.15\,\mathrm{s}^{-1}$. However, despite the fact that this study also took into account the inhomogeneous distribution of binding sites, it was only conducted in interphase cells. Due to the limited temporal resolution of confocal imaging, it was also only possible to determine a lower limit of the dissociation rate constant.

2.3.2 Fluorescence correlation spectroscopy

In fluorescence correlation spectroscopy (FCS), a confocal microscope is used to record fluorescence intensity fluctuations at a single spot of a sample with high temporal resolution (figure 2.4) [116–118]. Using the combination of a high numerical aperture lens and confocal optics, the size of the observation volume is reduced to a diffraction limited volume element and is typically on the order of 0.6 femtolitre.

Similar to FRAP, information about molecular processes is derived from measuring the relaxation kinetics of a perturbed system. However, in FCS the perturbation is not induced experimentally but is a result of spontaneous statistical fluctuations. To get reliable data on the relaxation kinetics, a large number of fluctuation events has to be recorded over time. Therefore, a single FCS measurement usually requires integration times of several seconds to minutes. The fluctuations are subsequently analysed by calculating the autocorrelation function of the fluorescence signal. This effectively derives an

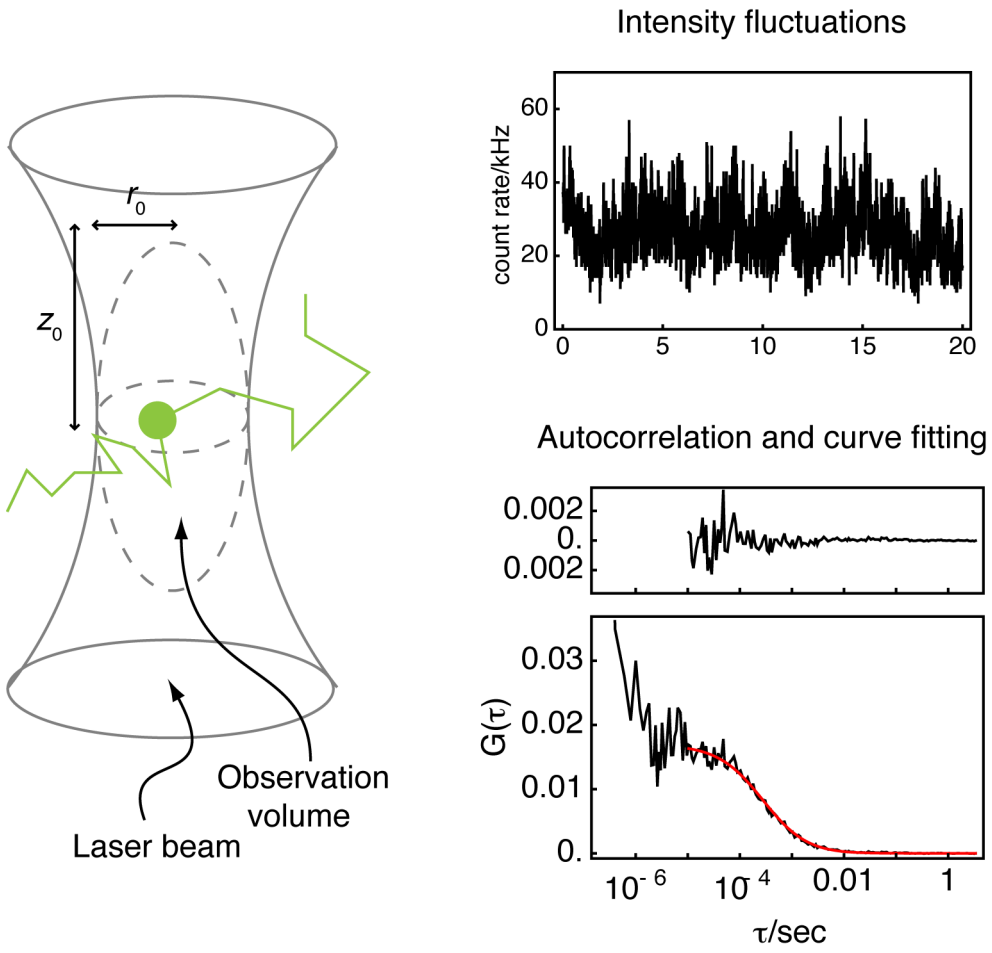

Figure 2.4: Principle of fluorescence correlation spectroscopy (FCS). Left: Fluorescent particles move stochastically through a diffraction limited observation volume. The typical dimensions are $r_0 = 0.2\,\mu$m and $z_0 = 1\,\mu$m. Right: Intensity fluctuations are recorded at a high temporal resolution over a period of several seconds. The fluctuations are autocorrelated and the autocorrelation curve is analyzed by curve fitting. The typical autocorrelation curve shown here (black line in the lower panel) was measured for EGFP in the nucleus of a HeLa cell. The red line shows a fit of eq. 2.3. The upper panel shows the fit residuals.

ensemble average of all individual fluctuation events.

The autocorrelation function $G(\tau)$ of a time-dependent fluorescent signal $F(t)$ quantifies the extent to which the fluorescence signal at time t is related to the signal at a later time $t + \tau$. This information is averaged over all time points t. $G(\tau)$ is commonly defined as

$$G(\tau) = \frac{\langle \delta F(t) \cdot \delta F(t+\tau) \rangle}{\langle F \rangle^2} \tag{2.1}$$

where $\delta F(t) = F(t) - \langle F \rangle$ is the intensity fluctuation at time t and the angle brackets denote the average over all t. Since intensity fluctuations are proportional to fluctuations in the number of fluorescent particles, the amplitude of the autocorrelation function contains information about the average number of particles in the observation volume. The number of particles at any given time point is Poisson distributed, consequently the variance in the observed particle number is $\sigma^2 = \langle \delta N^2 \rangle = N$, where N is the average particle number. Inserting this into the definition of the autocorrelation amplitude yields:

$$G(0) = \frac{\langle \delta F(t)^2 \rangle}{\langle F \rangle^2} = \frac{\langle \delta N(t)^2 \rangle}{N^2} = \frac{1}{N} \tag{2.2}$$

The autocorrelation amplitude can therefore be used to measure the absolute number of particles in the observation volume and, if the size of the observation volume is known, the absolute concentration of a fluorescent molecules in a sample.

Calculation of the autocorrelation function itself is a model-free operation, i.e. it does not rely on a model of molecular processes and consequently does not provide direct information about the processes that give rise to the intensity fluctuations, apart from the average sample concentration. Further information can only be gained by fitting an appropriate model to the autocorrelation curve.

The primary source of particle number fluctuations is the diffusion of fluorophores into and out of the observation volume. To derive a mathematical description for this process, the efficiency of excitation and detection of the fluorophores depending on their relative position in the observation volume needs to be taken into account. For a confocal microscope this is modelled with a three-dimensional gaussian function (for details see chapter 3). For three-dimensional diffusion this yields the following model for the autocorrelation function [119]:

$$G_D(\tau) = \frac{1}{N}\frac{1}{1+\tau/\tau_D}\sqrt{\frac{1}{1+\tau/(S^2\tau_D)}} \tag{2.3}$$

Here, τ_D is the characteristic dwell time of a particle in the observation volume, which is related to the diffusion constant D and the width of the observation volume r_0 via $\tau_D = r_0^2/4D$. S is called the structural parameter and gives the ratio between the height and the width of the observation volume, $S = z_0/r_0$.

If a sample contains a mixture of fluorescent species, each with a different diffusion constant and corresponding dwell time $\tau_{D,i}$, the autocorrelation function is a weighted sum of diffusion terms:

$$G_D(\tau) = \frac{1}{N}\sum_i F_i \frac{1}{1+\tau/\tau_{D,i}}\sqrt{\frac{1}{1+\tau/(S^2\tau_{D,i})}} \tag{2.4}$$

Where F_i is the relative molar fraction of species i and N is the total number of fluorescent particles of all species.

Transitions of fluorophores from a fluorescent to a non-fluorescent state are a second source of fluorescence intensity fluctuations that is commonly observed. Because this transition involves intersystem crossing of an excited fluorophore from a singlet to a triplet state, it is also referred to as triplet blinking. If modelled as an isomerization reaction, this adds an exponential prefactor to the autocorrelation function [119]:

$$G_T(\tau) = \left(1 + \frac{F_T \exp(-\tau/\tau_T)}{1-F_T}\right) G_D(\tau) \tag{2.5}$$

Here, F_T is the fraction of non-fluorescent fluorophores and τ_T is the dark state's relaxation time.

To conclude, FCS can be used to directly quantify the absolute concentration of fluorophores in a sample and their biophysical properties such as the diffusion constant and photophysical transitions. Because measurements are performed at a single point of a sample with a very high sampling rate on the order of $> 1\,\mathrm{MHz}$, it is superior to FRAP in the analysis of rapid molecular dynamics.

An important limitation of FCS regards its requirement for equilibrium conditions. That is, the sample has to remain constant with respect to the average molecule concentration, mobility, and brightness. It is therefore highly important to minimise the extent of photobleaching, as this will reduce the average

fluorophore concentration causing an artificial component in the autocorrelation curve. FCS measurements are also limited to a certain range of fluorophore concentrations. If the concentration is too high, individual fluctuation events only have minor relative contribution to the average fluorescence intensity and are indistinguishable from noise. On the other hand, if the concentration is too low, fluctuation events are rare resulting in increased integration times. While this is formally a limitation as it prevents measurements at sample concentrations above 1 μM, the sensitivity of FCS allows measurements at significantly lower expression levels of fluorescent proteins than FRAP. This reduces the risk of expression level dependent artefacts. Typically, FCS measurements are performed on samples in the nanomolar concentration range.

Fluorescence crosscorrelation spectroscopy

An important extension of FCS is dual-colour fluorescence crosscorrelation spectroscopy (FCCS) [120]. In FCCS two molecular species A and B are labelled with spectrally well separated fluorophores and the fluorescence intensity fluctuations of each are recorded in separate detectors. The crosscorrelation function is defined in analogy to eq. 2.1 as:

$$G_X(\tau) = \frac{\langle \delta F_A(t) \cdot \delta F_B(t+\tau) \rangle}{\langle F_A(t) \rangle \cdot \langle F_B(t) \rangle} \tag{2.6}$$

$G_X(\tau)$ is a statistical measure for the extent to which fluctuations of the two species occur concomitantly. This is the case if the two species interact and move through the observation volume as a single particle. Therefore, the temporal decay of $G_X(\tau)$ is determined by the mobility properties of the complex between A and B, and the amplitude of the crosscorrelation signal is related to its concentration:

$$G_X(0) = \frac{[AB]}{V_{\text{eff}}\,[A]_T\,[B]_T} \tag{2.7}$$

Here, $[AB]$ is the concentration of the complex while $[A]_T$ and $[B]_T$ are the *total* concentrations of the two interacting species, i.e. the sum of the concentration of unbound and bound molecules. V_{eff} is the effective overlap of the two observation volumes. Because the total concentrations of A and B can be calculated from their respective autocorrelation amplitudes, crosscorrelation measurements can be used to calculate the absolute concentration of the complex.

3 Analysis of binding and diffusion by fluorescence correlation spectroscopy

3.1 The binding-diffusion model

In the following paragraphs, I derive a model for the analysis of binding reactions by FCS following and extending an approach originally developed by Elson and Magde [116]. The basic biological assumption of this model is that proteins can either freely diffuse or can be immobilized by binding to specific binding sites (see figure 3.1). Diffusion is assumed to follow Fick's law, while binding is modelled as a single-step bimolecular binding reaction. This reaction-diffusion system can be described by a system of differential equations:

$$\begin{aligned} \frac{\partial[A]}{\partial t} &= D\nabla^2[A] - k_{\text{on}}[B][A] + k_{\text{off}}[AB] \\ \frac{\partial[B]}{\partial t} &= -k_{\text{on}}[B][A] + k_{\text{off}}[AB] \\ \frac{\partial[AB]}{\partial t} &= k_{\text{on}}[B][A] - k_{\text{off}}[AB] \end{aligned} \tag{3.1}$$

where $[A]$ is the concentration of unbound proteins, $[B]$ is the concentration of available binding sites, and $[AB]$ is the concentration of the AB complex. D is the diffusion constant of A, ∇^2 is the Laplacian operator, k_{on} is the association rate constant, and k_{off} is the dissociation rate constant.

To simplify eq. (3.1), the concentration of binding sites, $[B]$, is assumed to be much larger than the concentration of binding partners, $[A] + [AB]$. Under this condition, changes in $[B]$ due to binding can be neglected and $[B]$ can be assumed to be constant. This eliminates the second equation from eq. (3.1) and also introduces a pseudo-first-order association rate constant $k_{\text{on}}[B]$.

3.2 Derivation

The concentration correlation function

The first step in calculating the fluorescence autocorrelation function is to calculate the concentration correlation function. For a system of m labelled

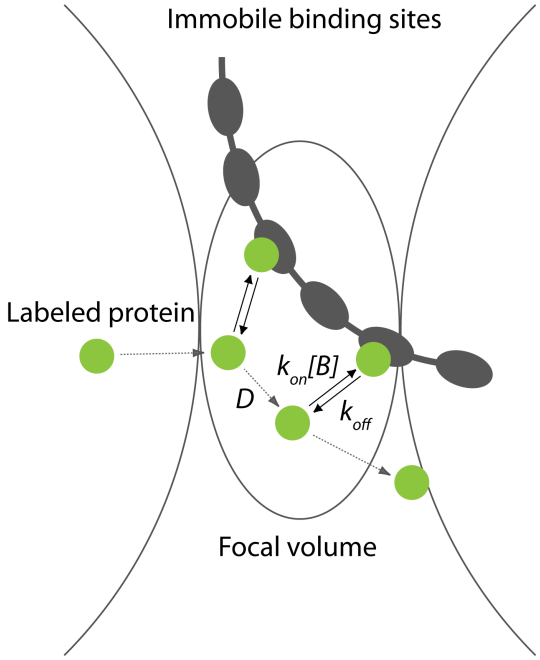

Figure 3.1: Schematic depiction of the binding-diffusion model. The diffusion constant D describes the labelled protein's diffusion, while the association rate constant $k_{\text{on}}[B]$ and the dissociation rate constant k_{off} describe the transient interaction with immobile binding sites. The confocal observation volume, from which the fluorescence fluctuations are observed, is modelled by a three-dimensional Gaussian.

components, the concentration correlation function, $\phi_{jl}(\mathbf{r}, \mathbf{r}', t)$, compares the concentration fluctuations of component j at position $\mathbf{r}$ to the concentration fluctuation of component l at position $\mathbf{r}'$ and after time τ:

$$\phi_{jl}(\mathbf{r}, \mathbf{r}', \tau) = \langle \delta C_j(\mathbf{r}, 0) \delta C_l(\mathbf{r}', \tau) \rangle \tag{3.2}$$

Here, $\delta C_l(\mathbf{r}, \tau) = C_l(\mathbf{r}, \tau) - \langle C_l \rangle$ is the local deviation from the average concentration $\langle C_l \rangle$.

If the δC_l are small with respect to the equilibrium concentrations, chemical rate equations such as those in eq. (3.1) can be used to describe the relaxation of the δC_l. In general terms, the system of differential equations for the δC_l can be written as:

$$\frac{\partial \delta C_l(\mathbf{r}, \tau)}{\partial \tau} = D_l \nabla^2 \delta C_l(\mathbf{r}, \tau) + \sum_{k=1}^{m} T_{lk} \delta C_k(\mathbf{r}, \tau) \tag{3.3}$$

Here, the matrix elements T_{lk} are the chemical rate constants and the equilibrium concentrations of the components, and D_l is the diffusion constant of component l.

To calculate ϕ_{jl}, eq. (3.3) needs to be solved for the $\delta C_l(\mathbf{r}, \tau)$. This is achieved by Fourier-transformation, which transforms eq. (3.3) into:

$$\frac{\partial \tilde{C}_l(\mathbf{q}, \tau)}{\partial \tau} = \sum_{k=1}^{m} M_{lk} \tilde{C}_k(\mathbf{q}, \tau) \tag{3.4}$$

where $\tilde{C}_l(\mathbf{q}, \tau) = (2\pi)^{-3/2} \int d^3\mathbf{r}\, e^{i\mathbf{q}\mathbf{r}} \delta C_l(\mathbf{r}, \tau)$ is the Fourier-transformation of $\delta C_l(\mathbf{r}, \tau)$, and $M_{lk} = T_{lk} - D_l \mathbf{q}^2 \delta_{lk}$. For the particular binding-diffusion system in eqs. (3.1) with the two species A and C, the matrix M is:

$$M = \begin{pmatrix} -k_{\text{on}}[B] - \mathbf{q}^2 D & k_{\text{off}} \\ k_{\text{on}}[B] & -k_{\text{off}} \end{pmatrix} \tag{3.5}$$

The solution of the system in eq. (3.4) is expressed through the eigenvalues $\lambda^{(s)}$ and the matrix of eigenvectors X of the matrix M:

$$\tilde{C}_l(\mathbf{q}, \tau) = \sum_{s=1}^{m} X_l^{(s)} e^{\lambda^{(s)} \tau} \sum_{k=1}^{m} (X^{-1})_k^{(s)} \tilde{C}_k(\mathbf{q}, 0) \tag{3.6}$$

This result is inserted into eq. (3.2), and Fourier-synthesis is performed:

$$\begin{aligned}\phi_{jl}(\mathbf{r},\mathbf{r}',\tau) &= (2\pi)^{-3/2}\int d^3\mathbf{q}\, e^{-i\mathbf{q}\mathbf{r}'}\langle\delta C_j(\mathbf{r},0)\tilde{C}_l(\mathbf{q},\tau)\rangle \\ &= (2\pi)^{-3/2}\int d^3\mathbf{q}\, e^{-i\mathbf{q}\mathbf{r}'}\sum_{s=1}^{m} X_l^{(s)} e^{\lambda^{(s)}\tau}\sum_{k=1}^{m}(X^{-1})_k^{(s)}\langle\delta C_j(\mathbf{r},0)\tilde{C}_k(\mathbf{q},0)\rangle \\ = (2\pi)^{-3}\int d^3\mathbf{q}\, e^{-i\mathbf{q}\mathbf{r}'}\sum_{s=1}^{m} X_l^{(s)} e^{\lambda^{(s)}\tau}\sum_{k=1}^{m}(X^{-1})_k^{(s)}\int d^3\mathbf{r}''\, e^{i\mathbf{q}\mathbf{r}''}\langle\delta C_j(\mathbf{r},0)\delta C_k(\mathbf{r}'',0)\rangle\end{aligned} \tag{3.7}$$

The zero-time correlations $\phi_{jk}(\mathbf{r},\mathbf{r}'',0) = \langle\delta C_j(\mathbf{r},0)\delta C_k(\mathbf{r}'',0)\rangle$, can be simplified assuming an ideal chemical solution. Under this condition, the positions of different molecules of the same species as well as those of different species must be uncorrelated, and:

$$\langle\delta C_j(\mathbf{r},0)\delta C_k(\mathbf{r}'',0)\rangle = \langle C_j\rangle\delta_{jk}\delta(\mathbf{r}-\mathbf{r}'') \tag{3.8}$$

Hence, the mean square fluctuation of C_j in a given volume is equal to the mean concentration $\langle C_j\rangle$, as dictated by Poisson statistics.

By inserting eq. 3.8 into eq. 3.7, and performing the integration over $\mathbf{r}''$, we arrive at the following equation for the concentration correlation function[1]:

$$\phi_{jl}(\mathbf{r},\mathbf{r}',\tau) = \frac{\langle C_j\rangle}{(2\pi)^3}\int d^3\mathbf{q}\, e^{i\mathbf{q}(\mathbf{r}-\mathbf{r}')}\sum_{s=1}^{m} X_l^{(s)} e^{\lambda^{(s)}\tau}(X^{-1})_j^{(s)} \tag{3.9}$$

As has been shown elsewhere, this function is symmetric with respect to the indices j and l: $\phi_{jl}(\mathbf{r},\mathbf{r}',\tau) = \phi_{lj}(\mathbf{r},\mathbf{r}',\tau)$ [116].

The normalized intensity correlation function

The normalized intensity correlation function $G(\tau)$ is defined by the fluorescence intensity fluctuations $\delta i(t)$ measured at time t and after time $t+\tau$, averaged over all t, and normalized to the squared mean intensity:

$$G(\tau) = \frac{\langle\delta i(0)\delta i(\tau)\rangle}{\langle i(t)\rangle^2} \tag{3.10}$$

The intensity fluctuations $\delta i(\tau)$ of component j are proportional to the concentration fluctuations $\delta C_j(\mathbf{r},\tau)$, as well as to the excitation intensity $I(\mathbf{r})$,

[1] With $\int d^3\mathbf{r}''\, e^{i\mathbf{q}\mathbf{r}''}\langle C_j\rangle\delta_{jk}\delta(\mathbf{r}-\mathbf{r}'') = \langle C_j\rangle\delta_{jk}e^{i\mathbf{q}\mathbf{r}}$.

and the product of the jth component's extinction coefficient and fluorescence quantum yield, Q_j:

$$\delta i(\tau) = \int d^3\mathbf{r} I(\mathbf{r}) \sum_{j=1}^{m} Q_j \delta C_j(\mathbf{r}, \tau) s \tag{3.11}$$

In fact, $I(\mathbf{r})$ describes both the illumination as well as detection properties of the optical setup. For a confocal microscope, $I(\mathbf{r})$ is approximated by a three dimensional Gaussian with the transversal width r_0 and the axial width z_0:

$$I(\mathbf{r}) = \exp\left(-2\left(x^2+y^2\right)/r_0^2\right) \cdot \exp\left(-2z^2/z_0^2\right) \tag{3.12}$$

Inserting eq. (3.11) into eq. (3.10) yields:

$$G(\tau) = \frac{1}{\langle i(t)\rangle^2} \iint d^3\mathbf{r}\, d^3\mathbf{r}'\, I(\mathbf{r}) I(\mathbf{r}') \sum_{jl} Q_j Q_l \phi_{jl}(\mathbf{r}, \mathbf{r}', \tau) \tag{3.13}$$

Because of the symmetry of ϕ, the number of summation terms that actually have to be calculated can be reduced by writing:

$$G(\tau) = \frac{1}{\langle i(t)\rangle^2} \iint d^3\mathbf{r}\, d^3\mathbf{r}'\, I(\mathbf{r}) I(\mathbf{r}') \sum_{j} \sum_{l\le j} (2-\delta_{jl}) Q_j Q_l \phi_{jl}(\mathbf{r}, \mathbf{r}', \tau) \tag{3.14}$$

With eq. (3.9), this leads to:

$$\begin{aligned} G(\tau) = \frac{1}{\langle i(t)\rangle^2} \int d^3\mathbf{q} \sum_{j} \sum_{l\le j} (2-\delta_{jl}) \\ Q_j Q_l \frac{\langle C_j\rangle}{(2\pi)^3} \sum_{s=1}^{m} X_l^{(s)} e^{\lambda^{(s)}\tau} (X^{-1})_j^{(s)} \iint d^3\mathbf{r}\, d^3\mathbf{r}'\, e^{i\mathbf{q}(\mathbf{r}-\mathbf{r}')} I(\mathbf{r}) I(\mathbf{r}') l \end{aligned} \tag{3.15}$$

With the integral:

$$\iint d^3\mathbf{r}\, d^3\mathbf{r}'\, e^{i\mathbf{q}(\mathbf{r}-\mathbf{r}')} I(\mathbf{r}) I(\mathbf{r}') = (\pi/2)^3\, r_0^2\, z_0\, e^{\left(-r_0^2(q_x^2+q_y^2)/4 - z_0^2 q_z^2/4\right)} \tag{3.16}$$

and the mean intensity

$$\langle i(t)\rangle = \int d^3\mathbf{r} I(\mathbf{r}) \sum_{j=1}^{m} Q_j \langle C_j\rangle = (\pi/2)^{3/2}\, r_0 \sqrt{z_0} \sum_{j=1}^{m} Q_j \langle C_j\rangle \tag{3.17}$$

the general form of the normalized intensity correlation is:

$$G(\tau) = \frac{1}{\left(\sum Q_j \langle C_j \rangle\right)^2} \int d^3\mathbf{q}\, e^{\left(-r_0^2(q_x^2+q_y^2)/4 - z_0^2 q_z^2/4\right)} \sum_j \sum_{l \le j} (2-\delta_{jl}) Q_j Q_l \frac{\langle C_j \rangle}{(2\pi)^3} \sum_{s=1}^{m} X_l^{(s)} e^{\lambda^{(s)}\tau} (X^{-1})_j^{(s)} \quad (3.18)$$

The correlation function in cylindrical coordinates

To simplify the calculation of $G(\tau)$, the integration over $\mathbf{q}$ is performed in cylindrical coordinates, using the substitutions $q_x = q_r \cos q_\phi$, $q_y = q_r \sin q_\phi$, $q_x^2 + q_y^2 = q_r^2$, $dq_x dq_y = r dq_r dq_\phi$. Instead of integrating over q_x and q_y from -∞ to ∞, the integration is performed over q_ϕ and q_r from 0 to 2π and 0 to ∞, respectively. The integral is simplified further by taking into account the fact that the integral is symmetric with respect to q_z. Hence:

$$G(\tau) = \frac{1}{\left(2\pi \sum Q_j \langle C_j \rangle\right)^2} \int_0^\infty dq_r \int_0^\infty dq_z\, r e^{\left(-r_0^2 q_r^2/4 - z_0^2 q_z^2/4\right)} \sum_j \sum_{l \le j} (2-\delta_{jl}) Q_j Q_l \langle C_j \rangle \sum_{s=1}^{m} X_l^{(s)} e^{\lambda^{(s)}\tau} (X^{-1})_j^{(s)} \quad (3.19)$$

Note that $\mathbf{q}^2 = q_r^2 + q_z^2$ is also replaced in the matrix M.

3.3 Parameter dependence

For the matrix M defining the binding diffusion model (eq. (3.5)), the integral in eq. (3.19) cannot be solved analytically but has to be approximated numerically. Figure 3.2 shows numerical solutions to eq. (3.19) calculated for different parameter values. In these examples the geometrical parameters are set to $r_0 = 0.2\,\mu$m and $z_0 = 4.75\, r_0$, reflecting the optical properties of the experimental setup used in this work. The total concentration of fluorescent proteins is set to $C_{\text{total}} = [A] + [AB] = 78$ nM, corresponding to an average of 10 particles in the observation volume. This concentration of fluorescent proteins is typically in encountered in live cell FCS experiments such as those described in section 4. The solutions are shown as a function of the diffusion constant, the dissociation rate constant, and the fraction of unbound proteins,

F. Here, F is defined as the average concentration of unbound protein, $[A]$, relative to the total concentration, $C_{\text{total}} = [A] + [AB]$. Based on the law of mass action, F can be expressed as a function of the association and dissociation rate constants:

$$F = \frac{[A]}{C_{\text{total}}} = \frac{k_{\text{off}}}{k_{\text{on}}[B] + k_{\text{off}}} \tag{3.20}$$

Typical diffusion constants of proteins that are freely diffusing in living cells and are not part of large multi-protein complexes range from $5\,\mu\text{m}^2\,\text{s}^{-1}$ to $50\,\mu\text{m}^2\,\text{s}^{-1}$, while dissociation rate constants of proteins transiently interacting with a macromolecular structure such as chromatin can range from $1\,\text{s}^{-1}$ to $100\,\text{s}^{-1}$ (see for example [115]). In this parameter regime, diffusion and binding kinetics produce two clearly distinguishable components in the autocorrelation curves (figure 3.2). The first component is dependent on the diffusion constant only and shifts to shorter correlation times when D is increased. The dissociation rate constant only affects the second component that shifts to shorter times when k_{off} is increased. The fraction of unbound proteins determines the relative contribution of the two components to the correlation curve.

To conclude, the binding-diffusion model derived in this section allows the quantitative analysis of binding reactions between mobile proteins and immobile binding sites by FCS. By fitting this model to experimental data, it should be possible to determine the diffusion constant, the dissociation rate constant, as well as the steady-state fraction of unbound proteins. It is important to point out, that this information can only be reliably gained from curve fitting if the two autocorrelation components are sufficiently well separated and the dissociation rate is within a certain range. If the interaction is highly transient, i.e. k_{off} is very large, the intensity fluctuations are dominated by diffusion and only a single autocorrelation component is visible. In this case, fitting of the binding-diffusion model to the data will not lead to correct estimates for the binding and diffusion parameters because changes in D and k_{off} will compensate each other. If, on the other hand, the interaction is very stable, i.e. k_{off} is very small, bound proteins will eventually reside in the focal volume so long, that they will be bleached. Strong photobleaching results in an artifactual autocorrelation component at long correlation times, which would prevent the correct analysis of the diffusion and binding components.

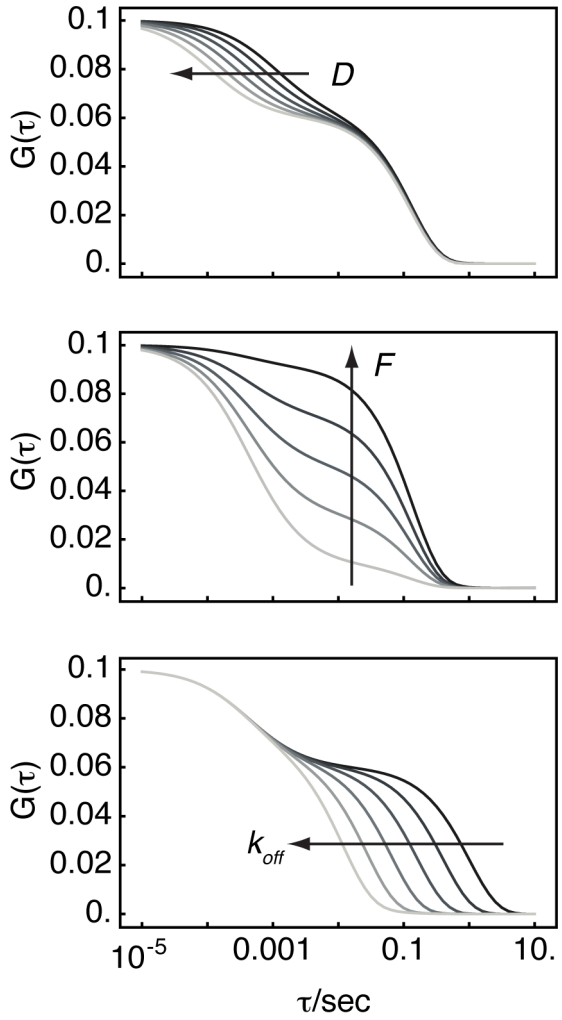

Figure 3.2: Numerical solutions to eq. (3.19). The diffusion constant is varied from 5 to 100 μm^2 s^{-1} (top panel), the fraction of unbound proteins is varied from 0.1 to 0.9 (middle), and the dissociation rate constant is varied from 1 to 100 s^{-1} (bottom). In each case the arrow points in the direction of increasing parameter values.

4 Experiments

4.1 Steady-state binding of RCC1 to chromatin during mitosis

To study cell-cycle dependent chromatin affinity of RCC1, a method is needed to quantitatively measure chromatin affinity, ideally in living cells. A useful measure for chromatin binding affinity is the fraction F of unbound RCC1, defined as the concentration of unbound RCC1 relative to its total concentration:

$$F = \frac{[\mathrm{RCC1}]_{\mathrm{unbound}}}{[\mathrm{RCC1}]_{\mathrm{unbound}} + [\mathrm{RCC1}]_{\mathrm{bound}}} \tag{4.1}$$

During mitosis, chromatin and cytoplasm are not separated by the nuclear envelope and unbound RCC1 should be able to freely equilibrate between chromatin and cytoplasm (an assumption that is corroborated by experiments described below). This allows the measurement of the unbound fraction by quantitative imaging of fluorescently tagged RCC1. In a confocal image of a mitotic cell, the average cytoplasmic fluorescence intensity should be proportional to the concentration of unbound RCC1, while the average fluorescence intensity on chromatin should be proportional to the total concentration of bound and unbound RCC1. Hence, the unbound fraction can be determined from the average fluorescence intensities:

$$F = \frac{I_{\mathrm{cytoplasm}}}{I_{\mathrm{chromatin}}} \tag{4.2}$$

HeLa cells transiently expressing a fusion protein of RCC1 γ and enhanced green fluorescent protein (RCC1-EGFP) were imaged by confocal microscopy during metaphase of mitosis (for details see chapter 6). As expected, RCC1-EGFP strongly localized to the condensed chromatin (figure 4.1) where it colocalized with transiently expressed diHcRed-tagged histone H2B (data not shown). By measuring the average image intensity in the cytoplasm relative to the average image intensity of the chromatin region, an unbound fraction of 0.05 ± 0.01 ($n = 5$ cells, figure 4.1 A and B) was determined for RCC1-EGFP.

To confirm that accumulation on chromatin is a readout of chromatin binding affinity, the mutant RCC1-Δ27 was studied by quantitative imaging.

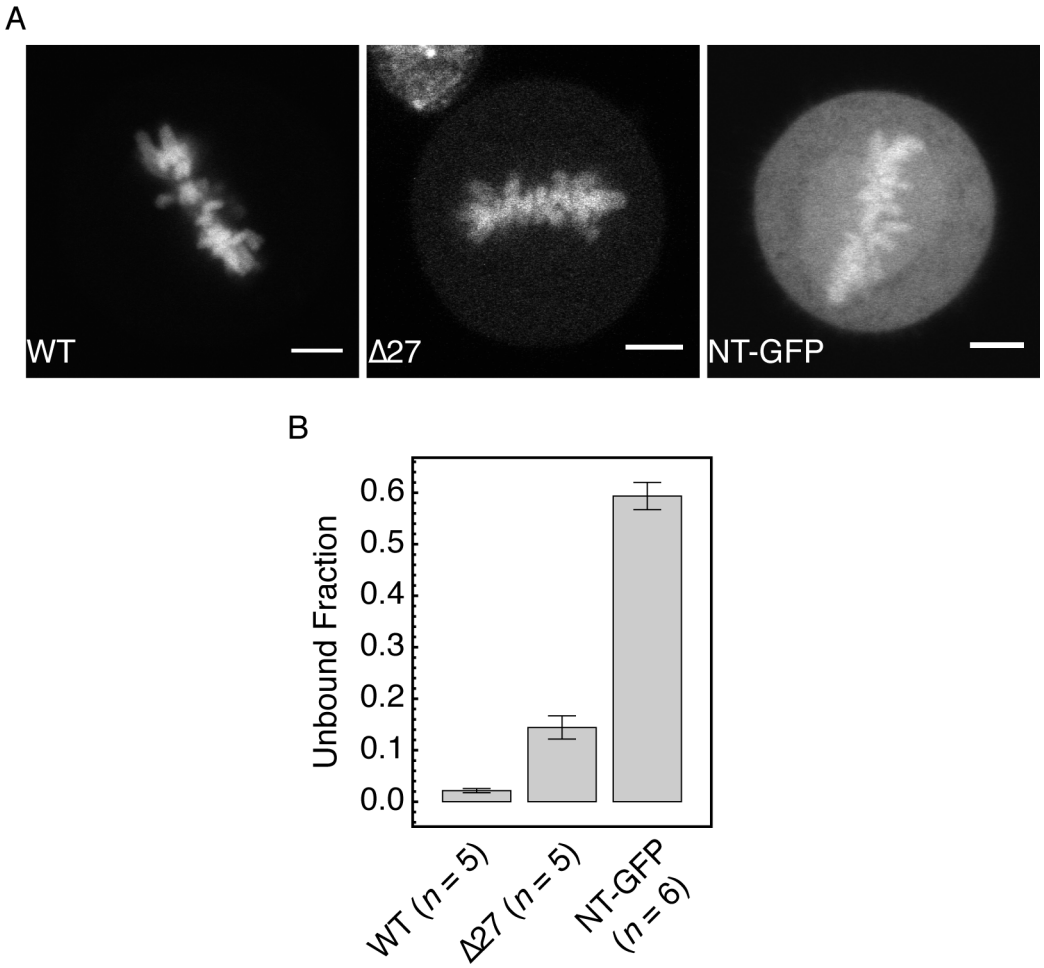

Figure 4.1: Quantitative imaging of the unbound fraction in mitotic cells. A: Mitotic cells expressing different constructs of RCC1-EGFP were imaged using confocal microscopy. B: The fraction of unbound protein was calculated from the average image intensity in the cytoplasm and on the chromatin. Error bars indicate standard deviation from measurements in n cells. Scale bars: 5 μm.

RCC1-Δ27 lacks the first 27 amino-terminal amino acids, which mediate binding to DNA and contribute to chromatin binding together with two loops of the β-propellor fold [100, 102]. Hence, RCC1-Δ27 is expected to have a reduced but not completely abolished chromatin binding affinity. Consistent with the reduced chromatin affinity, the unbound fraction was 0.14 ± 0.02 ($n = 5$) for RCC1-Δ27 (figure 4.1 A and B).

A fusion protein of the N-terminal peptide of RCC1 (amino acid positions 1 to 27) and EGPF (NT-GFP), accumulated on chromatin of mitotic cells to a markedly lesser degree than full length or Δ27 RCC1 (figure 4.1 A). The unbound fraction determined by quantitative imaging was 0.59 ± 0.03 ($n = 6$) (figure 4.1 B). Despite the reduced accumulation on chromatin, this shows that the N-terminus of RCC1 retains its chromatin binding ability.

4.1.1 Equilibration between chromatin and cytoplasm during mitosis

The determination of the unbound fraction of RCC1 by quantitative imaging relies on the assumption that unbound RCC1 can freely equilibrate between chromatin and cytoplasm in mitotic cells and that this equilibrium is already established at the time of metaphase. To test this assumption, mitotic HeLa cells coexpressing RCC1-EGFP and mCherry-Tubulin were treated with nocodazole to arrest them in metaphase. Imaging of mCherry-Tubulin demonstrated that nocodazole treatment effectively disrupted the mitotic spindle, in particular spindle pole integrity, and should therefore induce mitotic arrest. Consistent with previous reports, nocodazole treatment did not completely depolymerize the spindle, as kinetochore fibres are resistant to nocodazole-induced depolymerization [121] (fig. 4.2 A). Due to the mitotic arrest, the unbound fraction could be measured by quantitative imaging over a period of over 70 minutes, considerably longer than the time unperturbed HeLa cells spend in metaphase (less than 40 minutes, data not shown). The unbound fraction stayed constant over this period indicating that RCC1 on the chromatin is in equilibrium with the cytoplasmic pool (figure 4.2 A and B).

To directly determine the time it takes for RCC1 on the chromatin to equilibrate with the cytoplasm, a photoactivation experiment was performed, in which RCC1 fused to photoactivatable GFP (paGFP) was selectively photoactivated on chromatin in mitotic cells. Subsequently the average cytoplasmic intensity of RCC1-paGFP was measured. Cytoplasmic fluorescence increased and reached a steady-state within seconds after the photoactivation pulse (figure 4.2 C). This demonstrated that equilibration of unbound RCC1 only takes seconds. Therefore equilibration between chromatin and cytoplasm is expected

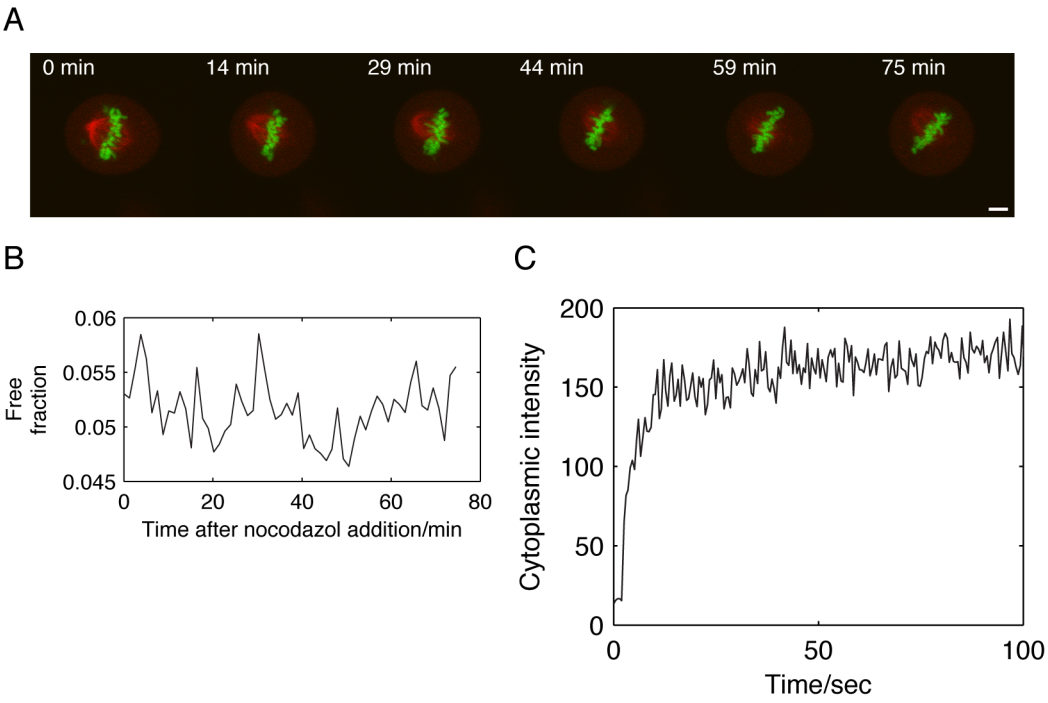

Figure 4.2: Equilibration of RCC1 between chromatin and cytoplasm in mitotic cells. A and B: A HeLa cell expressing RCC1-EGFP (green) and Tubulin-mCherry (red) was arrested in metaphase with 100 ng/ml nocodazole and imaged over a period of over one hour. Scale bar: 5 μm. Cytoplasmic and chromatin intensities of RCC1-EGFP were measured and used to calculate the fraction of unbound RCC1 (B). The ratio of cytoplasmic to chromatin-bound protein stayed constant over the observation period. C: RCC1-paGFP was photoactivated on mitotic chromatin. The cytoplasmic intensity of photoactivated RCC1-paGFP increased and reached a steady-state within seconds after the activation pulse.

to occur directly after nuclear envelope breakdown and certainly has reached steady state by the time of metaphase.

4.2 Dynamic binding of RCC1 to chromatin

Quantitative imaging provides a way to measure the steady-state distribution between unbound and bound RCC1 and is related to the dissociation constant of the RCC1-chromatin interaction. However it is not possible to image this distribution in interphase cells because chromatin and nucleoplasm cannot be distinguished by the resolution of conventional light microscopy and because the cytoplasmic concentration does not equal the concentration of unbound RCC1 in the nucleus due to the effect of active nuclear import. Furthermore, imaging of the average fluorescence intensity provides no information on the dynamics of the chromatin interaction.

As outlined in section 3, the measurement of protein mobility with FCS is a potential method to measure the distribution of bound and unbound proteins in a diffraction limited observation volume and to determine the kinetics of binding and unbinding. The following sections therefore describe FCS measurements of RCC1 mobility, aiming at the measurement of the binding dynamics of the RCC1-chromatin interaction.

Mobility measurements were performed on interphase and mitotic cells. Here, mitotic cells refers to cells in metaphase of mitosis, which can be readily identified by their spherical morphology and the characteristic morphology of the chromatin that is condensed and aligned on the metaphase plate (see micrographs in figure 4.1 A). The chromatin itself was either identified by the fluorescence of RCC1 constructs which accumulated on chromatin, or by the region of less fluorescence intensity evident in images of cells expressing EGFP alone. During metaphase, the condensed chromatin is immobile over a timescale of minutes, providing stable conditions for FCS measurements.

4.2.1 Diffusion of GFP

To determine the influence of chromatin on the diffusional mobility of proteins, the diffusion of monomeric EGFP was measured by FCS in different compartments of the cell. Autocorrelation curves of EGFP measured in the cytoplasm or on chromatin of interphase and mitotic HeLa cells could all be fit with a model for free diffusion (equation 2.3 on page 23, for representative measurements see figure 4.3). The EGFP diffusion constants measured in these experiments were $37.79 \pm 4.37\,\mu\mathrm{m}^2\,\mathrm{s}^{-1}$ (mean $\pm$ standard deviation, $n = 15$ cells) in nuclei, $35.12 \pm 6.31\,\mu\mathrm{m}^2\,\mathrm{s}^{-1}$ ($n = 15$) in the cytoplasm of interphase cells,

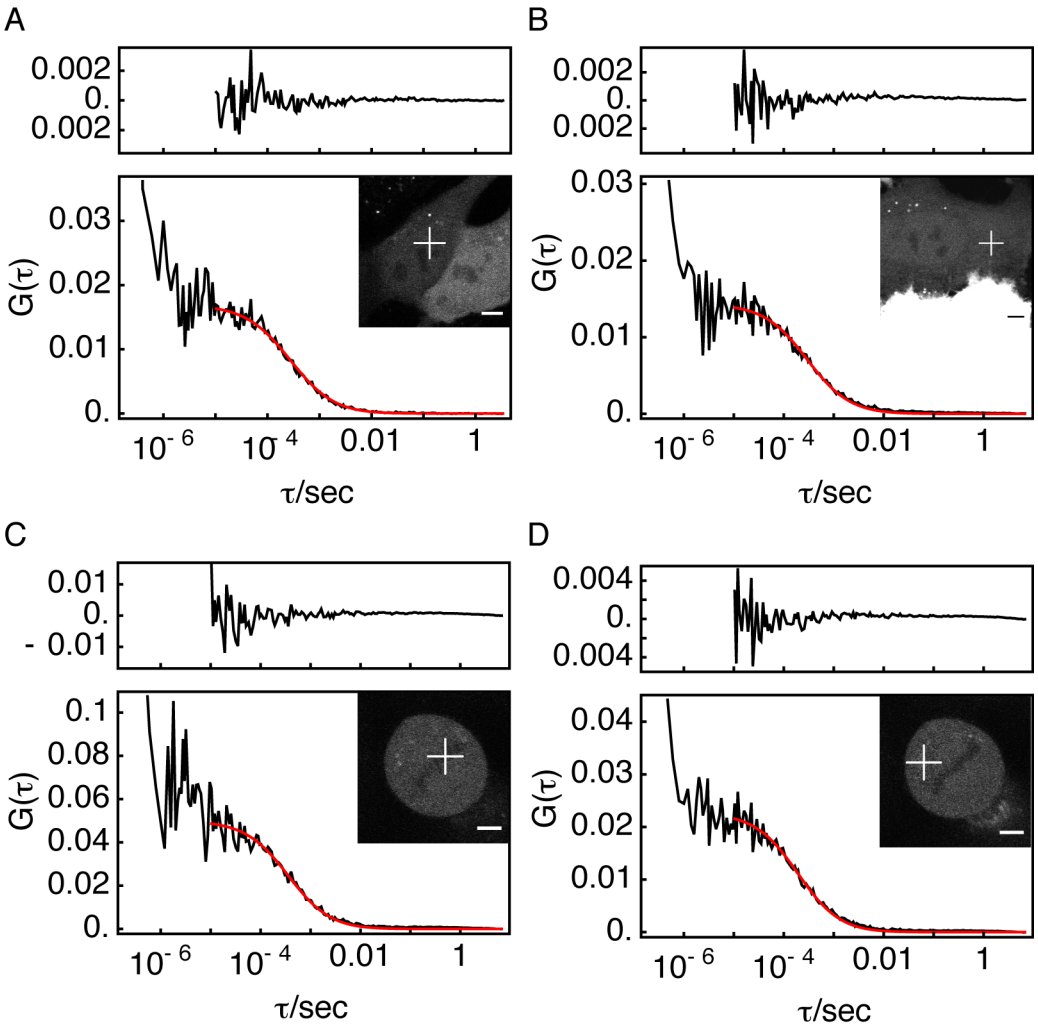

Figure 4.3: Representative autocorrelation curves of EGFP measured in the nucleus of an interphase HeLa cell (A), the cytoplasm of an interphase HeLa cell (B), on the chromatin of a HeLa cell in metaphase (C), and in the cytoplasm of a HeLa cell in metaphase (D). The measurements were fit with a model of free diffusion (red line). The upper panel shows the fit residuals. The insets show confocal images of the measured cells, where the measurement positions are indicated by white crosses. Scale bars: 5 μm

Table 4.1: Diffusion constants of EGFP measured in different compartments of HeLa cells. Values given are mean ± standard deviation calculated from measurements in n different cells. The p-value gives the result of a mean difference test comparing the given sample to EGFP in interphase nuclei.

	$D/\mu\mathrm{m}^2\,\mathrm{s}^{-1}$	n	p-value
Nucleus	37.79 ± 4.37	15	1
Interphase cytoplasm	35.12 ± 6.31	15	0.19
Mitotic chromatin	26.64 ± 4.36	14	$< 10^{-6}$
Mitotic cytoplasm	35.95 ± 6.94	14	0.4

$26.64 \pm 4.36\,\mu\mathrm{m}^2\,\mathrm{s}^{-1}$ ($n = 14$) on mitotic chromatin, and $35.95 \pm 6.94\,\mu\mathrm{m}^2\,\mathrm{s}^{-1}$ ($n = 14$) in the mitotic cytoplasm (table 4.1).

The data were submitted to a two-sided mean difference test, comparing each dataset to EGFP diffusion in interphase nuclei. According to these tests the diffusion of EGFP is not significantly slowed down in the nucleoplasm as compared to the interphase and mitotic cytoplasm (p-values > 0.01). Chemical interactions between EGFP and chromatin therefore do not affect diffusion of EGFP. However, diffusion on mitotic chromatin is significantly reduced compared to interphase chromatin (p-value $< 10^{-6}$). This reduction in the diffusion constant is most likely due to the higher degree of chromatin condensation in mitotic cells. Condensed chromatin probably acts as a barrier to restrict diffusion. As a barrier, chromatin also causes volume exclusion as is evident from the reduced EGFP intensity in confocal images of mitotic cells (figure 4.3 C and D).

4.2.2 Mobility of RCC1

Autocorrelation curves of transiently expressed RCC1-EGFP were measured in living HeLa cells. Figure 4.4 shows representative autocorrelation curves of RCC1-EGFP measured in different compartments of mitotic and interphase HeLa cells. These measurements revealed that the mobility of RCC1 on chromatin is significantly different from its mobility in the cytoplasm. The autocorrelation curves in the nucleus as well as on mitotic chromatin are characterized by two components with approximate correlation times on the order of 1 ms and 100 ms, whereas, in the cytoplasm, the autocorrelation curves have a single component with a correlation time on the order of 1 ms.

FCS measurements of RCC1-EGFP were sensitive to the laser power used for excitation. When autocorrelation curves were measured at the same posi-

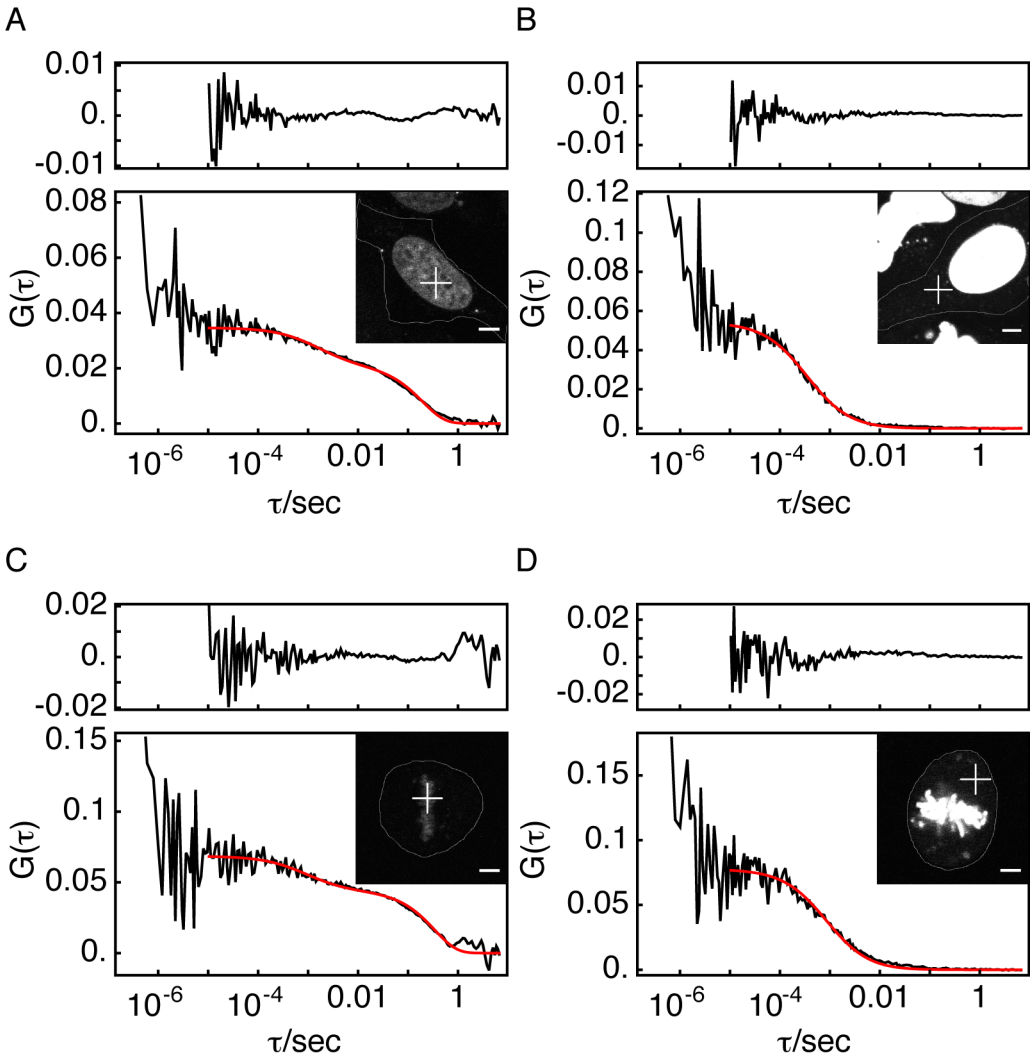

Figure 4.4: Representative autocorrelation curves of RCC1-EGFP measured in the nucleus of an interphase HeLa cell (A), the cytoplasm of an interphase HeLa cell (B), on the chromatin of a HeLa cell in metaphase (C), and in the cytoplasm of a HeLa cell in metaphase (D). The curves in A and C were fit with the binding-diffusion model, the curves in B and D were fit with a model for free diffusion. The upper panel of each graph shows the fit residuals. Insets show confocal images of the measured cells, where the white crosses indicate the measurement positions. Scale bars: 5 μm

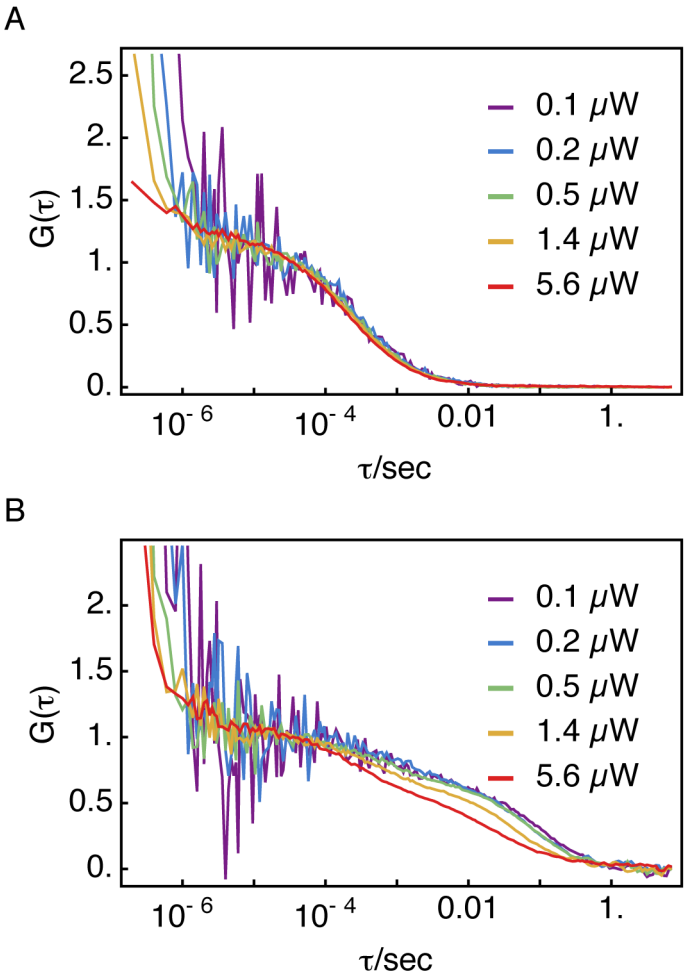

Figure 4.5: Autocorrelation curves of EGFP (A) and RCC1-EGFP (B) measured in the nucleus of HeLa cells at different laser powers. To better compare the shapes, the curves are normalized to have the same amplitude.

tion in interphase nuclei, but at different laser powers ranging from 100 nW to 5.6 μW (absolute laser power measured at the objective), both autocorrelation components shifted to shorter correlation times with increasing laser power (figure 4.5 B). This effect was not observed for FCS measurements of EGFP (figure 4.5 A). Because the autocorrelation curves of RCC1-EGFP converged at low laser powers ($\leq$ 400 nW), a laser power of 220 nW was used for all measurements.

Cytoplasmic mobility

The cytoplasmic mobility of RCC1-EGFP in interphase and mitosis could be described by a model for free diffusion (figure 4.4 B and D). The diffusion of RCC1-EGFP was significantly slower in the mitotic cytoplasm than in the interphase cytoplasm ($D = 11.05 \pm 1.66\,\mu\mathrm{m}^2\,\mathrm{s}^{-1}$, $n = 15$, compared to $D = 27.11 \pm 5.35\,\mu\mathrm{m}^2\,\mathrm{s}^{-1}$, $n = 13$, p-value $< 10^{-8}$, see table 4.2), an effect that was not observed for EGFP alone.

Assuming that the Stokes-Einstein relation holds, i.e. that RCC1-EGFP can be treated as a spherical molecule with a diffusion constant inversely proportional to its radius, the diffusion constant should be inversely proportional to the third root of the molecular mass:

$$D \propto \frac{1}{\sqrt[3]{M}} \tag{4.3}$$

EFGP has a molecular mass of 27 kDa and a diffusion constant of approximately 36 $\mu\mathrm{m}^2\,\mathrm{s}^{-1}$ in the interphase and mitotic cytoplasm. Taking EGFP as a reference, the measured diffusion constants of RCC1-EGFP can therefore be used to estimate the size of the diffusing particle. RCC1-EGFP diffuses as fast as a 63 kDa protein in the interphase cytoplasm and as fast as a 932 kDa protein in the mitotic cytoplasm. In the interphase cytoplasm this estimated mass agrees well with the actual mass of RCC1-EGFP (72 kDa), indicating that RCC1-EGFP diffuses as a monomer in interphase. In contrast, RCC1-EGFP diffuses much slower than expected for a protein of its size in the mitotic cytoplasm, suggesting that is bound to a large multiprotein complex.

This complex might be a RCC1-importin α/β complex. Two observations support this idea. First, RCC1-Δ27, which should not be able to bind to importin α due to its lack of an NLS, diffuses faster than full length RCC1 with a diffusion constant of $16.47 \pm 3.32\,\mu\mathrm{m}^2\,\mathrm{s}^{-1}$ ($n = 14$, p-value $< 10^{-4}$ when compared to full length RCC1). Second, the mutant RCC1-S2,11A diffuses slower than wildtype RCC1 with a diffusion constant of $7.88 \pm 1.41\,\mu\mathrm{m}^2\,\mathrm{s}^{-1}$ ($n = 15$, p-value $< 10^{-5}$). In this mutant, the serine residues 2 and 11 are

Table 4.2: Diffusion constants of RCC1-EGFP, wildtype protein and mutants, measured in the cytoplasm of HeLa cells in interphase and mitosis. Mean ± standard deviation from n cells. The p-value gives the result of a mean difference test comparing the given sample to wildtype RCC1 in the mitotic cytoplasm.

	$D/\mu\mathrm{m}^2\,\mathrm{s}^{-1}$	n	p-value
Interphase			
WT	27.11 ± 5.35	15	$< 10^{-8}$
Mitosis			
WT	11.05 ± 1.66	15	1
Δ27	16.47 ± 3.32	14	$< 10^{-4}$
S2,11A	7.88 ± 1.41	15	$< 10^{-5}$

mutated to alanine, rendering the protein unphosphorylatable during mitosis [99]. N-terminal phosphorylation is thought to inhibit binding of RCC1 to importin α during mitosis, hence a larger fraction of RCC1-S2,11A should be in complex with karyopherins in the mitotic cytoplasm and the apparent diffusion constant should be decreased [98, 99].

Binding of NLS-containing proteins to karyopherins is spatially regulated by the Ran gradient in mitotic cells. Therefore, the fraction of RCC1 bound to importins α and β should be small in the vicinity of chromatin and increase with the distance to chromatin. Consequently, RCC1's diffusion apparent diffusion constant should be a function of the distance to chromatin. To test this hypothesis, autocorrelation curves of EGFP-RCC1 were recorded at multiple positions in single mitotic cells (figure 4.6 A). Autocorrelation curves were fit with a model for free diffusion to determine the apparent diffusion constant. To test if the diffusion constant decreased systematically with the distance to chromatin, the first and the last data points of each series were subjected to a paired two-sided mean difference test. The test failed to detect a significant difference between the diffusion constants measured close to chromatin and close to the cell border ($p-\mathrm{value} = 0.16$, figure 4.6 B). However, a steady decrease in the diffusion constant was apparent in one out of five cells (green points in figure 4.6 B). To conclude, a potential mobility gradient could not be clearly detected with FCS, which might be due to the limited accuracy in the determination of the apparent diffusion constant.

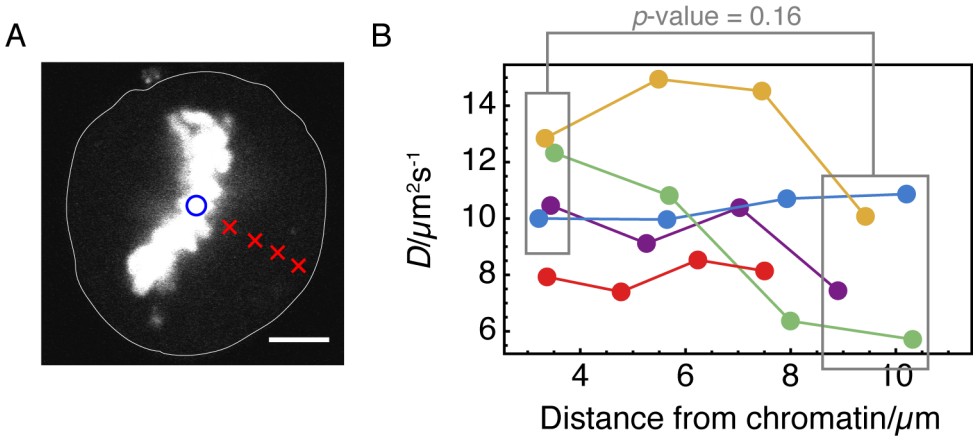

Figure 4.6: A: Confocal image of a representative HeLa cell expressing RCC1-EGFP. Autocorrelation curves were measured at the positions indicated by red crosses. For each position the distance to the centre of mass of chromatin (blue circle) was determined. Scale bar: 5 μm. The cell border is outlined by a thin white line. B: The diffusion constant of RCC1-EGFP in the mitotic cytoplasm as a function of distance from chromatin. Each line represents measurements at four positions in a single cell. Diffusion constants were determined by fitting a model for free diffusion to autocorrelation curves. Data that were subjected to a paired mean difference test are indicated by grey boxes.

Analysis of RCC1 mobility with the binding-diffusion model

The two-component autocorrelation measured for RCC1-EGFP on chromatin suggested that binding interactions such as those between RCC1 and chromatin contribute to the shape of the autocorrelation curves and that the binding-diffusion model discussed in section 3 could be used to analyze those measurements. Indeed, the two-component autocorrelation curves recorded in nuclei or on mitotic chromatin could be fit with the binding diffusion model (figure 4.4 A). For RCC1-EGFP in nuclei, this gave $D = 6.16 \pm 1.52\,\mu\mathrm{m}^2\,\mathrm{s}^{-1}$, $k_{\mathrm{off}} = 4.58 \pm 0.94\,\mathrm{s}^{-1}$, and $F = 0.41 \pm 0.02$ ($n = 21$, see table 4.3). Fitting autocorrelation curves of RCC1-Δ27-EGFP with the binding-diffusion model yielded $D = 8.57 \pm 2.17\,\mu\mathrm{m}^2\,\mathrm{s}^{-1}$, $k_{\mathrm{off}} = 14.8 \pm 4.47\,\mathrm{s}^{-1}$, and $F = 0.5 \pm 0.04$ ($n = 15$, table 4.3). The differences in D, k_{off}, and F between wildtype and RCC-Δ27 were significant as judged by a two-sided mean difference test (p-values $< 10^{-3}$, $< 10^{-6}$, and $< 10^{-6}$, respectively, table 4.3). The changes in k_{off} and F agreed well with the reduced chromatin affinity expected for RCC1-

Table 4.3: Mobility parameters of RCC1-EGFP, wildtype protein and mutants, measured by fitting autocorrelation data with the binding diffusion model. Values given are mean ± standard deviation from n cells. The p-value gives the result of a mean difference test comparing the given sample to wildtype RCC1 in interphase nuclei.

		Nucleus			Mitotic chromatin		
		mean ± SD	n	p	mean ± SD	n	p
$D/\mu\mathrm{m}^2\,\mathrm{s}^{-1}$	WT	6.16 ± 1.52	21	1	6.28 ± 2.3	15	0.85
	Δ27	8.57 ± 2.17	15	$< 10^{-3}$	7.36 ± 2.08	14	0.06
	S2,11A	8.1 ± 2.58	15	0.02	7.59 ± 1.8	15	0.01
$k_{\mathrm{off}}/\mathrm{s}^{-1}$	WT	4.58 ± 0.94	21	1	2.43 ± 1.44	15	$< 10^{-5}$
	Δ27	14.8 ± 4.47	15	$< 10^{-6}$	5.39 ± 2.23	14	0.22
	S2,11A	3.82 ± 1.15	15	0.04	2.0 ± 0.66	15	$< 10^{-9}$
F	WT	0.41 ± 0.02	21	1	0.36 ± 0.1	15	0.06
	Δ27	0.5 ± 0.04	15	$< 10^{-6}$	0.44 ± 0.04	14	0.02
	S2,11A	0.4 ± 0.02	15	0.03	0.4 ± 0.03	15	0.23

Δ27, demonstrating that FCS measurements are able to detect changes in the chromatin affinity of RCC1.

To support the assumption of the binding-diffusion model that the binding sites are immobile and that the diffusion of RCC1-nucleosome complexes does not influence the autocorrelation data, an attempt was made to measure histone H2B-EGFP mobility by FCS as a marker for nucleosome movement. At the same laser power as that used for RCC1-EGFP, H2B-EGFP fluorescence bleached quickly, precluding an analysis of nucleosome mobility (figure 4.7). This result demonstrates that nucleosomes are immobile on the timescale of an FCS experiment.

The binding-diffusion model predicts that the two components of the correlation curve reflect diffusion and a dissociation reaction, respectively. The diffusion constant and the dissociation rate constant are both temperature-dependent, but should respond differently to changes in the temperature as is outlined in the following paragraph. This difference in the temperature-dependence can potentially be used to differentiate between the contribution of the two processes to the correlation curves. Therefore the temperature-

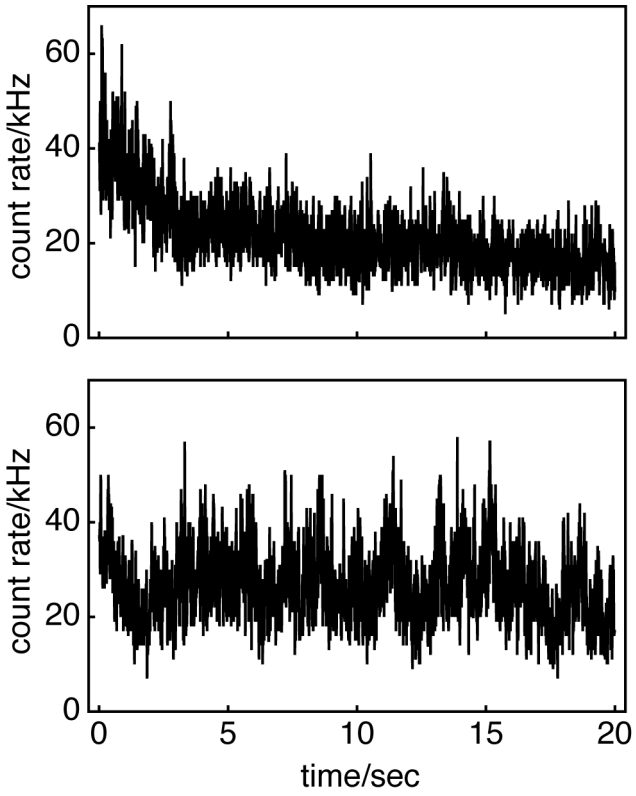

Figure 4.7: FCS measurements on histone H2B-EGFP show a fast bleaching of the H2B-EGFP fluorescence (top), which indicates that nucleosomes are immobile on the timescale of the FCS experiment. Under the same conditions, the fluorescence of RCC1-EGFP is stable (bottom). Both measurements were taken at the same laser power in nuclei of HeLa cells.

dependence of the correlation curves was analyzed to verify the assumptions of the binding-diffusion model.

The diffusion constant is proportional to temperature, $D = RT/N_A f$, where T is the absolute temperature, R is the gas constant, f is the frictional force, and N_A is Avogadro's number. In contrast, the rate constant of a chemical reaction is an exponential function of temperature, $k = A \exp(-E_a/RT)$, where A is called the pre-exponential factor, E_a is the activation energy for the reaction, and T is the absolute temperature. For small temperature changes $\Delta T = T - T_0$, the resulting changes in D or k can be approximated by a Taylor series and the relative changes $\Delta D/D_0$ and $\Delta k/k_0$ are given by:

$$\frac{\Delta D}{D_0} = \frac{\Delta T}{T_0} \qquad \text{and} \qquad \frac{\Delta k}{k_0} = \frac{E_a}{RT_0}\frac{\Delta T}{T_0} \tag{4.4}$$

Consequently, the relative change in k_{off} will be a factor of E_a/RT_0 bigger than the relative change in D, assuming that the activation energy is larger than the thermal energy.

Diffusion constants and dissociation rate constants of RCC1-EGFP were measured in nuclei of HeLa cells at different temperatures ranging from 22°C to 37°C (relative change of $\Delta T/T_0 = 0.05$ in the absolute temperature). No significant change in D could be observed in this temperature range, with $D = 7.30 \pm 1.54\,\mu\text{m}^2\,\text{s}^{-1}$ ($n = 9$) at 22°C, and $D = 7.24 \pm 1.06\,\mu\text{m}^2\,\text{s}^{-1}$ ($n = 8$) at 37°C. Similarly, the diffusion constant of EGFP did not change significantly over the same temperature range. In contrast to the diffusion constant, k_{off} increased significantly from $2.96 \pm 0.69\,\text{s}^{-1}$ ($n = 9$) at 22°C to $4.61 \pm 1.22\,\text{s}^{-1}$ ($n = 8$) at 37°C (figure 4.8). Based on the observed relative change of $\Delta k/k_0 = 0.56$, the dissociation has an estimated activation energy of $27.5\,\text{kJ}\,\text{mol}^{-1}$.

The fact that the measured k_{off} is more sensitive to changes in temperature than the measured D agrees with the assumption of the binding-diffusion model that it is a kinetic process that is reflected in the second component of RCC1-EGFP autocorrelation curves while a diffusive process is reflected in the first component.

To conclude, several observations support the interpretation of FCS data with the binding-diffusion model: First, reducing chromatin affinity by deleting the N-terminal DNA-binding site renders the chromatin interaction less stable and results in a strongly increased k_{off} while it affects the measured diffusion constant only slightly. Second, diffusion of binding sites does not affect the autocorrelation measurements as it is unlikely to occur on the timescale of an FCS experiment. Third, an analysis of the temperature dependence of autocorrelation data suggests that the two observed autocorrelation components represent a diffusive and a kinetic process, respectively.

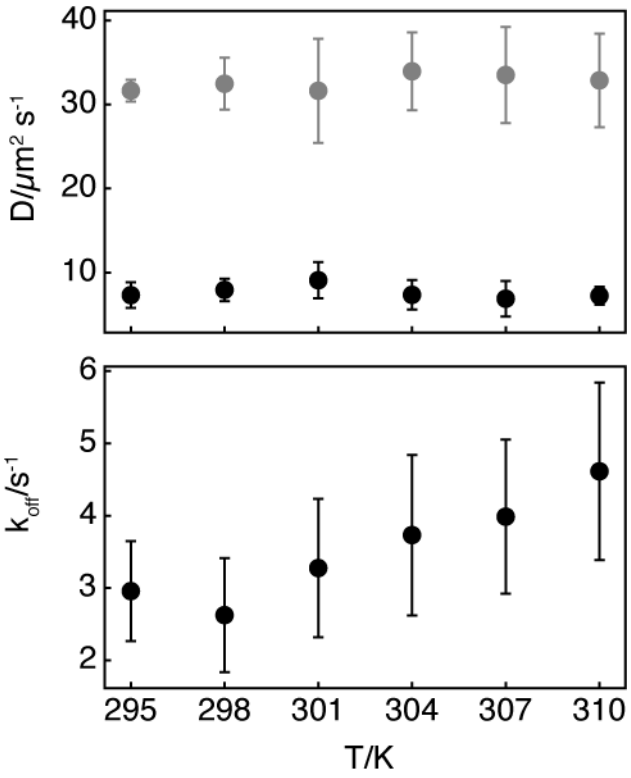

Figure 4.8: The mobility of RCC1-EGFP and EGFP was measured in nuclei of HeLa cells at different temperatures. To calculate mobility parameters, RCC1-EGFP correlation curves were fit with the binding-diffusion model while EGFP correlation curves were fit with a model for free diffusion. Top panel: The diffusion constant of RCC1-EGFP (black) and EGPF (grey) as a function of temperature. Bottom panel: The dissociation rate constant of RCC1-EGFP as a function of temperature. The error bars indicate the standard deviation from measurements in at least 4 cells.

RCC1 mobility during mitosis

To address the question whether RCC1's chromatin affinity is regulated during the cell cycle, autocorrelation measurements of RCC1-EGFP were performed on chromatin of HeLa cells during metaphase of mitosis. Fitting this autocorrelation data with the binding-diffusion model yielded $D = 6.28 \pm 2.3\,\mu\mathrm{m}^2\,\mathrm{s}^{-1}$, $k_{\mathrm{off}} = 2.43 \pm 1.44\,\mathrm{s}^{-1}$, and $F = 0.36 \pm 0.01$ ($n = 15$). When the fitting results for interphase and mitosis were submitted to a mean difference test, the difference in k_{off} was found to be significant (p-value $< 10^{-5}$), while the differences in D and F were not. This result indicates that RCC1's residence time on chromatin is cell-cycle regulated, and that the RCC1-chromatin interaction is more stable during mitosis compared to interphase. The diffusion constant is not affected by cell-cycle dependent regulation, indicating that dynamics of the immobilized state of RCC1 are regulated specifically. Furthermore, the measured free fraction is also unaffected, indicating an increase in the association rate constant. Importantly, the unbound fraction determined by FCS does not agree with the results of the quantitative imaging experiment, a discrepancy that is discussed in more detail in section 5.1.

RCC1-Δ27-EGFP also showed a more stable chromatin interaction during mitosis. Fitting data of RCC1-Δ27-EGFP on mitotic chromatin yielded $D = 7.36 \pm 2.08\,\mu\mathrm{m}^2\,\mathrm{s}^{-1}$, $k_{\mathrm{off}} = 5.39 \pm 2.23\,\mathrm{s}^{-1}$, and $F = 0.44 \pm 0.04$ ($n = 14$). Thus, even RCC1-Δ27 experiences a twofold decrease in its dissociation rate constant during mitosis similar to the wildtype protein, although its interaction with chromatin is still weaker overall. This indicates that whatever mechanism stabilises the chromatin interaction during mitosis does not depend on the N-terminus of RCC1.

This also argues against a regulatory effect of phosphorylation of N-terminal serine residues. Indeed, the non-phosphorylatable mutant RCC1-S2,11A did not show any differences to wildtype RCC1 in chromatin-binding dynamics, neither in interphase ($D = 8.1 \pm 2.58\,\mu\mathrm{m}^2\,\mathrm{s}^{-1}$, $k_{\mathrm{off}} = 3.82 \pm 1.15\,\mathrm{s}^{-1}$, $F = 0.4 \pm 0.02$, $n = 15$), nor during mitosis ($D = 7.59 \pm 1.8\,\mu\mathrm{m}^2\,\mathrm{s}^{-1}$, $k_{\mathrm{off}} = 2.0 \pm 0.66\,\mathrm{s}^{-1}$, $F = 0.4 \pm 0.03$, $n = 15$).

Mobility of the RCC1 N-terminus

Due to its interaction with chromatin, NT-GFP is expected to display two autocorrelation components in FCS measurements. However, autocorrelation curves recorded on mitotic chromatin, as well as those recorded in nuclei or in the mitotic cytoplasm, could be fit with a model for free diffusion (figure 4.9), indicating that the apparent mobility of NT-GFP is similar to a

Table 4.4: Apparent diffusion constants of NT-EGFP measured in different compartments of HeLa cells. Mean ± standard deviation from n cells. The p-value gives the result of a mean difference test comparing the given sample to NT-GFP in interphase nuclei.

	$D/\mu\mathrm{m}^2\,\mathrm{s}^{-1}$	n	p-value
NT-GFP			
Nucleus	16.8 ± 4.06	15	1
Mitotic chromatin	12.9 ± 5.32	10	0.05
Mitotic cytoplasm	17.94 ± 2.83	10	0.45
NT-K4Q-GFP			
Nucleus	23.33 ± 3.2	6	0.002

freely diffusing protein. This yielded diffusion constants of $16.8 \pm 4.06\,\mu\mathrm{m}^2\,\mathrm{s}^{-1}$ ($n = 15$) in nuclei, $12.9 \pm 5.32\,\mu\mathrm{m}^2\,\mathrm{s}^{-1}$ ($n = 10$) on mitotic chromatin, and $17.94 \pm 2.83\,\mu\mathrm{m}^2\,\mathrm{s}^{-1}$ ($n = 10$) in mitotic cytoplasm (table 4.4). Although the diffusion on mitotic chromatin was 23% slower than in interphase nuclei, a mean difference test failed to detect a significant difference between the two compartments given the current statistics ($p-$value $= 0.05$, the threshold for significance being at $p-$value $= 0.01$). The diffusion constants in interphase nuclei and mitotic cytoplasm were not significantly different ($p-$value $= 0.45$).

Based on its diffusion constant in the mitotic cytoplasm, NT-GFP diffuses as fast as a 216 kDa particle, which is in good agreement with the expected size of a NT-GFP-importin α/β complex (183 kDa), indicating that NT-GFP does form such a complex in the mitotic cytoplasm.

The fact that only a single mobility component can be distinguished on chromatin despite the chromatin-binding of NT-GFP can be explained in two ways. NT-GFP could either interact very transiently with chromatin, with a k_{off} so rapid, that the autocorrelation curves are dominated by diffusion (section 3.3). Alternatively, a fraction of NT-GFP could be stably chromatin-associated, but could be mobile while bound to chromatin and could undergo one-dimensional diffusion along the chromatin fibres. In this case, diffusion of bound and unbound NT-GFP would have to be equally fast in order to produce a single component autocorrelation curve. A further discussion of this model is presented in section 5.1.

Mutation of the lysine residue at position 4 to glutamic acid (NT-K4Q) results in a loss of chromatin accumulation during mitosis (figure 4.10), indi-

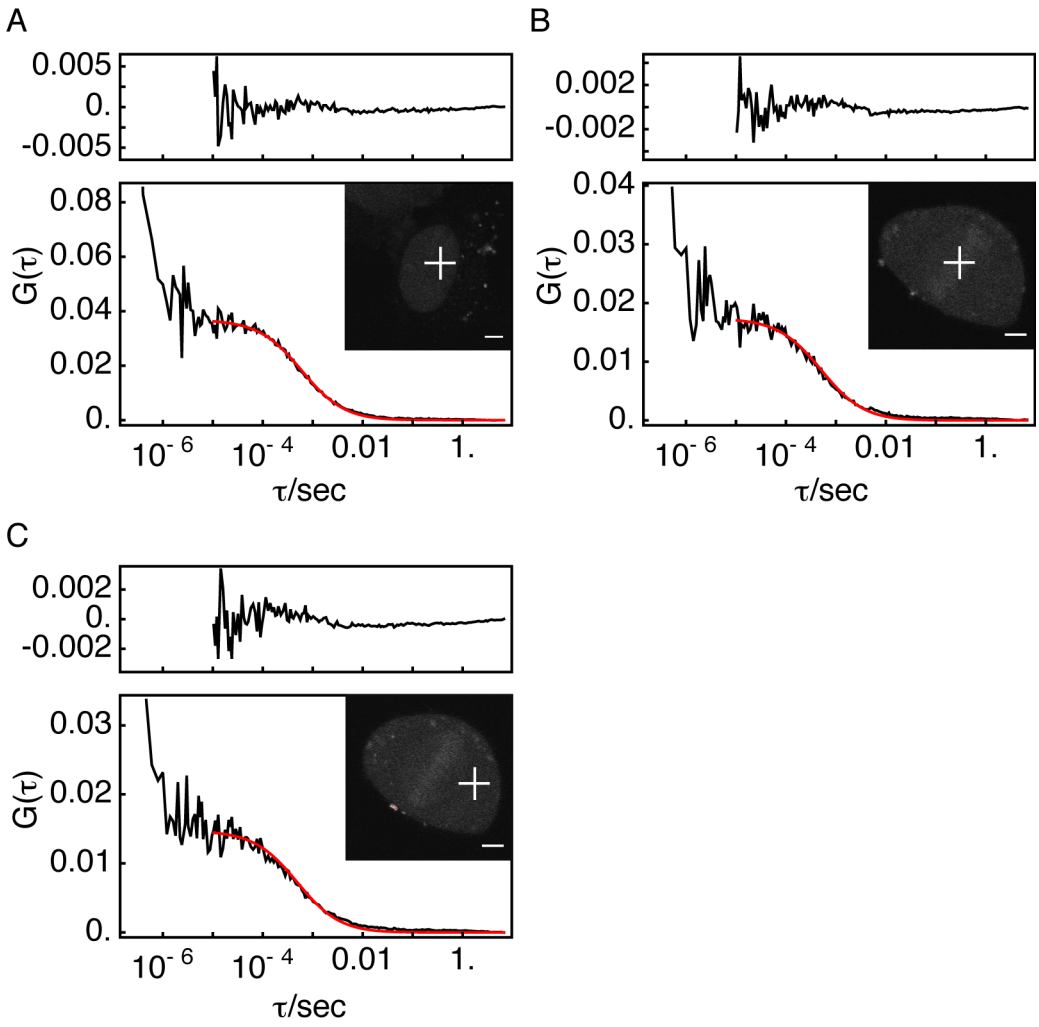

Figure 4.9: Representative autocorrelation curves of NT-GFP measured in the nucleus of an interphase HeLa cell (A), on the chromatin of a HeLa cell in metaphase (B), and in the cytoplasm of a HeLa cell in metaphase (C). All data were fit with a model for free diffusion. The upper panel of each graph shows the fit residuals. Insets show confocal images of the measured cells, where the white crosses indicate the measurement positions. Scale bars: 5 μm

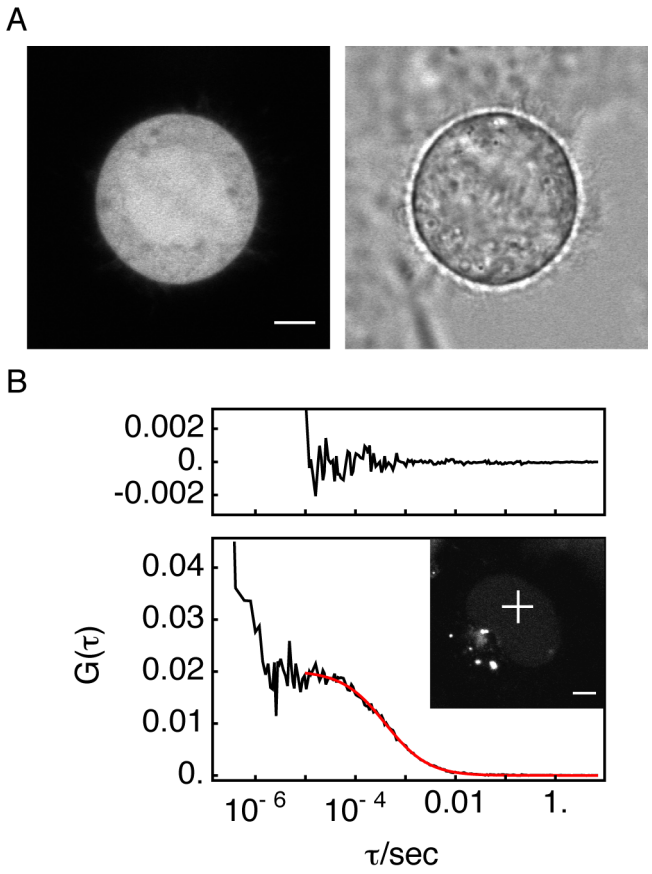

Figure 4.10: A: Confocal images of a HeLa cell expressing NT-K4Q-EGFP during metaphase of mitosis. Scale bar: 5 μm. B: Autocorrelation curve of NT-K4Q-EGFP measured in the nucleus of a HeLa cell during mitosis. The curve was fit with a model for simple diffusion. Upper panel shows fit residuals.

cating that chromatin-association of NT-GFP requires N-terminal methylation [104]. The mutant NT-K4Q-GFP also diffused significantly faster than NT-GFP in nuclei ($D = 23.33 \pm 3.2\,\mu m^2\,s^{-1}$, $p-$value $= 0.002$, $n = 6$), which agrees with the hypothesis that chromatin-binding affects diffusion of NT-GFP.

4.3 Interaction of RCC1 and Ran

Colocalization experiments with RCC1 and the nucleotide-free Ran mutant Ran T24N have indicated that the binary complex of RCC1 and nucleotide-free Ran has a strong affinity to chromatin [107]. The binary complex is an intermediate of the nucleotide-exchange reaction and its localisation to chromatin would effectively spatially restrict the production of active Ran to chromatin.

4.3.1 Mobility of Ran

The hypothesis that the binary complex of Ran and RCC1 binds to chromatin predicts that a fraction of Ran should be immobilized on chromatin and should display mobility characteristics similar to RCC1. To test this prediction, FCS measurements were performed with EGFP-tagged human Ran (EGFP-Ran) expressed in HeLa cells. Autocorrelation curves of EGFP-Ran recorded in nuclei of interphase cells lacked the prominent second component that was characteristic of RCC1-EGFP (figure 4.11 A). Nevertheless, a model for free diffusion did not fit the data as well as the binding-diffusion model. An F-test was used to decide whether the binding-diffusion model gave a significantly better fit than the model for free diffusion. The F-test yielded an average p-value of 10^{-24}, rejecting the null hypothesis that the binding-diffusion model does not provide a significantly better fit than the model for free diffusion. In contrast, the null hypothesis could not be rejected for measurements of EGFP in the nucleus ($p-$value $= 0.73$), indicating that EGFP diffusion in the nucleoplasm was adequately described by diffusion. For EGFP-Ran in the cytoplasm ($p-$value $= 2 \cdot 10^{-7}$) and EGFP in the cytoplasm ($p-$value $= 7 \cdot 10^{-5}$) the null hypothesis was rejected, albeit with a much lower confidence than for EGFP-Ran in the nucleus.

The fact that the binding-diffusion model performed better than the model for free diffusion for cytoplasmic measurements suggests that the diffusion-only model does not fully account for the dynamics of EGFP and EGFP-Ran in the cytoplasm. However, the binding-diffusion model can be rejected in this case, because it is not physically meaningful for EGFP in the cytoplasm. On the other hand, comparison of EGFP and EGFP-Ran in the nucleus strongly

Table 4.5: Mobility parameters for EGFP-Ran and EGFP-RanT24N. Mobility parameters in the nucleus were determined by fitting the binding diffusion model to autocorrelation data. Diffusion in the cytoplasm was quantified by fitting a model for free diffusion. Mean ± standard deviation from n cells.

	$D/\mu\mathrm{m}^2\,\mathrm{s}^{-1}$	$k_{\mathrm{off}}/\mathrm{s}^{-1}$	F	n
Ran				
Cytoplasm	16.05 ± 3.7			10
Nucleus	14.33 ± 1.57	53.15 ± 22.7	0.85 ± 0.05	10
RanT24N				
Nucleus	11.21 ± 3.16	6.57 ± 1.46	0.5 ± 0.05	10

supports the hypothesis that Ran mobility is different from EGFP mobility in the nucleus.

Analysis of EGFP-Ran in the nucleus yielded $D = 14.33 \pm 1.57\,\mu\mathrm{m}^2\,\mathrm{s}^{-1}$, $k_{\mathrm{off}} = 53.15 \pm 22.7\,\mathrm{s}^{-1}$, and $F = 0.85 \pm 0.05$ ($n = 10$, table 4.5). This suggests that a small fraction of EGFP-Ran is transiently immobilized by binding to chromatin, however, with a considerably higher dissociation rate constant than RCC1. The large variance in k_{off} might either reflect the uncertainty of the curve fitting procedure caused by the small contribution of the bound fraction to the total autocorrelation amplitude, or it might represent cell-to-cell or spatial variation of the Ran-chromatin interaction. In the cytoplasm, the apparent diffusion constant of EGFP-Ran was $D = 16.05 \pm 3.7\,\mu\mathrm{m}^2\,\mathrm{s}^{-1}$ ($n = 10$). A mean difference test did not detect a significant difference in the diffusion constants between cytoplasm and nucleus ($p-\mathrm{value} = 0.2$).

The mutant RanT24N had a considerably different mobility than wildtype Ran with a marked slow autocorrelation component (figure 4.11 B), suggesting that it strongly interacts with chromatin. Analysis with the binding-diffusion model yielded $D = 11.21 \pm 3.16\,\mu\mathrm{m}^2\,\mathrm{s}^{-1}$, $k_{\mathrm{off}} = 6.57 \pm 1.46\,\mathrm{s}^{-1}$, and $F = 0.5 \pm 0.05$ ($n = 10$, table 4.5). Consistent with its proposed binding to chromatin, RanT24N accumulates in the nucleus and on mitotic chromatin to a higher degree than wildtype Ran (figure 4.11 C).

These data support the model that Ran is recruited to chromatin in living cells. As the example of the T24N mutant shows, there is a correlation between affinity for RCC1 and a reduction in mobility, arguing that the interaction with RCC1 results in a localization of Ran to chromatin. In interphase cells however, only a small steady-state fraction of wildtype Ran is transiently immobilized.

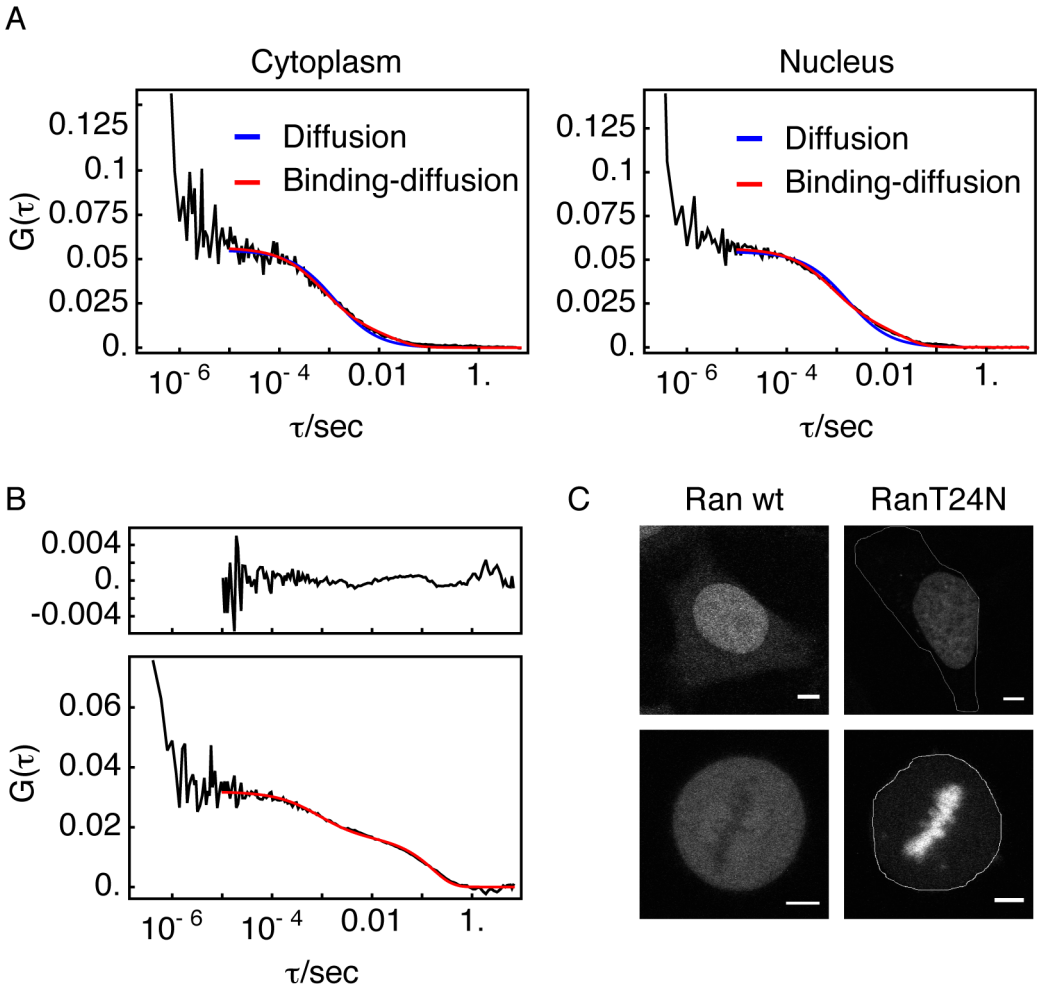

Figure 4.11: A: Autocorrelation curves of EGFP-Ran recorded in the cytoplasm (left) or the nucleus (right) of HeLa cells during interphase were fit with either a model for free diffusion (blue) or the binding diffusion model (red). B: Autocorrelation curve of EGFP-RanT24N recorded in the nucleus of an interphase HeLa cell and fit with the binding diffusion model. The upper panel shows the fit residuals. C: Confocal images of HeLa cells expressing either EGFP-Ran (left column) or EGFP-RanT24N (right column) during interphase (top row) or mitosis (bottom row). Cell borders are outlined by a thin white line. Scale bars: 5 μm.

Table 4.6: Mobility parameters of mCherry-Ran or mCherry-RanT24N in interphase nuclei and on mitotic chromatin determined from fits of the binding diffusion model. Mean ± standard deviation from n cells. Samples from interphase nuclei and mitotic chromatin were compared using a mean difference test.

		Nucleus		Mitotic chromatin		
		mean ± SD	n	mean ± SD	n	$p-$value
$D/\mu\mathrm{m}^2\,\mathrm{s}^{-1}$	WT	12.24 ± 4.25	20	14.19 ± 8.16	8	0.54
	T24N	10.77 ± 6.04	13	27.16 ± 25.81	11	0.06
$k_{\mathrm{off}}/\mathrm{s}^{-1}$	WT	42.65 ± 25.64	20	39.76 ± 22.26	8	0.78
	T24N	5.31 ± 1.39	13	0.97 ± 0.58	11	$< 10^{-7}$
F	WT	0.81 ± 0.08	20	0.71 ± 0.07	8	0.005
	T24N	0.41 ± 0.09	13	0.32 ± 0.08	11	0.01

Also, the interaction of wildtype Ran with chromatin is much more transient than that of RCC1 with chromatin.

To test whether the mobility of Ran and RanT24N is also subject to cell-cycle dependent regulation as in the case of RCC1, autocorrelation data of of mCherry-Ran and mCherry-RanT24N from interphase nuclei and mitotic chromatin were fit with the binding-diffusion model (table 4.6). The data from interphase nuclei for the mCherry-tagged proteins were in good agreement with those for the EGFP-tagged proteins. For wildtype Ran, a significant reduction in the free fraction was observed, from 0.81 ± 0.09 in interphase to 0.71 ± 0.07 in mitosis ($n = 20$, $n = 8$, respectively, $p-$value $= 0.005$). No significant difference in D and k_{off} was detected. In the case of mCherry-RanT24N, the dissociation rate constant was significantly smaller in mitosis than in interphase, decreasing from $5.31 \pm 1.39\,\mathrm{s}^{-1}$ to $0.97 \pm 0.58\,\mathrm{s}^{-1}$ ($n = 13$, $n = 11$, $p-$value $< 10^{-7}$).

4.3.2 Complex formation of Ran and RCC1

To directly measure the interaction of Ran and RCC1, dual-colour fluorescence crosscorrelation spectroscopy (FCCS) measurements were preformed in cells coexpressing RCC1-EGFP with either mCherry-Ran, or mCherry-RanT24N (figure 4.12 A and B). Measurements were taken either in nuclei during interphase or on chromatin during metaphase of mitosis.

FCCS measurements are complicated by effects such as an incomplete spectral separation of the fluorescent dyes and an imperfect overlap of the observation volumes of each channel. The former results in false positive crosscorrelation because fluctuations of the EGFP-labelled component are also detected in the mCherry channel. The latter reduces the maximal crosscorrelation signal. To correct for false positive crosscorrelation, FCCS was recorded in cells coexpressing either mEGFP and RanT24N-mCherry (figure 4.12 C), or RCC1-EGFP and mCherry (figure 4.12 D). These proteins should not interact specifically with each other and therefore serve as a negative control. As positive control, a construct consisting of EGFP fused to mCherry via p38 mitogen-activated protein kinase as a linker (EGFP-p38-mCherry) was used (figure 4.12 F). Because here EGFP and mCherry are part of one molecule, this should indicate the maximal amount of cross-correlation detectable.

In the case of two chromatin-binding proteins, false positive crosscorrelation might also arise from both proteins binding independently to the same chromatin fibre. To correct for this effect, FCCS was measured in cells coexpressing histone H1-EGFP and RanT24N-mCherry, which are not known to interact specifically but both bind chromatin (figure 4.12 E).

The FCCS measurements were quantitatively analysed by calculating apparent interaction strengths (section 6.3). In short, this involves calculating an effective association constant from the amplitudes of the auto- and cross-correlation curves [122]. The apparent interaction strength was normalized between the mean interaction strength observed with the negative controls and the mean interaction strength observed with the positive control. Figure 4.13 shows the normalized interaction strengths calculated for different samples. The samples were compared using a mean difference test.

The level of crosscorrelation detected between RCC1-EGFP and mCherry-Ran was only slightly higher than the level of crosscorrelation in the negative controls (figure 4.13). The difference to the negative control was not significant on mitotic chromatin (mean $\pm$ standard deviation of the normalized interaction strength 0.007 ± 0.01, $n = 8$, $p-$value $= 0.05$) and only slightly significant in interphase nuclei (normalized interaction strength 0.008 ± 0.009, $n = 18$, $p-$value $= 0.007$), indicating that the interaction of wildtype Ran with RCC1 could not be detected with satisfactory accuracy.

In contrast, there was a strong crosscorrelation between RCC1-EGFP and mCherry-RanT24N in interphase nuclei (normalized interaction strength 0.1 ± 0.04, $n = 14$) and on mitotic chromatin (normalized interaction strength 0.04 ± 0.04, $n = 12$). Both samples were significantly different from the negative controls (p-values $4 \cdot 10^{-7}$ and 0.004, respectively). However, a considerable crosscorrelation signal was also observed between histone H1-EGFP

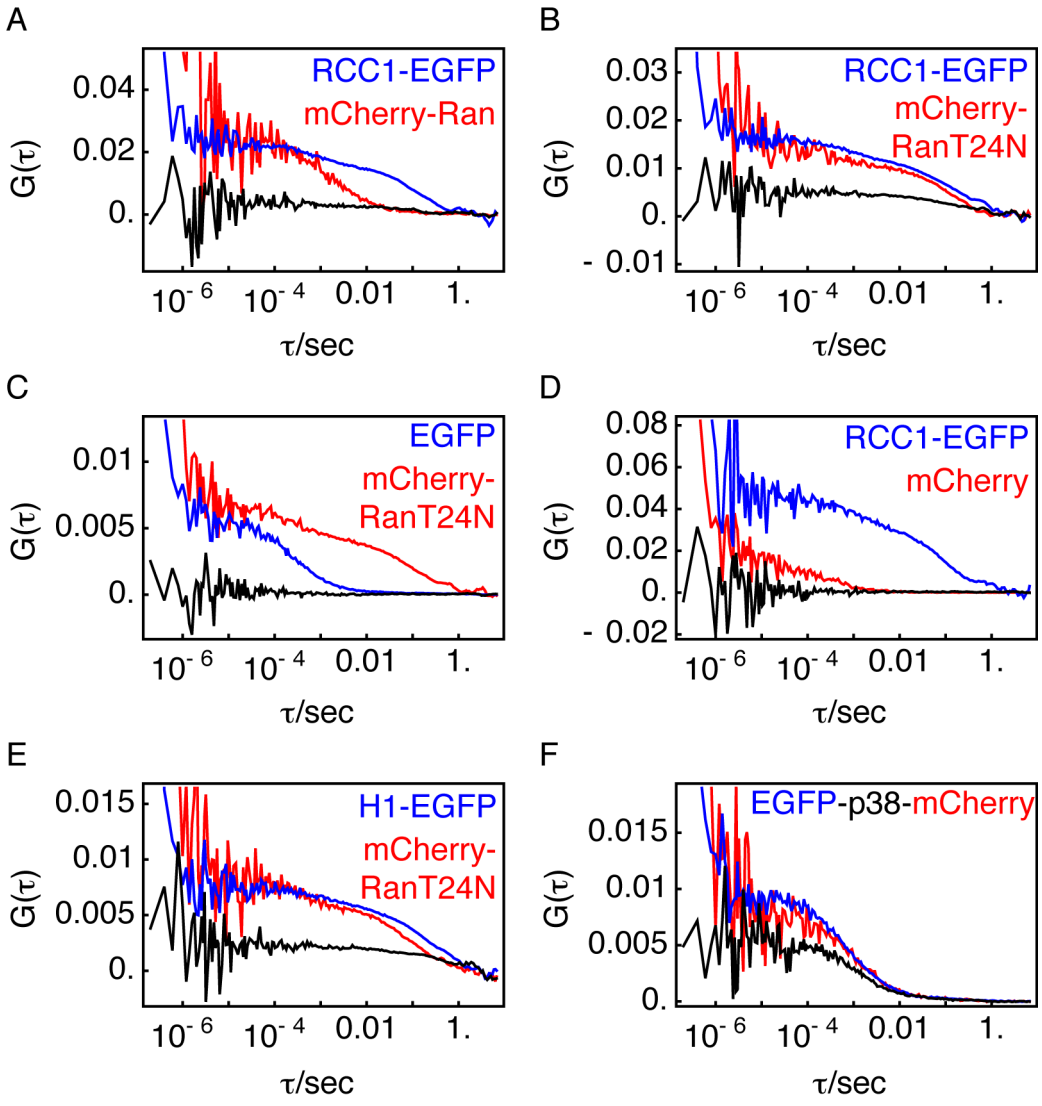

Figure 4.12: Representative crosscorrelation measurements showing autocorrelation curves of the EGFP channel (blue), the mCherry channel (red), and the crosscorrelation curve (black). All measurements were taken in nuclei of interphase HeLa cells coexpressing either RCC1-EGFP and mCherry-Ran (A), RCC1-EGFP and mCherry-RanT24N (B), EGFP and mCherry-RanT24N (C), RCC1-EGFP and mCherry (D), histone H1-EGFP and mCherry-RanT24N (E), or expressing EGFP-p38-mCherry (F).

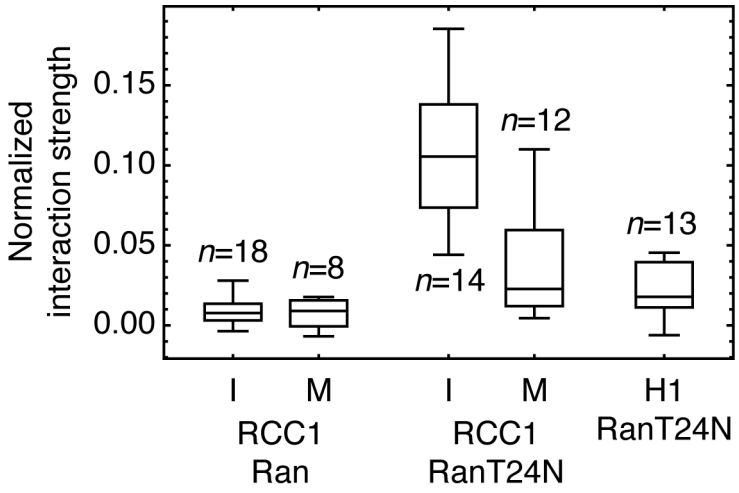

Figure 4.13: Normalized interaction strengths determined by dual-colour fluorescence cross-correlation. Measurements were taken either in interphase nuclei (I) or on mitotic chromatin (M). In the case of H1-EGFP and Cherry-RanT24N coexpression, measurements were taken in interphase nuclei only. Each box and whisker chart represents measurements from n different cells.

and mCherry-RanT24N in interphase nuclei (normalized interaction strength 0.02 ± 0.004, $n = 13$, $p-$value $= 0.0003$ compared to the negative control). There was no statistically significant difference between this signal and the normalized interaction strength of RCC1 and RanT24N during mitosis ($p-$value $= 0.16$), indicating that the crosscorrelation signal between RCC1 and RanT24N during mitosis cannot be attributed to their specific interaction unequivocally. On the other hand, the normalized interaction strength of RCC1 and RanT24N in interphase was significantly different from H1 and RanT24N ($p-$value $= 7 \cdot 10^{-7}$), supporting the conclusion that the crosscorrelation signal in interphase stems from a specific interaction. More importantly, these data suggest that the interaction of RCC1 and RanT24N is cell cycle regulated and is stronger during interphase.

4.3.3 Mobility of the Ran-RCC1 complex

Crosscorrelation curves contain information about the mobility of the complex in addition to information about its concentration [120]. The crosscorrelation data for the Ran RCC1 interaction were therefore analyzed to test the hypothesis that the Ran-RCC1 complex binds to chromatin.

Analysis of the crosscorrelation data of RCC1-EGFP and wildtype mCherry-

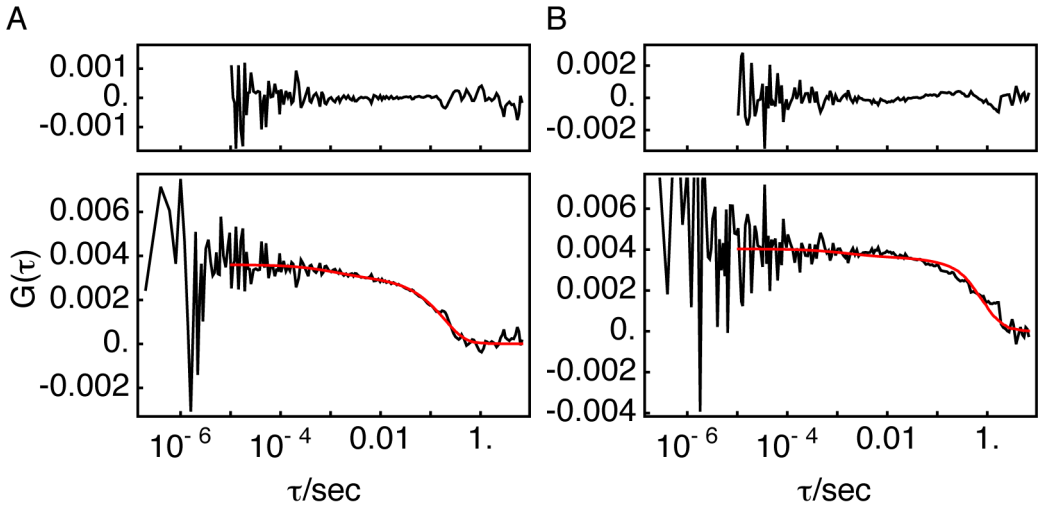

Figure 4.14: Representative crosscorrelation curves recorded in interphase nuclei (A) or on mitotic chromatin (B) of HeLa cells coexpressing RCC1-EGFP and mCherry-RanT24N. The curves were fit with the binding diffusion model (red curves) to determine the mobility of the RanT24N-RCC1 complex.

Ran was hampered by a low signal to noise ratio of the crosscorrelation curves caused by the low crosscorrelation amplitude and the apparently low concentration of the Ran-RCC1 complex. This did not allow to draw conclusions about the mobility of the complex of wildtype Ran and RCC1.

Crosscorrelation curves of RCC1-EGFP and RanT24N-mCherry, however, had a reproducibly good signal to noise ratio. Qualitatively, crosscorrelation curves were dominated by a prominent slow component with a correlation time on the order of several hundred milliseconds, indicating that most of the RanT24N-RCC1 complex is bound to chromatin (figure 4.14). However, qualitative analysis could not fully rule out any contribution from a fast component. To quantify the extent to which a possible fast component contributed to the crosscorrelation curves, the binding diffusion model was fit to the data. To fit the fast fraction accurately, the diffusion constant was limited to values between $6\,\mu\mathrm{m}^2\,\mathrm{s}^{-1}$ and $9\,\mu\mathrm{m}^2\,\mathrm{s}^{-1}$. For the RanT24N-RCC1 complex in interphase nuclei, this yielded $D = 6.9 \pm 1.13\,\mu\mathrm{m}^2\,\mathrm{s}^{-1}$, $k_{\mathrm{off}} = 3.51 \pm 1.36\,\mathrm{s}^{-1}$, and $F = 0.24 \pm 0.05$ ($n = 11$, table 4.7). Therefore, the immobilized fraction is higher for the RanT24N-RCC1 complex than for RCC1 and RanT24N separately, while the dissociation rate constant is similar in both cases. This indicates that the complex is enriched on chromatin, providing strong support for the model that the Ran-RCC1 interaction takes place preferentially

Table 4.7: Mobility parameters obtained by fitting crosscorrelation curves of RCC1-EGFP and mCherry-RanT24N by the binding diffusion model. The diffusion constant was restricted to values between $6\,\mu\mathrm{m}^2\,\mathrm{s}^{-1}$ and $9\,\mu\mathrm{m}^2\,\mathrm{s}^{-1}$, to fit the mobile fraction accurately. Mean ± standard deviation from n cells. Samples from interphase nuclei and mitotic chromatin were compared using a mean difference test.

	Nucleus		Mitotic chromatin		
	mean ± SD	n	mean ± SD	n	p-value
$D/\mu\mathrm{m}^2\,\mathrm{s}^{-1}$	6.9 ± 1.13	11	6.73 ± 0.76	4	0.79
$k_{\mathrm{off}}/\mathrm{s}^{-1}$	3.51 ± 1.36	11	0.63 ± 0.41	4	0.001
F	0.24 ± 0.05	11	0.09 ± 0.02	4	$< 10^{-4}$

on chromatin.

On mitotic chromatin, both the mobile fraction and the dissociation rate constant are decreased to $F = 0.09 \pm 0.02$ and $k_{\mathrm{off}} = 0.63 \pm 0.41\,\mathrm{s}^{-1}$ ($n = 4$). The complex is therefore almost exclusively localized on chromatin during mitosis, and displays a similar increase in its residence time as RCC1 and RanT24N alone.

5 Discussion

Formation of the Ran gradient is a reaction-diffusion process that is controlled not only by the kinetics of the biochemical reactions involved but also by the spatial distribution and the diffusional properties of its reactants [63]. Traditional biochemical approaches using purified proteins are well suited to measure kinetic reaction parameters in solution, however they cannot easily account for the effects of localization and diffusion of reactants within the cell. Fluorescence microscopy based methods on the other hand provide the spatial and temporal resolution required to study these two aspects of reaction-diffusion processes *in vivo*.

In the reaction-diffusion process that underlies the Ran gradient, chromatin acts as a structural seed by localizing active Ran, the Ran GEF RCC1 [123]. It thereby spatially partitions the two parts of the GTPase cycle, the GEF and the GAP reaction, respectively. In this thesis, I used fluorescence correlation spectroscopy to study the mobility of the chromatin-bound RCC1. This gave insight into how binding and diffusion contribute to RCC1 mobility on chromatin and in the cytoplasm. Furthermore, a potential coupling between the GEF reaction and chromatin-binding of RCC1 was investigated by measuring the mobility of Ran and the interaction between RCC1 and Ran. Finally, FCS measurements allowed to compare the dynamics of chromatin-bound RCC1 between interphase and mitosis.

5.1 Description of RCC1 mobility requires a three-state model

FCS measurements of RCC1 in living cells reveal two different components of RCC1 mobility on chromatin (figure 4.4 on page 40). A similar observation has previously been reported for the nuclear mobility of histone H1, another chromatin-binding protein, but has not been analyzed in great quantitative detail [124]. Here, I have used a binding diffusion model of RCC1 mobility to analyze FCS data. As I show in chapter 3, this model can be readily formulated on the basis of the existing theoretical framework for FCS [116, 119]. This possibility has not been discussed in the past literature, with the exception of a work on the analysis of chromatin binding of a transcription factor DNA binding domain [125].

To validate the interpretation of the FCS measurements, I compare them to two independent estimates of the steady-state fraction of unbound RCC1. The first is the quantitative imaging data presented in section 4.1, which indicates that the relative concentration of unbound RCC1 on chromatin is $5 \pm 1\%$. The second is published data of RCC1 in interphase nuclei, which estimate the relative unbound concentration to $2.1 \pm 0.6\%$ [115]. Neither estimate agrees with the results of the FCS analysis, according to which the relative unbound concentration is $41 \pm 2\%$ in interphase and $36 \pm 10\%$ in mitosis (see table 4.3 on page 45).

To resolve this discrepancy, I propose a modified model of RCC1 mobility, which distinguishes three different mobility states: Freely diffusing RCC1 that does not interact with chromatin, loosely bound RCC1 that moves along chromatin by one-dimensional diffusion, and tightly bound RCC1 that is immobilized on nucleosomes (figure 5.1 A). RCC1 mobility is thus governed by two mobile and one immobile state. Because imaging cannot distinguish between the two chromatin-bound states of RCC1, it only measures the relative concentration of unbound RCC1. FCS measurements, on the other hand, have the potential to discriminate all three states based on their mobility. The fact that only a single mobile state can be distinguished in the autocorrelation data of RCC1 suggests that the unbound and the loosely bound state have similar mobilities and/or that one of them has such a small contribution to the autocorrelation amplitude that they cannot be resolved by autocorrelation analysis. Hence, the fraction F determined by fitting of the binding-diffusion model does not indicate the relative concentration of *unbound* RCC1 but the relative concentration of *mobile* RCC1.

From imaging and FCS data, it can be calculated that the unbound state contributes only 14% to the total mobile component on mitotic chromatin. Under these conditions, the diffusion constant of the two mobile states would have to differ by a factor of ten in order to be distinguishable [126]. Since the loosely bound state is the dominant fraction of the mobile component, it is likely that the apparent diffusion constant of $6.16 \pm 1.52\,\mu\mathrm{m}^2\,\mathrm{s}^{-1}$ is a close estimate for the diffusion constant of one-dimensional diffusion. This explains why the apparent diffusion constant on chromatin is significantly different from the diffusion constant in the interphase and the mitotic cytoplasm, which is $27.11 \pm 5.35\,\mu\mathrm{m}^2\,\mathrm{s}^{-1}$ and $11.05 \pm 1.66\,\mu\mathrm{m}^2\,\mathrm{s}^{-1}$, respectively (see table 4.2 on page 43). It also offers an explanation why the apparent diffusion constant is not affected by the high density of mitotic chromatin as it is the case for EGFP (table 4.1 on page 39).

In the three-state model, RCC1 has two modes of chromatin interaction. One-dimensional diffusion in the loosely bound state probably depends on un-

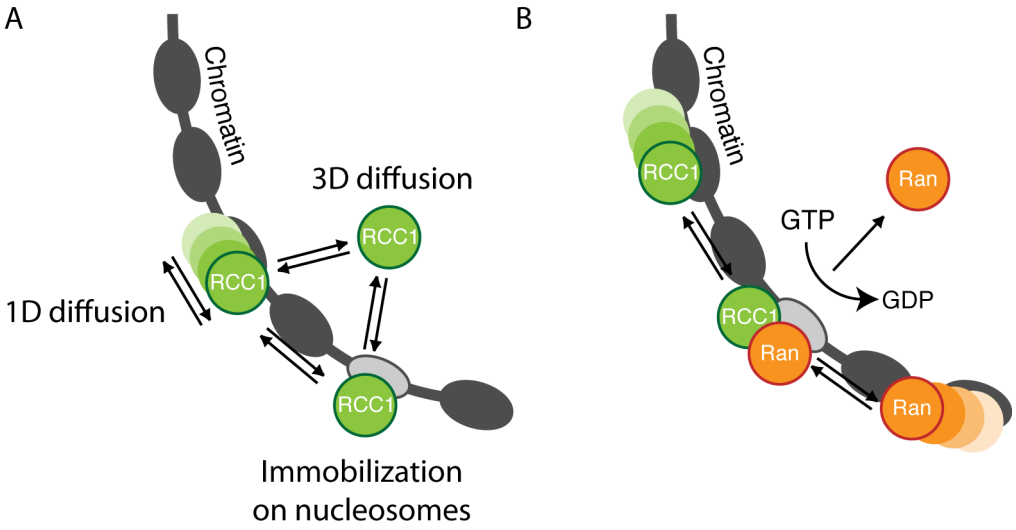

Figure 5.1: A: Three-state model of RCC1 mobility on chromatin and its interaction with Ran. B: Model for the interaction of Ran and RCC1 on chromatin.

specific and weak interactions with either the DNA or other components of chromatin. Tight binding to chromatin most likely employs specific interactions with the nucleosome such as those observed in the crystal structure of the RCC1-nucleosome complex [100]. The dissociation rate constant k_{off} describes the transition rate from the tightly bound state to either of the mobile states. Because the loosely bound state is the dominant mobile state, k_{off} probably is a measure for the transition between the two binding modes, not for complete dissociation from chromatin.

Importantly, this interpretation of the FCS data is also consistent with the observed temperature dependence of the autocorrelation components, which predicts that the fast component reflects a diffusive process while the slow component corresponds to a chemical reaction (see figure 4.8 on page 48).

The mobility of RCC1's N-terminus fused to GFP (NT-GFP) can be best explained by assuming that it lacks the ability to bind chromatin in the tightly bound state. Instead, the N-terminus of RCC1 purely mediates loose binding and one-dimensional diffusion along chromatin. Interestingly, this interaction specifically requires N-terminal methylation (table 4.4 on page 50 and figure 4.10 on page 52). In the light of this result, it would be possible that the N-terminus of RCC1 is necessary and sufficient to mediate one-dimensional diffusion along chromatin. However, the data on RCC1Δ27 refutes this idea. With an unbound fraction of $14 \pm 2\%$ and a mobile fraction of $44 \pm 4\%$ on

mitotic chromatin, the loosely bound state still makes the largest contribution to the mobile component. This shows that one-dimensional diffusion is not solely mediated by the N-terminal DNA binding site.

To conclude, the comparison of quantitative imaging and FCS measurements demonstrates that a two state binding diffusion model is insufficient to describe RCC1 mobility. Instead, the data provide strong support for a three-state model of RCC1 mobility, in which one-dimensional diffusion along chromatin is a major determinant of mobility.

One-dimensional diffusion along DNA has been directly observed for example for the *lac* repressor *in vivo* and a DNA repair factor *in vitro* [127, 128]. In the case of site-specific proteins, one-dimensional diffusion is a mechanism to increase the speed at which the protein finds its binding site. The combination of three- and one-dimensional diffusion is referred to as facilitated diffusion and can increase the association rate above the diffusion limit [129]. One-dimensional diffusion therefore provides an advantage in a situation where a protein needs to search the large volume of the cell nucleus for a single binding site. RCC1 does not need to scan the genome for a specific binding site, since it associates with nucleosomes unselectively [130]. However, one-dimensional diffusion along chromatin might have a functional significance by enhancing the interaction between RCC1 and Ran (see next section).

It is an interesting question why measurement of RCC1 mobility in a photoactivation experiment does only distinguish unbound from bound RCC1, but does not detect the large fraction of mobile RCC1 [115]. In a photoactivation experiment, the redistribution of fluorescence is measured over a length scale of the size of the nucleus, i.e. several μm. FCS, in contrast, measures protein dynamics in a diffraction-limited volume, i.e. on length scales of less than 1 μm. The movement of loosely bound RCC1 might therefore be spatially confined such that it cannot contribute to the redistribution of fluorescence across the nucleus. This agrees with the expectation that a given chromatin fibre is not an elongated track traversing the whole nucleus, but might be folded inside a compact volume element.

5.2 The GEF reaction is coupled to chromatin

If chromatin binding and the guanine exchange reaction were coupled, Ran should be immobilized on chromatin and the k_{off} of the Ran-chromatin interaction should be similar to the rate of the nucleotide exchange reaction.

FCS measurements reveal that Ran mobility has two components on chromatin (figure 4.11 on page 55), consistent with previous data [131]. Analysis of

the FCS data with the binding diffusion model indicates that a 15±5% fraction of Ran is bound to chromatin with a dissociation rate constant of $53 \pm 23\,\mathrm{s}^{-1}$ (table 4.5 on page 54). The rate of nucleotide exchange measured *in vitro* is $14.9\,\mathrm{s}^{-1}$, with the rate limiting step being the nucleotide dissociation [94]. If one considers that the nucleotide dissociation rate is stimulated twofold in the presence of histones, the *in vivo* rate of nucleotide exchange might be as high as $30\,\mathrm{s}^{-1}$ [103]. It is therefore of similar order of magnitude as the dissociation rate constant of the Ran-chromatin interaction, which is consistent with the model that the nucleotide exchange takes places while Ran is immobilized on chromatin.

Increasing the affinity for RCC1 by the T24N mutation, recruits Ran to chromatin. This is apparent in mitotic cells, where RanT24N accumulates on chromatin, but also in interphase, where RanT24N accumulates in the nucleus. It is also evident from the autocorrelation data, which show a more dominant slow component as compared to wildtype Ran. Analysis of RanT24N mobility with the binding diffusion model yields a dissociation rate constant of $5.31 \pm 1.39\,\mathrm{s}^{-1}$ (table 4.6 on page 56). This is comparable to the *in vitro* dissociation rate constant of the RanT24N-RCC1 complex, which can be estimated to be on the order of $2\,\mathrm{s}^{-1}$ on the basis of the K_D of the interaction between nucleotide-free Ran and RCC1 (25 nM) and the association rate constant of nucleotide-bound Ran and RCC1 ($74\,\mu\mathrm{M}^{-1}\,\mathrm{s}^{-1}$) [94].

Taken together, the FCS measurements are consistent with the model that Ran interacts with RCC1 on chromatin and dissociates from chromatin when the exchange reaction is complete. It also suggests that Ran's affinity for RCC1 determines its residence time on chromatin, in which case one could quantify the dissociation rate constant of RCC1 and Ran by measuring the residence time of Ran on chromatin. Because the k_{off} of the Ran-chromatin interaction is slightly faster than the *in vitro* k_{off} of the Ran-RCC1 interaction both in the case of wildtype Ran and RanT24N, it might be speculated that the nucleotide exchange reaction is faster in living cells than expected from *in vitro* experiments. This would agree well with the reported stimulation of the exchange reaction by nucleosomes [103].

Additional support for this model of the Ran-RCC1 interaction comes from an analysis of the mobility of the RanT24N-RCC1 complex by crosscorrelation measurements (section 4.3.3 on page 59). Quantitative analysis of the crosscorrelation data indicates that most of the complex is immobilized on chromatin with a dissociation rate constant of $3.51 \pm 1.36\,\mathrm{s}^{-1}$ (table 4.7 on page 61), while only a fraction of approximately 25% (in interphase) is mobile. This suggests that nucleosomes serve as specific sites on which the nucleotide exchange reaction takes place.

This suggests the following speculative mechanism (figure 5.1 B): Ran associates with loosely bound RCC1, that undergoes one-dimensional diffusion on chromatin. The trimeric complex binds tightly to a nucleosome. On the nucleosome, the nucleotide exchange reaction takes place. Ran dissociates from chromatin upon nucleotide binding.

This mechanism has two major implications: First, it spatially restricts the activation of Ran to chromatin. As has been put forward previously, this might be important in formation of the Ran gradient, since it ensures the partitioning of the the GEF and the GAP reactions [107]. Second, the association of Ran with chromatin-bound RCC1 can be compared to interaction of proteins at the plasma membrane that play an important role in signal transduction from plasma membrane bound receptors. In this context, Kholodenko *et al.* localizing *both* interaction partners to the membrane increases their encounter rate [132]. This can increase the turnover rate of a reaction-limited process. For Ran and RCC1 this would indicate that Ran first binds to chromatin and then associates with RCC1. Indeed, RCC1-independent binding of Ran to chromatin via histones H3/H4 has been demonstrated [108]. I therefore conclude that localization of the GEF reaction to chromatin, stimulates the nucleotide-exchange rate by increasing the association rate of Ran and RCC1 and by a nucleotide-dependent stimulation of the nucleotide dissociation rate.

5.3 RCC1 binds to macromolecular complexes in the mitotic cytoplasm

With a diffusion constant of $11.05 \pm 1.66\,\mu\mathrm{m}^2\,\mathrm{s}^{-1}$, the mobility of RCC1 is significantly lower in the mitotic cytoplasm than in the interphase cytoplasm (table 4.2 on page 43). This indicates that cytoplasmic RCC1 binds to macromolecular complexes specifically during mitosis, and suggests that the measured diffusion constant is the apparent diffusion constant of a mixture of bound and unbound RCC1. RCC1 has been shown to interact with importin α (see the discussion in section 2.2.2 on page 16) as well as with the nucleoporin Nup98 [133].

Two observations support the model that at least a fraction of cytoplasmic RCC1 is bound to a complex of importin α/β. First, removing the N-terminal NLS results in an increase of the diffusion constant to $16.47 \pm 1.41\,\mu\mathrm{m}^2\,\mathrm{s}^{-1}$. Interestingly, this does not result in a complete shift of the RCC1 population to the unbound state, which hints at a NLS-independent interaction of RCC1 with other binding partners. Second, the diffusion constant of RCC1 S2,11A is decreased to $7.88 \pm 1.41\,\mu\mathrm{m}^2\,\mathrm{s}^{-1}$. This is consistent with an increase in

the fraction of importin bound RCC1 that should be induced by preventing phosphorylation of the N-terminal serine residues.

If importin binding was the major determinant of RCC1 mobility in the cytoplasm, a RCC1 mobility gradient should exist, as less RCC1 should be importin-bound in the vicinity of chromatin. This gradient, however, could not be unequivocally detected by FCS measurements (figure 4.6 on page 44). I therefore propose that binding to nucleoporins also contributes to the decreased mobility of RCC1. As nucleoporins are distributed on the endoplasmic reticulum during mitosis, it is possible that there is a homogeneous distribution of low affinity binding sites throughout the mitotic cytoplasm, which slows RCC1 diffusion. This model is consistent with the observation that RCC1 mobility is not affected by complex formation in the interphase cytoplasm and with the estimated size of the macromolecular complex in mitosis (932 kDa, see analysis on page 42), which is too large for a trimeric complex of RCC1 and importins α/β alone.

In summary, RCC1 binds to both importins and other macromolecular complexes, for example nucleoporins, in the mitotic cytoplasm. In the interphase cytoplasm, no interaction between importins and RCC1 can be detected on the basis of RCC1's mobility, despite the fact that the importin-interaction is required for nuclear import of RCC1. The RCC1-importin $\alpha 3$ might therefore be spatially regulated during interphase, for example it might only occur close to the nuclear envelope. More carefully spatially resolved FCS measurements might provide further information on this question.

What is the functional significance of the importin-interaction during mitosis? Importin-binding competes with binding of RCC1 to chromatin [93]. During mitosis, this could have a negative effect on the formation of the Ran gradient, since it could cancel out the spatial partitioning of RCC1 and RanGAP by concentrating RCC1 in the cytoplasm. Especially after nuclear envelope breakdown, when the chromatin is exposed to the large cytoplasmic volume, the cell therefore needs a mechanism to prevent the potential shift in equilibrium from chromatin-bound to importin-bound RCC1. Dissociation of RCC1 from importin α/β by GTP-bound Ran can be regarded as a positive feedback mechanism to prevent this, as chromatin-bound RCC1 activates Ran and thereby promotes its own chromatin localization. N-terminal phosphorylation of RCC1 is another mechanism to prevent importin binding [98, 99]. This is confirmed by my observations on the cytoplasmic mobility of RCC1 S2,11A. For this reason I propose, that phosphorylation of RCC1 by Cdk1 at the onset of mitosis complements the Ran-mediated positive feedback and is a safeguard mechanism to maintain chromosomal localization of RCC1 during mitosis. Judging from the different mobility of wildtype RCC1 and RCC1Δ27,

only a fraction of RCC1 is phosphorylated and unable to bind importin α3. In the presence of the Ran-mediated feedback, phosphorylation does not have to be complete, since it is only needed to prevent a loss of RCC1 from chromatin at the onset of mitosis. Once sufficient RCC1 is localized on chromatin, the constant production of active Ran will ensure RCC1's localization. Phosphorylation could therefore be a transient event, and the localization of RCC1 should display hysteresis, i.e. it should persist even when the phosphorylating kinase (Cdk1) is inactive.

This model poses two questions that might provide interesting directions for future work. First, is the Ran-mediated dissociation of RCC1 from importin α3 an absolute requirement for maintaining RCC1 chromatin localization or does the equilibrium between importin- and chromatin-binding favour the chromatin-bound state of RCC1 even in the absence of Ran-mediated feedback? The K_D of the RCC1 nucleosome interaction has been estimated to 5 nM and the K_D for the importin α/β-NLS interaction is on the order of 30 nM [103, 134]. Both interactions are of similar affinity, therefore the equilibrium distribution between importin- and chromatin-bound RCC1 depends on the relative concentrations of importin α3 and chromosomal binding sites. The question is, whether there is enough importin α3 to sequester RCC1 to such a degree that the Ran gradient could be affected in a situation where the Ran-mediated feedback is not active? Second, what is the time-course of phosphorylation? Cdk1 is activated prior to mitosis and translocates to the nucleus before nuclear envelope breakdown [90]. It is inactivated at anaphase by proteasomal degradation of its cyclin B partner. Does RCC1 phosphorylation follow Cdk1 activity over time and what is the phosphatase that determines the steady-state level of phosphorylation?

5.4 The interaction of RCC1 with chromatin and Ran is regulated during mitosis

The mobility of RCC1 on chromatin differs between interphase and mitosis. Specifically, the dissociation rate constant of the immobilized state is decreased from $4.58 \pm 0.94\,\mathrm{s}^{-1}$ in interphase to $2.43 \pm 1.44\,\mathrm{s}^{-1}$ in mitosis (table 4.3 on page 45). The decrease in the dissociation rate constant is not accompanied by a significant decrease in the mobile fraction. This indicates that the association rate between RCC1 and nucleosomes is also regulated during mitosis, and that both the transition frequencies to and from the immobilized state are reduced. Judging from the apparent diffusion constant, there is also no change in the unbound fraction, i.e. the overall level of chromatin-association is unchanged

between interphase and mitosis.

How this change in the dynamic properties of the immobilized state is regulated on a molecular level remains an interesting question. One possibility is that this regulation is mediated by a conformational change in the RCC1 structure, which could for example be induced by cell-cycle dependent post-translational modification. Previous work suggested that a conformational change occurs in RCC1 upon chromatin or Ran binding [135]. This change was detected by fluorescence resonance energy transfer (FRET) between N- and C-terminally attached fluorescent proteins, and was interpreted as a conformational change in the N-terminal tail. Interestingly, a change in the level of FRET was detected during mitosis, indicating a conformational regulation during mitosis. However, my FCS data argue against an involvement of the first 27 amino acid residues in the regulatory mechanism, because similar changes in chromatin-binding dynamics are observed for wildtype RCC1 as well as RCC1Δ27 and RCC1 S2,11A during mitosis. Conformational changes might still involve the β-propeller structure of RCC1 though. Superimposing the structures of the monomeric and the Ran-bound human RCC1 with the nucleosome-bound drosophila RCC1 does not reveal striking differences in the conformation of the β-propeller (data not shown) [5, 91, 100]. However, this does not rule out conformational changes during mitosis because no crystallographic data is currently available on RCC1 with possible mitosis-specific modifications.

As an alternative to modifications of RCC1 itself, chromatin binding might also be regulated on the level of chromatin structure. There are two possibilities for how this can take place. First, global changes in chromatin structure such as different degrees of chromatin condensation in heterochromatin or during cell division might affect chromatin-binding of RCC1. Second, specific modifications of nucleosomes might regulate the RCC1-nucleosome interaction. The latter model has the appeal that it offers the possibility to spatially regulate the RCC1-chromatin interaction by the modification of a local subset of nucleosomes. On example for a mechanism that is based on a specific nucleosome modification is the apoptosis-specific phosphorylation of serine 14 of histone H2B, which causes a decrease in RCC1's mobility [109]. Interestingly, this particular serine residue is part of the N-terminal tail of H2B, which appears not to be in close contact with RCC1 [100]. Phosphorylation of H2B might therefore have an indirect effect on RCC1 binding by altering the nucleosome conformation or higher order chromatin structure.

In the context of RCC1's role in apoptosis, it was suggested that a decrease in RCC1's mobility correlates with a decrease in RCC1's catalytic efficiency [109]. This begs the question how the observed change in the stability of

the immobilized state of RCC1 affects its interaction with Ran during mitosis. Analysis of the autocorrelation data does not reveal any difference in the mobility of wildtype Ran during mitosis (table 4.5 on page 54). However, differences might be hidden by the fact that the slow autocorrelation component cannot be analyzed reliably by curve fitting due to its minor contribution to the total amplitude. Interestingly, in the case of RanT24N the dissociation rate constant of the immobilized state is decreased from $5.31 \pm 1.39\,\mathrm{s}^{-1}$ in interphase to $0.97 \pm 0.58\,\mathrm{s}^{-1}$ in mitosis (table 4.6 on page 56). Similarly, a decrease in the mobility of the RanT24N-RCC1 complex is observed, with k_{off} decreasing from $3.51 \pm 1.36\,\mathrm{s}^{-1}$ to $0.63 \pm 0.41\,\mathrm{s}^{-1}$ (table 4.7 on page 61). If it is true that the residence time of Ran on chromatin is an indicator for the Ran-RCC1 interaction, this means that the dissociation rate of the binary complex of RanT24N and RCC1 is decreased during mitosis. This is correlated with a decrease in the interaction strength between RanT24N and RCC1 during mitosis, implying a decrease in the association rate of the complex as well (figure 4.13 on page 59). Both effects, the decrease in the interaction strength, i.e. in the steady state concentration of the binary complex, as well as a decrease in the nucleotide dissociation rate will decrease the turnover rate of the nucleotide exchange reaction. This interpretation of the FCS data agrees with the model that a decrease in the mobility of RCC1 is linked with a decrease in its catalytic efficiency.

5.5 Implications for spindle assembly

It has been speculated previously that a switch-like accumulation of RCC1 takes place at the onset of mitosis, which is driven by a Ran-mediated feedback and phosphorylation by Cdk1 [78]. This hypothesis was motivated by the fact that importin-binding of RCC1 competes with its chromatin-binding, and that both active Ran and Cdk1-dependent N-terminal phosphorylation, which occurs during mitosis, inhibit binding to importins. Because reaction topologies involving a positive feedback (here, activation of Ran by chromsome-bound RCC1) can generate bistability in the state of its reactants, this might shift the RCC1 population from completely importin-bound to chromatin-bound. However, the FCS data presented here give no evidence for a change in the overall level of recruitment to chromatin between interphase and mitosis. Instead, I propose that regulation during mitosis affects the dynamic properties of the nucleosome-bound state of RCC1 and thereby reduces the turnover rate of the nucleotide exchange reaction. Cdk1-mediated phosphorylation does not affect chromatin-binding directly, but regulates binding to importins. As discussed

in section 5.3, this might be a safeguard mechanism to maintain chromosomal localization of RCC1. What then might be the functional significance of a regulation of the reaction rate of the nucleotide exchange reaction?

There is evidence that the spatial profile of the Ran gradient scales with the length of the mitotic spindle. For example the Ran gradient decays to the minimal Ran concentration after about 5 μm in mitotic HeLa cells, whereas it extends approximately 20 μm away from chromatin in *X. laevis* egg extracts [64]. In both cases this correlates with the significantly different size of the mitotic spindle. Cell-type specific modulation of the rate of Ran activation might be a mechanism to affect the extent of the Ran gradient [63]. Therefore it might be interesting to study the Ran and RCC1 dynamics on chromatin in different experimental systems such as somatic cells and *X. laevis* egg extracts.

Modulation of the GEF reaction might also be a very localized mechanism, restricted to certain regions of mitotic chromatin. For example, Ran might be regulated specifically at kinetochores to facilitate the formation of MT-kinetochore connections [136]. Because kinetochores are small compared to the size of a diffraction-limited observation volume, FCS measurements can only provide information about the average mobility of kinetochore- and non-kinetochore-bound RCC1 and Ran. Therefore, it cannot be concluded whether the mobility of Ran and RCC1 is decreased or increased on kinetochores relative to other regions of the chromatin. Interestingly, Ran recruits the exportin Crm1 to kinetochores, which in turn causes the kinetochore-localization of RanGAP and RanBP2. Recruitment of Crm1 indicates that active and immobile Ran should be enriched on chromatin. How this can be achieved by regulation of the Ran-RCC1 interaction is not intuitively clear on the basis of the model for the Ran-RCC1 interaction presented above. A modelling approach to characterize the dynamics of the Ran GTPase cycle taking into account the coupling between the GEF reaction and chromatin binding could be a good starting point for further investigations on Ran's role on kinetochores.

6 Methods

6.1 Molecular biology

Techniques and reagents

Basic methods of DNA handling and manipulation were as previously described [137].

DNA was separated and analyzed by electrophoresis in 1% agarose gels in TAE buffer (40 mM Tris/acetate, 1 mM EDTA, pH 8.5). DNA was purified from agarose gels using the QIAquick Gel Extraction kit (Qiagen, Hilden, Germany).

All PCR reactions were performed using high fidelity *PfuUltra* HF DNA polymerase (Stratagene, La Jolla, CA, USA) according to the manufacture's protocol. PCR products were purified using the QIAquick PCR Purification kit (Qiagen). Sequence-specific cleavage of DNA was carried out with restriction enzymes purchased from New England Biolabs (Ipswich, MA, USA). Cleaved vectors and DNA fragments were ligated using T4 DNA Ligase (New England Biolabs). Point mutations were introduced into DNA plasmids by *Dpn*I mediated site directed mutagenesis [138]. DNA oligonucleotides to be used as PCR primers were synthesized by MWG (Ebersberg, Germany) or Sigma-Aldrich (St. Louis, MO, USA). Oligonucleotides used for site directed mutagenesis were HPLC purified by the manufacturer.

Plasmids were propagated in the *E. coli* XL10-Gold strain (Agilent Technologies, Santa Clara, CA, USA) grown in LB medium supplemented with either 100 μg/ml ampicillin (SERVA electrophoresis, Heidelberg, Germany) or 50 μg/ml kanamycin (GERBU Biotechnik, Wieblingen, Germany) depending on the resistance gene of the plasmid.

Small amounts of plasmid DNA were purified from bacteria using the Qiaprep Spin Miniprep kit (Qiagen), large amounts of endotoxin-free plasmid DNA for transfection were purified using the NucleoBond Xtra EF kit (Macherey-Nagel, Düren, Germany). The identity of DNA plasmids was verfied by dideoxy sequencing [139] using the Big dye terminator v3.1 cycle sequencing kit (Applied Biosystems, Carlsbad, CA, USA) and a Abi Prism 3700 capillary sequencer (Applied Biosystems).

DNA constructs

The plasmids encoding RCC1-EGFP and RCC1-paGFP were constructed by inserting the coding sequence of the γ-isoform of human RCC1 (gift from J. Ellenberg, EMBL, [115]) into the *Xho*I and *Age*I restriction sites of pEGFP-N1 or paGFP-N1, (Clontech, Mountain View, CA, USA), thus creating a SP-VAT linker between RCC1 and the fluorescent protein. Plasmids encoding RCC1Δ27-EGFP and NT-GFP were made by producing partial RCC1 γ coding sequences by polymerase chain reaction and inserting them into pEGFP-N1 using the restriction sites above. All point mutations were introduced directly into RCC1-EGFP or NT-GFP. A plasmid encoding H2B-EGFP was constructed by inserting the coding sequence for human histone H2B from pH2B-diHcRed (gift from J. Ellenberg, EMBL, [140]) into the *Sal*I and *BamH*I sites of pEGFP-N1. Plasmids encoding for EGFP-Ran and mCherry-Ran were obtained by inserting the coding sequence for human Ran (gift from A. Wittinghofer, MPI Dortmund) into the *Hind*III and *BamH*I sites of pEGFP-C3 and pmCherry-C3 (Clontech, Mountain View, CA, USA), respectively. This creates a YSDLELKL linker sequence between the two proteins. The plasmid encoding mCherry-Tubulin (gift from L. Dehmelt, MPI Dortmund) contained the coding sequence of human α tubulin and was originally constructed by exchanging the EGFP coding sequence of pEGFP-Tub (Clontech, Mountain View, CA, USA) for the mCherry coding sequence. EGFP-p38-mCherry was a kind gift of M. Hink (MPI Dortmund). A plasmid encoding histone H1-EGFP was constructed by replacing the coding sequence of paGFP in the plasmid H1.1-paGFP (J. Ellenberg, EMBL, [115]) by the coding sequence of EGFP.

6.2 Mammalian cell culture

Cells from the HeLa human cervical cancer cell line were grown at 37°C and 5% CO_2 in DMEM (PAN-Biotech, Aidenbach, Germany) supplemented with 10% fetal calf serum (PAN-Biotech) and 2 mM L-glutamine (Gibco/Invitrogen, Darmstadt, Germany). The cells were grown in 10 cm tissue culture dishes (BD Falcon, Heidelberg, Germany). To prevent cells from growing to confluency, cells were split every two to three days by treatment with trypsin/EDTA (PAN-Biotech) and re-seeding into fresh medium at a dilution of 1:10. For long-term storage, cells were kept in DMEM supplemented with 20% fetal calf serum and 10% DMSO (SERVA Electrophoresis) at a concentration of 10^6 cells/ml at -196°C in liquid nitrogen. Cells were counted with a Vi-CELL XR cell viability analyzer (Beckman Coulter, Brea, CA, USA).

Two days prior to the experiments, cells were seeded on LabTek II cham-

bered No. 1 coverglass (Nalge Nunc International, Rochester, NY, USA) at a density of approximately $2 \cdot 10^5$ cells per single well LabTek chamber. Immediatly after seeding, cells were transfected with DNA plasmids using FuGENE 6 (Roche, Mannheim, Germany) according to the manufacturer's instructions. For a single well LabTek chamber, transfection was performed with a total DNA amount of 1 μg and 3 μl transfection reagent. To reduce the expression level of the ectopically expressed proteins for FCS experiments, DNA used for transfection was mixed with non-coding pcDNA 3.1 plasmid (Invitrogen, Darmstadt, Germany) at a ratio of 1:4, while keeping the total amount of DNA constant.

For microscopy, cells were kept in phenolred-free DMEM supplemented with 25 mM Hepes (PAN-Biotech), 10% fetal calf serum, and 2 mM L-glutamine.

6.3 Fluorescence correlation spectroscopy

Experimental setup

Fluorescence correlation spectroscopy (FCS) was performed on a Zeiss LSM 510 Meta confocal microscope (Carl Zeiss Jena, Jena, Germany) equipped with a ConfoCor 3 unit and a C-Apochromat 40x/1.2 NA W Corr water-immersion objective. During measurements, the sample and the objective were kept at the desired temperature using an incubation box. If not noted otherwise, measurements were carried out at 37°C.

For single-colour autocorrelation measurements, the sample was excited with the 488 nm line of an argon laser through a HFT 405/488/561 beam splitter. The emitted fluorescence was collected through a LP 505 long pass filter, and was detected in confocal mode with a 70 μm pinhole using an avalanche photodiode (APD) detector. In dual-colour crosscorrelation measurements, the sample was simultaneously excited with the 488 nm line of an argon laser and the 561 nm line of a DPSS laser through a HFT 405/488/561 beam splitter. The emitted fluorescence was separated through a NFT 565 beam splitter onto two APD detectors equipped with a BP 505-540 IR (EGFP channel) and a BP 615-680 IR (mCherry channel) band pass filter, respectively (see figure 6.1 for spectral characteristics of EGFP and mCherry). The pinhole diameter was set to 72 μm.

Calibration measurements were performed on aqueous solutions of Alexa Fluor 488 or Alexa Fluor 546 (Molecular Probes, Eugene, OR, USA) on LabTek II chambered No. 1 coverglass to determine the geometrical parameters of the observation volume in the EGFP and mCherry channel, respectively. At the beginning of each day of experimentation, the objective correction ring and the

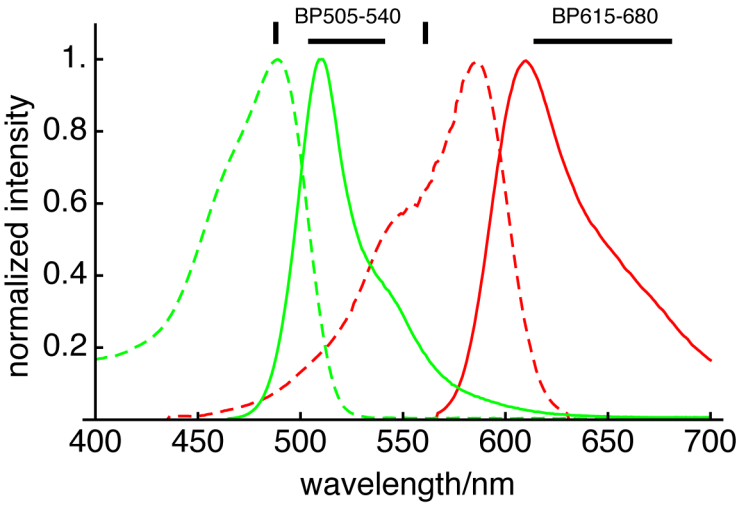

Figure 6.1: Excitation (dashed lines) and emission spectra (solid lines) of EGFP (green) and mCherry (red). The excitation wavelengths at 488 nm and 561 nm are indicated with vertical black bars, the detection range of the band pass filters used for FCCS is indicated with horizontal lines.

lateral pinhole position were optimized to yield the maximal count rate from Alexa Fluor 488 excited with 488 nm. After this optimization, the excitation power was attenuated to give an average molecular brightness of 15 kHz for Alexa Fluor 488 and 11 kHz for Alexa Fluor 546 to record the calibration autocorrelation curves.

For live cell measurements of EGFP and mCherry, the excitation power was attenuated to give an average molecular brightness of 1 kHz for EGFP and 0.4 kHz for mCherry. Cells were selected for the expression level of EGFP- and mCherry-tagged proteins base on the averaged count rate measured at the point of interest. FCS measurements were taken over an average count rate range of 10 kHz to 200 kHz.

The raw intensity data was auto- and crosscorrelated using the microscope manufacturer's software. Typically, the correlation curves of two to five consecutive 20 sec intensity recordings were averaged for one measurement, except for calibration measurements where ten consecutive 10 sec recordings were averaged. Individual correlation curves were discarded when strong drift or bleaching was apparent in the intensity trace.

Table 6.1: Analysis of FCS data by curve fitting. Starting values, and upper limits for each model parameter that was optimized by non-linear least-squares minimization. The starting value for N, N_{guessed}, was estimated by calculating the average correlation value between $1\,\mu$s and $10\,\mu$s ant taking the inverse. The lower limit for each parameter was 0.

Model	Parameter	Start	Upper
General	N	N_{guessed}	∞
	S	4	20
Diffusion	$D/\mu\text{m}^2\,\text{s}^{-1}$	10	∞
	τ_D/μs	100	∞
Binding diffusion	$k_{\text{off}}/\text{s}^{-1}$	10	∞
	F	1	1
Triplett blinking	τ_T/μs	1	∞
	F_T	1	1

Curve fitting

Fitting of model equations to the correlation curves was performed using non-linear least-squares minimization of the unweighted sum of the squared fit residuals. The fitting procedure was implemented in Matlab 7 R2010b (The MathWorks, Natick, MA, USA) on the basis of the `lsqnonlin` function of the Matlab optimization toolbox. Parameter-specific starting values and upper limits are given in table 6.1.

Correlation curves of fluorescent proteins recorded in living cells were fit only for correlation times above $10\,\mu$s. On this time scale, fluorophore blinking effects could be neglected and were not accounted for in the fitting models. Autocorrelation curves were fit either with an equation for binding and diffusion (eq. 3.19 on page 30) or for diffusion only (eq. 2.3 on page 23). Numerical integration of eq. 3.19 was implemented using the `dblquad` function of Matlab 7 R2010b.

The geometrical parameters S and r_0 of the focal volume were determined from calibration measurements of Alexa Fluor 488 and Alexa Fluor 546, assuming diffusion constants of $536\,\mu\text{m}^2\,\text{s}^{-1}$ and $308\,\mu\text{m}^2\,\text{s}^{-1}$ at 37°C, respectively [141]. Calibration curves were fit for correlation times above $1\,\mu$s with a model accounting for three-dimensional diffusion and fluorophore blinking (eq. 2.5 on page 23). For the experimental setup described above this yielded $r_0 = 202 \pm 4\,\text{nm}$ and $S = 5.4 \pm 0.5$ for Alexa Fluor 488, and $r_0 = 196 \pm 4\,\text{nm}$ and $S = 5.0 \pm 0.4$ for Alexa Fluor 546.

Calculation of the apparent interaction strength

To calculate the apparent interaction strength in FCCS experiments, auto- and crosscorrelation amplitudes were estimated by calculating the average correlation value between 1 μs and 100 μs. In a dual-colour FCCS experiment, the correlation amplitudes are related to the total concentration of each labelled species and to the concentration of their complex (see section 2.3.2). Assuming that the two species A and B form a complex with 1:1 stoichiometry, the following expression for the dissociation constant of the interaction can be derived:

$$K_D = \frac{G_X}{V_{\text{eff}}\, G_A\, G_B} \left(\frac{G_A}{G_X} - 1\right) \left(\frac{G_B}{G_X} - 1\right) \tag{6.1}$$

Here, G_X is the crosscorrelation amplitude and G_A and G_B are the autocorrelation amplitudes of the two species A and B, respectively. V_{eff} is the effective overlap of the two observation volumes.

The calculation of a K_D for protein-protein interactions is complicated by two characteristic features of live cell measurements. First, the interaction takes place in the presence of a potentially large number of competing interactors. Second, in addition to the labelled proteins, which are encoded by the DNA plasmid used for transfection, there is an unknown fraction of unlabelled proteins expressed from their genomic location, which participate in the binding equilibrium. It is therefore not possible to calculate an absolute K_D for the binary interaction of A and B. Hence, crosscorrelation experiments were quantified by calculating a dimensionless *apparent interaction strength* to compare the extent of interaction in different samples. This also allowed to neglect the effect of an impartial overlap of the two observation volumes, which should be the same in all samples. The apparent interaction strength was calculated as the inverse of the K_D, with $V_{\text{eff}} = 1$. As described in section 4.3.2 on page 56, the apparent interaction strength was normalized between the highest and lowest mean values observed.

6.4 Confocal microscopy

Confocal microscopy was performed on the same instrument as FCS (see above). For single-colour imaging of EGFP, the sample was excited with the 488 nm line of an argon laser through a HFT 405/488/561 dichroic mirror. The emitted fluorescence was imaged through a LP 505 long-pass filter onto a photomultiplier tube (PMT) detector. For dual-colour imaging of EGFP and mCherry, the sample was excited by bidirectional scanning, alternating

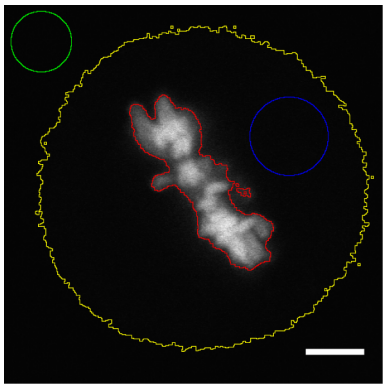

Figure 6.2: Example of quantitative image analysis of a HeLa cell expressing RCC1-EGFP. The cell border is outlined in yellow. The mean fluorescence intensity on chromatin, in the cytoplasm, and in the background was calculated from the pixels in the red, blue, and green region on interest, respectively. Scale bar: 5 μm.

line by line between the 488 nm argon laser line (EGFP) and a 561 nm DPSS laser (mCherry) to minimize the cross-detection of EGFP fluorescence in the mCherry channel. The same dichroic mirror as above was used. The emitted fluorescence was separated by a NFT 565 beam splitter and imaged onto separate PMT detectors either through a BP 505-500 band pass filter (EGFP) or a LP 575 long pass filter (mCherry). Unless otherwise noted, single confocal slices were recorded at a size of 512-by-512 pixels and a pixel distance of 0.088 μm. The pinhole was set to a diameter of 170 μm. Images were stored and processed in the LSM file format with 8 or 12 bit per channel.

Quantitative imaging of RCC1 localization in mitotic cells

To calculate the fraction of unbound molecules in mitotic cells, mean fluorescence intensities were measured in a cytoplasmic region and in a region occupied by chromatin in images of mitotic cells (figure 6.2 shows a representative image analysis). The mean fluorescence intensities were corrected by subtracting the mean background intensity measured in a region outside of the cell. The fraction of unbound molecules was calculated as $F = I_{\text{cytoplasm}}/I_{\text{chromatin}}$, where $I_{\text{cytoplasm}}$ and $I_{\text{chromatin}}$ were the corrected mean fluorescence intensities in the cytoplasm and on the chromatin, respectively.

Imaging of RCC1 localization after nocodazole treatment

HeLa cells coexpressing RCC1-EGFP and mCherry-Tubulin were treated with the indicated concentration of nocodazole (Sigma-Aldrich, St. Louis, MO, USA). Immediately after nocodazole addition a time-lapse recording was started by taking dual-colour images every minute. Images were taken using an autofocus and tracking macro as previously described [142]. Shortly, this involved rapidly taking a z-stack of 10 images at a reduced size of 16-by-16 pixels and a z-interval of 1 μm and resetting the focus to the centre of mass of the fluorescence intensity distribution of this image stack. Autofocussing was performed on images taken in the mCherry channel. The unbound fraction of RCC1 was determined as described above.

Photoactivation of paGFP

For photoactivation experiments, mitotic HeLa cells cotransfected with RCC1-paGFP and histone H2B-diHcRed were identified by diHcRed fluorescence. Single mitotic cells were imaged by recording single confocal slices at a size of 256-by-256 pixels and a resolution of 0.18 μm per pixel. A total of 200 frames were recorded at a frame rate of 2 Hz. After the fifth frame, paGFP was photoactivated by scanning the beam of a 405 nm laser diode with maximal excitation intensity across the chromatin. The time-lapse series was analysed by measuring the average EGFP intensity in a circular area of the cytoplasm.

6.5 Statistical analysis

Mean difference test

Datasets of fitting parameters were compared using a two-sample two-sided mean difference test based on the Student's t-distribution as implemented in the `TTest` function of Mathematica 8 (Wolfram Research, Champaign, IL, USA). This tests the null hypothesis that the means of the two datasets are equal. The test results are reported as the probability (p-value) of obtaining the observed mean difference if the true mean difference was zero. Hence, a low p-value indicates that the null hypothesis is unlikely to be true and that the observed mean difference the two datasets is significant. By convention, a p-value < 0.01 is be considered statistically significant in this work.

F test

Given two models with different numbers of parameters ($p_1 < p_2$), the F statistic was calculated as follows:

$$F = \left(\frac{\mathrm{RSS}_1 - \mathrm{RSS}_2}{p_2 - p_1}\right) \Big/ \left(\frac{\mathrm{RSS}_2}{n - p_2}\right) \tag{6.2}$$

where n is the number of data points the models were fit to and RSS_i is the residual sum of squares from model i. The F-test tests the null hypothesis that model 2 does not provide a significantly better fit than model 1. Under this hypothesis, F will have a F distribution with $(p_2 - p_1, n - p_2)$ degrees of freedom. The p-value is calculated by comparing the observed F statistic to a F distribution with $(p_2 - p_1, n - p_2)$ degrees of freedom, and gives the probability of obtaining a F statistic at least as big as the one observed when the null hypothesis is true.

Average p-values from a group of F-tests were calculated with the assumption that p-values are log-normally distributed:

$$\bar{p} = \exp\left(\mu(\log p) + \sigma^2(\log p)\right) \tag{6.3}$$

where $\bar{p}$ is the mean p-value and $\mu(\log p)$ and $\sigma^2(\log p)$ are the mean and variance of natural logarithm of all p-values.

Summary

A spatial activity gradient of the small G-protein Ran is an important mechanism of controlling essential cellular processes such as nucleo-cytoplasmic transport, mitotic spindle assembly, and formation of the nuclear envelope. Formation of this gradient depends on the spatial partitioning of the opposing enzyme activities of the Ran guanine exchange factor, Regulator of Chromosome Condensation (RCC1), and Ran GTPase activating protein (RanGAP). This partitioning is achieved by interaction of RCC1 with chromatin. Binding to chromatin not only partitions RCC1 to chromatin but might also couple the reaction between RCC1 and Ran to chromatin. Regulation of RCC1's chromatin affinity might therefore be a way to regulate the production of Ran at different stages of the cell cycle.

To test this hypothesis, the interaction kinetics between RCC1 and chromatin are studied. Measurements of RCC1 mobility in living cells by fluorescence correlation spectroscopy (FCS) are analyzed to determine the mechanism of chromatin interaction. By comparing the distribution of RCC1 between chromatin and the cytoplasm and the mobility measured by FCS, it is demonstrated that chromatin-bound RCC1 can have two mobility states. In one state, RCC1 is loosely bound to chromatin and can undergo one-dimensional diffusion along the chromatin fibre. In the second state, RCC1 is transiently immobilized by interaction with specific sites. The quantitative analysis of FCS data allows to determine the diffusion constant of the loosely bound state and the dissociation rate constant of the immobilized state.

Measurements of the mobility of Ran indicate a correlation between the interaction kinetics between Ran and chromatin and the reaction kinetics between Ran and RCC1. Furthermore, measuring the interaction between Ran and RCC1 by fluorescence crosscorrelation spectroscopy (FCCS) supports the hypothesis that the reaction between both proteins is coupled to chromatin, and that the binary complex of Ran and RCC1, an important intermediate of the reaction, is bound to chromatin.

By comparing RCC1 mobility between interphase and cell division, a cell cycle dependent regulation of chromatin binding can be demonstrated. This regulation results in a decreased dissociation rate constant of the immobilized state of RCC1. In addition, a decrease in the interaction between Ran and RCC1 can be detected during cell division. In conclusion, the hypothesis is

formulated that by regulating the kinetic properties of the immobilized state of RCC1 the rate of Ran activation by RCC1 is reduced during cell division.

Zusammenfassung

Ein räumlicher Aktivitätsgradient des kleinen G-Proteins Ran ist ein bedeutender Kontrollmechanismus von grundlegenden zellulären Prozessen wie dem Transport zwischen Kern und Cytoplasma, dem Aufbau des mitotischen Spindelapparats und der Bildung der Kernhülle. Die Entstehung dieses Gradienten verlangt eine räumliche Trennung der entgegenwirkenden enzymatischen Aktiviäten des Ran-spezifischen Guaninnukleotid-Austauschfaktors RCC1 und des Ran-spezifischen GTPase aktivierenden Proteins RanGAP. Die Interaktion von RCC1 mit Chromatin ist eine Vorraussetzung hierfür, indem sie RCC1 von dem sich im Cytoplasma befindlichen RanGAP trennt. Darüber hinaus beeinflusst die Chromatininteraktion möglicherweise die enzymatische Aktivität von RCC1 und bewirkt eine räumliche Kopplung der Reaktion zwischen Ran und RCC1 an Chromatin. Die Regulation der Chromatininteraktion von RCC1 ist deswegen ein potentieller Mechanismus, die Aktivierung von Ran in Abhängigkeit des Zellzyklus zu regulieren.

Um diese Hypothese zu überprüfen, wird in der vorliegenden Arbeit eine Untersuchung der kinetischen Eigenschaften der Chromatininteraktion von RCC1 durchgeführt. Die Messung der Mobilität von RCC1 auf molekularer Ebene durch Fluoreszenzkorrelationsspektroskopie (FCS) erlaubt Rückschlüsse auf den Mechanismus der Chromatininteraktion. Ein Vergleich der Verteilung von RCC1 zwischen Chromatin und Zytoplasma und der durch FCS gemessen Mobilität zeigt, dass an Chromatin gebundenes RCC1 zwei verschiedene Mobilitätszustände einnehmen kann. Es kann unterschieden werden zwischen RCC1, das in einem eindimensionalen Prozess entlang der Chromatinfaser diffundiert, und RCC1, das für einen kurzen Zeitraum an spezifischen Stellen gebunden ist. Die quantitative Analyse der FCS-Messungen ermöglicht eine Bestimmung der Diffusionkonstante des mobilen Zustands sowie der Dissoziationsrate des gebundenen Zustands.

Durch Messung der Mobilität von Ran wird gezeigt, dass die Interaktionskinetik zwischen Ran und Chromatin mit der Reaktionskinetik zwischen Ran und RCC1 korreliert. Weiterhin stärken Messungen der Interaktion von Ran und RCC1 mittels Fluoreszenzkreuzkorrelationsspektroskopie (FCCS) die Hypothese, dass die Reaktion zwischen beiden Proteinen an Chromatin gekoppelt ist. Insbesondere weisen die hier vorgestellten Ergebnisse darauf hin, dass der binäre Komplex zwischen Ran und RCC1, ein wichtiges enzymatisches Inter-

mediat, an Chromatin gebunden ist.

Der Vergleich zwischen Mobilitätsmessungen während der Interphase und während der Zellteilung demonstriert eine zellzyklusabhängige Regulation der Chromatininteraktion von RCC1. Diese äußert sich in einer verringerten Dissoziationsrate des fest gebundenden Zustands von RCC1. Des Weiteren kann während der Zellteilung eine verringerte Interaktion zwischen RCC1 und Ran gemessen werden. Hieraus wird abschließend die Hypothese abgeleitet, dass durch eine Regulation der Bindungseigenschaften des fest gebundenen Zustands von RCC1 eine Verringerung der Reaktionsrate zwischen Ran und RCC1 erreicht wird.

Bibliography

[1] I. R. Vetter and A. Wittinghofer (2001). The guanine nucleotide-binding switch in three dimensions. *Science*, **294**, 1299–304.

[2] Y. Takai, T. Sasaki, and T. Matozaki (2001). Small GTP-binding proteins. *Physiol Rev*, **81**, 153–208.

[3] F. R. Bischoff and H. Ponstingl (1991). Catalysis of guanine nucleotide exchange on Ran by the mitotic regulator RCC1. *Nature*, **354**, 80–2.

[4] F. R. Bischoff, C. Klebe, J. Kretschmer, A. Wittinghofer, and H. Ponstingl (1994). RanGAP1 induces GTPase activity of nuclear Ras-related Ran. *Proc Natl Acad Sci U S A*, **91**, 2587–2591.

[5] L. Renault, J. Kuhlmann, A. Henkel, and A. Wittinghofer (2001). Structural basis for guanine nucleotide exchange on Ran by the regulator of chromosome condensation (RCC1). *Cell*, **105**, 245–55.

[6] M. J. Seewald, C. Körner, A. Wittinghofer, and I. R. Vetter (2002). RanGAP mediates GTP hydrolysis without an arginine finger. *Nature*, **415**, 662–6.

[7] C. Klebe, F. R. Bischoff, H. Ponstingl, and A. Wittinghofer (1995). Interaction of the nuclear GTP-binding protein Ran with its regulatory proteins RCC1 and RanGAP1. *Biochemistry*, **34**, 639–47.

[8] F. R. Bischoff, H. Krebber, E. Smirnova, W. Dong, and H. Ponstingl (1995). Co-activation of RanGTPase and inhibition of GTP dissociation by Ran-GTP binding protein RanBP1. *EMBO J*, **14**, 705–15.

[9] I. R. Vetter, C. Nowak, T. Nishimoto, J. Kuhlmann, and A. Wittinghofer (1999). Structure of a Ran-binding domain complexed with Ran bound to a GTP analogue: implications for nuclear transport. *Nature*, **398**, 39–46.

[10] M. J. Matunis, J. Wu, and G. Blobel (1998). SUMO-1 modification and its role in targeting the Ran GTPase-activating protein, RanGAP1, to the nuclear pore complex. *J Cell Biol*, **140**, 499–509.

[11] J. Joseph, S.-H. Tan, T. S. Karpova, J. G. McNally, and M. Dasso (2002). SUMO-1 targets RanGAP1 to kinetochores and mitotic spindles. *J Cell Biol*, **156**, 595–602.

[12] M. Ohtsubo, H. Okazaki, and T. Nishimoto (1989). The RCC1 protein, a regulator for the onset of chromosome condensation locates in the nucleus and binds to DNA. *J Cell Biol*, **109**, 1389–97.

[13] H. Fried and U. Kutay (2003). Nucleocytoplasmic transport: taking an inventory. *Cell Mol Life Sci*, **60**, 1659–88.

[14] M. Stewart (2007). Molecular mechanism of the nuclear protein import cycle. *Nat Rev Mol Cell Biol*, **8**, 195–208.

[15] C. Strambio-De-Castillia, M. Niepel, and M. P. Rout (2010). The nuclear pore complex: bridging nuclear transport and gene regulation. *Nat Rev Mol Cell Biol*, **11**, 490–501.

[16] J. E. Hinshaw, B. O. Carragher, and R. A. Milligan (1992). Architecture and design of the nuclear pore complex. *Cell*, **69**, 1133–41.

[17] M. W. Goldberg and T. D. Allen (1992). High resolution scanning electron microscopy of the nuclear envelope: demonstration of a new, regular, fibrous lattice attached to the baskets of the nucleoplasmic face of the nuclear pores. *J Cell Biol*, **119**, 1429–40.

[18] C. W. Akey and M. Radermacher (1993). Architecture of the Xenopus nuclear pore complex revealed by three-dimensional cryo-electron microscopy. *J Cell Biol*, **122**, 1–19.

[19] M. P. Rout, J. D. Aitchison, A. Suprapto, K. Hjertaas, Y. Zhao, and B. T. Chait (2000). The yeast nuclear pore complex: composition, architecture, and transport mechanism. *J Cell Biol*, **148**, 635–51.

[20] J. M. Cronshaw, A. N. Krutchinsky, W. Zhang, B. T. Chait, and M. J. Matunis (2002). Proteomic analysis of the mammalian nuclear pore complex. *J Cell Biol*, **158**, 915–27.

[21] F. Alber, S. Dokudovskaya, L. M. Veenhoff, W. Zhang, J. Kipper, D. Devos, A. Suprapto, O. Karni-Schmidt, R. Williams, B. T. Chait, A. Sali, and M. P. Rout (2007). The molecular architecture of the nuclear pore complex. *Nature*, **450**, 695–701.

[22] D. P. Denning, S. S. Patel, V. Uversky, A. L. Fink, and M. Rexach (2003). Disorder in the nuclear pore complex: the FG repeat regions of nucleoporins are natively unfolded. *Proc Natl Acad Sci U S A*, **100**, 2450–5.

[23] S. Frey and D. Görlich (2007). A saturated FG-repeat hydrogel can reproduce the permeability properties of nuclear pore complexes. *Cell*, **130**, 512–523.

[24] T. Jovanovic-Talisman, J. Tetenbaum-Novatt, A. S. McKenney, A. Zilman, R. Peters, M. P. Rout, and B. T. Chait (2009). Artificial nanopores that mimic the transport selectivity of the nuclear pore complex. *Nature*, **457**, 1023–7.

[25] R. Y. H. Lim, N.-P. Huang, J. Köser, J. Deng, K. H. A. Lau, K. Schwarz-Herion, B. Fahrenkrog, and U. Aebi (2006). Flexible phenylalanine-glycine nucleoporins as entropic barriers to nucleocytoplasmic transport. *Proc Natl Acad Sci U S A*, **103**, 9512–7.

[26] K. Ribbeck and D. Görlich (2002). The permeability barrier of nuclear pore complexes appears to operate via hydrophobic exclusion. *EMBO J*, **21**, 2664–71.

[27] O. Keminer and R. Peters (1999). Permeability of single nuclear pores. *Biophys J*, **77**, 217–28.

[28] P. L. Paine, L. C. Moore, and S. B. Horowitz (1975). Nuclear envelope permeability. *Nature*, **254**, 109–114.

[29] W. M. Bonner (1975). Protein migration into nuclei. I. Frog oocyte nuclei in vivo accumulate microinjected histones, allow entry to small proteins, and exclude large proteins. *J Cell Biol*, **64**, 421–30.

[30] C. M. Feldherr, E. Kallenbach, and N. Schultz (1984). Movement of a karyophilic protein through the nuclear pores of oocytes. *J Cell Biol*, **99**, 2216–22.

[31] R. Bayliss, K. Ribbeck, D. Akin, H. M. Kent, C. M. Feldherr, D. Görlich, and M. Stewart (1999). Interaction between NTF2 and xFxFG-containing nucleoporins is required to mediate nuclear import of RanGDP. *J Mol Biol*, **293**, 579–93.

[32] L. A. Strawn, T. Shen, N. Shulga, D. S. Goldfarb, and S. R. Wente (2004). Minimal nuclear pore complexes define FG repeat domains essential for transport. *Nat Cell Biol*, **6**, 197–206.

[33] W. Yang, J. Gelles, and S. M. Musser (2004). Imaging of single-molecule translocation through nuclear pore complexes. *Proc Natl Acad Sci U S A*, **101**, 12887–92.

[34] D. Görlich, S. Prehn, R. A. Laskey, and E. Hartmann (1994). Isolation of a protein that is essential for the first step of nuclear protein import. *Cell*, **79**, 767–78.

[35] D. Kalderon, W. D. Richardson, A. F. Markham, and A. E. Smith (1984). Sequence requirements for nuclear location of simian virus 40 large-T antigen. *Nature*, **311**, 33–8.

[36] J. Robbins, S. M. Dilworth, R. A. Laskey, and C. Dingwall (1991). Two interdependent basic domains in nucleoplasmin nuclear targeting sequence: identification of a class of bipartite nuclear targeting sequence. *Cell*, **64**, 615–23.

[37] D. Görlich, F. Vogel, A. D. Mills, E. Hartmann, and R. A. Laskey (1995). Distinct functions for the two importin subunits in nuclear protein import. *Nature*, **377**, 246–8.

[38] D. S. Goldfarb, A. H. Corbett, D. A. Mason, M. T. Harreman, and S. A. Adam (2004). Importin alpha: a multipurpose nuclear-transport receptor. *Trends Cell Biol*, **14**, 505–14.

[39] D. Görlich, N. Panté, U. Kutay, U. Aebi, and F. R. Bischoff (1996). Identification of different roles for RanGDP and RanGTP in nuclear protein import. *EMBO J*, **15**, 5584–94.

[40] M. Rexach and G. Blobel (1995). Protein import into nuclei: association and dissociation reactions involving transport substrate, transport factors, and nucleoporins. *Cell*, **83**, 683–92.

[41] F. R. Bischoff and D. Görlich (1997). RanBP1 is crucial for the release of RanGTP from importin beta-related nuclear transport factors. *FEBS Lett*, **419**, 249–54.

[42] M. Fornerod, M. Ohno, M. Yoshida, and I. W. Mattaj (1997). CRM1 is an export receptor for leucine-rich nuclear export signals. *Cell*, **90**, 1051–60.

[43] R. H. Kehlenbach, A. Dickmanns, A. Kehlenbach, T. Guan, and L. Gerace (1999). A role for RanBP1 in the release of CRM1 from the nuclear pore complex in a terminal step of nuclear export. *J Cell Biol*, **145**, 645–57.

[44] A. Smith, A. Brownawell, and I. G. Macara (1998). Nuclear import of Ran is mediated by the transport factor NTF2. *Curr Biol*, **8**, 1403–6.

[45] K. Ribbeck, G. Lipowsky, H. M. Kent, M. Stewart, and D. Görlich (1998). NTF2 mediates nuclear import of Ran. *EMBO J*, **17**, 6587–98.

[46] D. A. Compton (2000). Spindle assembly in animal cells. *Annu Rev Biochem*, **69**, 95–114.

[47] T. Wittmann, A. Hyman, and A. Desai (2001). The spindle: a dynamic assembly of microtubules and motors. *Nat Cell Biol*, **3**, E28–34.

[48] E. Karsenti and I. Vernos (2001). The mitotic spindle: a self-made machine. *Science*, **294**, 543–7.

[49] T. Mitchison and M. Kirschner (1984). Dynamic instability of microtubule growth. *Nature*, **312**, 237–42.

[50] M. Kirschner and T. Mitchison (1986). Beyond self-assembly: from microtubules to morphogenesis. *Cell*, **45**, 329–42.

[51] R. Heald, R. Tournebize, T. Blank, R. Sandaltzopoulos, P. Becker, A. Hyman, and E. Karsenti (1996). Self-organization of microtubules into bipolar spindles around artificial chromosomes in Xenopus egg extracts. *Nature*, **382**, 420–5.

[52] J. Lüders, U. K. Patel, and T. Stearns (2006). GCP-WD is a gamma-tubulin targeting factor required for centrosomal and chromatin-mediated microtubule nucleation. *Nat Cell Biol*, **8**, 137–47.

[53] A. Khodjakov, L. Copenagle, M. B. Gordon, D. A. Compton, and T. M. Kapoor (2003). Minus-end capture of preformed kinetochore fibers contributes to spindle morphogenesis. *J Cell Biol*, **160**, 671–83.

[54] H. Maiato, C. L. Rieder, and A. Khodjakov (2004). Kinetochore-driven formation of kinetochore fibers contributes to spindle assembly during animal mitosis. *J Cell Biol*, **167**, 831–40.

[55] R. E. Carazo-Salas and E. Karsenti (2003). Long-range communication between chromatin and microtubules in Xenopus egg extracts. *Curr Biol*, **13**, 1728–33.

[56] P. Kalab, R. T. Pu, and M. Dasso (1999). The ran GTPase regulates mitotic spindle assembly. *Curr Biol*, **9**, 481–4.

[57] T. Ohba, M. Nakamura, H. Nishitani, and T. Nishimoto (1999). Self-organization of microtubule asters induced in Xenopus egg extracts by GTP-bound Ran. *Science*, **284**, 1356–8.

[58] A. Wilde and Y. Zheng (1999). Stimulation of microtubule aster formation and spindle assembly by the small GTPase Ran. *Science*, **284**, 1359–62.

[59] R. E. Carazo-Salas, G. Guarguaglini, O. J. Gruss, A. Segref, E. Karsenti, and I. W. Mattaj (1999). Generation of GTP-bound Ran by RCC1 is required for chromatin-induced mitotic spindle formation. *Nature*, **400**, 178–81.

[60] A. Wilde, S. B. Lizarraga, L. Zhang, C. Wiese, N. R. Gliksman, C. E. Walczak, and Y. Zheng (2001). Ran stimulates spindle assembly by altering microtubule dynamics and the balance of motor activities. *Nat Cell Biol*, **3**, 221–7.

[61] R. E. Carazo-Salas, O. J. Gruss, I. W. Mattaj, and E. Karsenti (2001). Ran-GTP coordinates regulation of microtubule nucleation and dynamics during mitotic-spindle assembly. *Nat Cell Biol*, **3**, 228–34.

[62] P. Kaláb, K. Weis, and R. Heald (2002). Visualization of a Ran-GTP gradient in interphase and mitotic Xenopus egg extracts. *Science*, **295**, 2452–6.

[63] M. Caudron, G. Bunt, P. Bastiaens, and E. Karsenti (2005). Spatial coordination of spindle assembly by chromosome-mediated signaling gradients. *Science*, **309**, 1373–6.

[64] P. Kaláb, A. Pralle, E. Y. Isacoff, R. Heald, and K. Weis (2006). Analysis of a RanGTP-regulated gradient in mitotic somatic cells. *Nature*, **440**, 697–701.

[65] M. V. Nachury, T. J. Maresca, W. C. Salmon, C. M. Waterman-Storer, R. Heald, and K. Weis (2001). Importin beta is a mitotic target of the small GTPase Ran in spindle assembly. *Cell*, **104**, 95–106.

[66] C. Wiese, A. Wilde, M. S. Moore, S. A. Adam, A. Merdes, and Y. Zheng (2001). Role of importin-beta in coupling Ran to downstream targets in microtubule assembly. *Science*, **291**, 653–6.

[67] C. A. Schatz, R. Santarella, A. Hoenger, E. Karsenti, I. W. Mattaj, O. J. Gruss, and R. E. Carazo-Salas (2003). Importin alpha-regulated nucleation of microtubules by TPX2. *EMBO J*, **22**, 2060–70.

[68] T. A. Kufer, H. H. W. Silljé, R. Körner, O. J. Gruss, P. Meraldi, and E. A. Nigg (2002). Human TPX2 is required for targeting Aurora-A kinase to the spindle. *J Cell Biol*, **158**, 617–23.

[69] R. Bayliss, T. Sardon, I. Vernos, and E. Conti (2003). Structural basis of Aurora-A activation by TPX2 at the mitotic spindle. *Mol Cell*, **12**, 851–62.

[70] P. A. Eyers, E. Erikson, L. G. Chen, and J. L. Maller (2003). A novel mechanism for activation of the protein kinase Aurora A. *Curr Biol*, **13**, 691–7.

[71] N. Ozlü, M. Srayko, K. Kinoshita, B. Habermann, E. T. O'toole, T. Müller-Reichert, N. Schmalz, A. Desai, and A. A. Hyman (2005). An essential function of the C. elegans ortholog of TPX2 is to localize activated aurora A kinase to mitotic spindles. *Dev Cell*, **9**, 237–48.

[72] M. Giubettini, I. A. Asteriti, J. Scrofani, M. De Luca, C. Lindon, P. Lavia, and G. Guarguaglini (2011). Control of Aurora-A stability through interaction with TPX2. *J Cell Sci*, **124**, 113–22.

[73] O. J. Gruss, R. E. Carazo-Salas, C. A. Schatz, G. Guarguaglini, J. Kast, M. Wilm, N. Le Bot, I. Vernos, E. Karsenti, and I. W. Mattaj (2001). Ran induces spindle assembly by reversing the inhibitory effect of importin alpha on TPX2 activity. *Cell*, **104**, 83–93.

[74] M.-Y. Tsai, C. Wiese, K. Cao, O. Martin, P. Donovan, J. Ruderman, C. Prigent, and Y. Zheng (2003). A Ran signalling pathway mediated by the mitotic kinase Aurora A in spindle assembly. *Nat Cell Biol*, **5**, 242–8.

[75] A. Giesecke and M. Stewart (2010). Novel binding of the mitotic regulator TPX2 (target protein for Xenopus kinesin-like protein 2) to importin-alpha. *J Biol Chem*, **285**, 17628–35.

[76] H. Yokoyama, O. J. Gruss, S. Rybina, M. Caudron, M. Schelder, M. Wilm, I. W. Mattaj, and E. Karsenti (2008). Cdk11 is a RanGTP-dependent microtubule stabilization factor that regulates spindle assembly rate. *J Cell Biol*, **180**, 867–75.

[77] A. Arnaoutov, Y. Azuma, K. Ribbeck, J. Joseph, Y. Boyarchuk, T. Karpova, J. McNally, and M. Dasso (2005). Crm1 is a mitotic effector of Ran-GTP in somatic cells. *Nat Cell Biol*, **7**, 626–32.

[78] P. Bastiaens, M. Caudron, P. Niethammer, and E. Karsenti (2006). Gradients in the self-organization of the mitotic spindle. *Trends Cell Biol*, **16**, 125–34.

[79] B. Burke and J. Ellenberg (2002). Remodelling the walls of the nucleus. *Nat Rev Mol Cell Biol*, **3**, 487–97.

[80] E. Robbins and N. K. Gonatas (1964). The ultrastructure of a mammalian cell during the mitotic cycle. *J Cell Biol*, **21**, 429–63.

[81] J. Ellenberg, E. D. Siggia, J. E. Moreira, C. L. Smith, J. F. Presley, H. J. Worman, and J. Lippincott-Schwartz (1997). Nuclear membrane dynamics and reassembly in living cells: targeting of an inner nuclear membrane protein in interphase and mitosis. *J Cell Biol*, **138**, 1193–206.

[82] C. Zhang and P. R. Clarke (2000). Chromatin-independent nuclear envelope assembly induced by Ran GTPase in Xenopus egg extracts. *Science*, **288**, 1429–32.

[83] M. Hetzer, D. Bilbao-Cortés, T. C. Walther, O. J. Gruss, and I. W. Mattaj (2000). GTP hydrolysis by Ran is required for nuclear envelope assembly. *Mol Cell*, **5**, 1013–24.

[84] C. Zhang, J. R. A. Hutchins, P. Mühlhäusser, U. Kutay, and P. R. Clarke (2002). Role of importin-beta in the control of nuclear envelope assembly by Ran. *Curr Biol*, **12**, 498–502.

[85] T. C. Walther, P. Askjaer, M. Gentzel, A. Habermann, G. Griffiths, M. Wilm, I. W. Mattaj, and M. Hetzer (2003). RanGTP mediates nuclear pore complex assembly. *Nature*, **424**, 689–94.

[86] S. Uchida, T. Sekiguchi, H. Nishitani, K. Miyauchi, M. Ohtsubo, and T. Nishimoto (1990). Premature chromosome condensation is induced

by a point mutation in the hamster RCC1 gene. *Mol Cell Biol*, **10**, 577–84.

[87] M. Ohtsubo, R. Kai, N. Furuno, T. Sekiguchi, M. Sekiguchi, H. Hayashida, K. Kuma, T. Miyata, S. Fukushige, and T. Murotsu (1987). Isolation and characterization of the active cDNA of the human cell cycle gene (RCC1) involved in the regulation of onset of chromosome condensation. *Genes Dev*, **1**, 585–93.

[88] H. Nishitani, M. Ohtsubo, K. Yamashita, H. Iida, J. Pines, H. Yasudo, Y. Shibata, T. Hunter, and T. Nishimoto (1991). Loss of RCC1, a nuclear DNA-binding protein, uncouples the completion of DNA replication from the activation of cdc2 protein kinase and mitosis. *EMBO J*, **10**, 1555–64.

[89] P. R. Clarke, C. Klebe, A. Wittinghofer, and E. Karsenti (1995). Regulation of Cdc2/cyclin B activation by Ran, a Ras-related GTPase. *J Cell Sci*, **108 (Pt 3)**, 1217–25.

[90] O. Gavet and J. Pines (2010). Activation of cyclin B1-Cdk1 synchronizes events in the nucleus and the cytoplasm at mitosis. *J Cell Biol*, **189**, 247–59.

[91] L. Renault, N. Nassar, I. Vetter, J. Becker, C. Klebe, M. Roth, and A. Wittinghofer (1998). The 1.7 A crystal structure of the regulator of chromosome condensation (RCC1) reveals a seven-bladed propeller. *Nature*, **392**, 97–101.

[92] T. J. Stevens and M. Paoli (2008). RCC1-like repeat proteins: a pangenomic, structurally diverse new superfamily of beta-propeller domains. *Proteins*, **70**, 378–87.

[93] F. E. Hood and P. R. Clarke (2007). RCC1 isoforms differ in their affinity for chromatin, molecular interactions and regulation by phosphorylation. *J Cell Sci*, **120**, 3436–45.

[94] C. Klebe, H. Prinz, A. Wittinghofer, and R. S. Goody (1995). The kinetic mechanism of Ran–nucleotide exchange catalyzed by RCC1. *Biochemistry*, **34**, 12543–52.

[95] M. Köhler, C. Speck, M. Christiansen, F. R. Bischoff, S. Prehn, H. Haller, D. Görlich, and E. Hartmann (1999). Evidence for distinct substrate specificities of importin alpha family members in nuclear protein import. *Mol Cell Biol*, **19**, 7782–91.

[96] B. Talcott and M. S. Moore (2000). The nuclear import of RCC1 requires a specific nuclear localization sequence receptor, karyopherin alpha3/Qip. *J Biol Chem*, **275**, 10099–104.

[97] M. E. Nemergut and I. G. Macara (2000). Nuclear import of the Ran exchange factor, RCC1, is mediated by at least two distinct mechanisms. *J Cell Biol*, **149**, 835–50.

[98] J. R. A. Hutchins, W. J. Moore, F. E. Hood, J. S. J. Wilson, P. D. Andrews, J. R. Swedlow, and P. R. Clarke (2004). Phosphorylation regulates the dynamic interaction of RCC1 with chromosomes during mitosis. *Curr Biol*, **14**, 1099–104.

[99] H.-Y. Li and Y. Zheng (2004). Phosphorylation of RCC1 in mitosis is essential for producing a high RanGTP concentration on chromosomes and for spindle assembly in mammalian cells. *Genes Dev*, **18**, 512–27.

[100] R. D. Makde, J. R. England, H. P. Yennawar, and S. Tan (2010). Structure of RCC1 chromatin factor bound to the nucleosome core particle. *Nature*, **467**, 562–6.

[101] K. Luger, A. W. Mäder, R. K. Richmond, D. F. Sargent, and T. J. Richmond (1997). Crystal structure of the nucleosome core particle at 2.8 A resolution. *Nature*, **389**, 251–60.

[102] H. Seino, N. Hisamoto, S. Uzawa, T. Sekiguchi, and T. Nishimoto (1992). DNA-binding domain of RCC1 protein is not essential for coupling mitosis with DNA replication. *J Cell Sci*, **102**, 393–400.

[103] M. E. Nemergut, C. A. Mizzen, T. Stukenberg, C. D. Allis, and I. G. Macara (2001). Chromatin docking and exchange activity enhancement of RCC1 by histones H2A and H2B. *Science*, **292**, 1540–3.

[104] T. Chen, T. L. Muratore, C. E. Schaner-Tooley, J. Shabanowitz, D. F. Hunt, and I. G. Macara (2007). N-terminal alpha-methylation of RCC1 is necessary for stable chromatin association and normal mitosis. *Nat Cell Biol*, **9**, 596–603.

[105] C. E. S. Tooley, J. J. Petkowski, T. L. Muratore-Schroeder, J. L. Balsbaugh, J. Shabanowitz, M. Sabat, W. Minor, D. F. Hunt, and I. G. Macara (2010). NRMT is an alpha-N-methyltransferase that methylates RCC1 and retinoblastoma protein. *Nature*, **466**, 1125–8.

[106] W. Moore, C. Zhang, and P. R. Clarke (2002). Targeting of RCC1 to chromosomes is required for proper mitotic spindle assembly in human cells. *Curr Biol*, **12**, 1442–7.

[107] H. Y. Li, D. Wirtz, and Y. Zheng (2003). A mechanism of coupling RCC1 mobility to RanGTP production on the chromatin in vivo. *J Cell Biol*, **160**, 635–44.

[108] D. Bilbao-Cortés, M. Hetzer, G. Längst, P. B. Becker, and I. W. Mattaj (2002). Ran binds to chromatin by two distinct mechanisms. *Curr Biol*, **12**, 1151–6.

[109] C.-H. Wong, H. Chan, C.-Y. Ho, S.-K. Lai, K.-S. Chan, C.-G. Koh, and H.-Y. Li (2009). Apoptotic histone modification inhibits nuclear transport by regulating RCC1. *Nat Cell Biol*, **11**, 36–45.

[110] D. Axelrod, D. E. Koppel, J. Schlessinger, E. Elson, and W. W. Webb (1976). Mobility measurement by analysis of fluorescence photobleaching recovery kinetics. *Biophys J*, **16**, 1055–69.

[111] R. D. Phair and T. Misteli (2000). High mobility of proteins in the mammalian cell nucleus. *Nature*, **404**, 604–9.

[112] B. L. Sprague, R. L. Pego, D. A. Stavreva, and J. G. McNally (2004). Analysis of binding reactions by fluorescence recovery after photobleaching. *Biophys J*, **86**, 3473–95.

[113] F. Müller, P. Wach, and J. G. McNally (2008). Evidence for a common mode of transcription factor interaction with chromatin as revealed by improved quantitative fluorescence recovery after photobleaching. *Biophys J*, **94**, 3323–39.

[114] G. H. Patterson and J. Lippincott-Schwartz (2002). A photoactivatable GFP for selective photolabeling of proteins and cells. *Science*, **297**, 1873–7.

[115] J. Beaudouin, F. Mora-Bermúdez, T. Klee, N. Daigle, and J. Ellenberg (2006). Dissecting the contribution of diffusion and interactions to the mobility of nuclear proteins. *Biophys J*, **90**, 1878–94.

[116] E. L. Elson and D. Magde (1974). Fluorescence correlation spectroscopy. I. Conceptual basis and theory. *Biopolymers*, **13**, 1–27.

[117] R. Rigler, Ü. Mets, J. Widengren, and P. Kask (1993). Fluorescence correlation spectroscopy with high count rate and low background: analysis of translational diffusion. *European Biophysics Journal*, **22**, 169–175.

[118] R. Brock (2005). Fluorescence Correlation Spectroscopy in Cell Biology. In M. Hof, R. Hutterer, and V. Fidler, eds., *Fluorescence Spectroscopy in Biology*, vol. 3 of *Springer Series on Fluorescence*, pp. 245–262. Springer Berlin Heidelberg.

[119] O. Krichevsky and G. Bonnet (2002). Fluorescence correlation spectroscopy: the technique and its applications. *Reports on Progress in Physics*, **65**, 251–297.

[120] P. Schwille, F. J. Meyer-Almes, and R. Rigler (1997). Dual-color fluorescence cross-correlation spectroscopy for multicomponent diffusional analysis in solution. *Biophys J*, **72**, 1878–86.

[121] L. Cassimeris and E. D. Salmon (1991). Kinetochore microtubules shorten by loss of subunits at the kinetochores of prometaphase chromosomes. *J Cell Sci*, **98**, 151–8.

[122] C. I. Maeder, M. A. Hink, A. Kinkhabwala, R. Mayr, P. I. H. Bastiaens, and M. Knop (2007). Spatial regulation of Fus3 MAP kinase activity through a reaction-diffusion mechanism in yeast pheromone signalling. *Nat Cell Biol*, **9**, 1319–26.

[123] A. Kinkhabwala and P. I. H. Bastiaens (2010). Spatial aspects of intracellular information processing. *Curr Opin Genet Dev*, **20**, 31–40.

[124] D. Bhattacharya, A. Mazumder, S. A. Miriam, and G. V. Shivashankar (2006). EGFP-tagged core and linker histones diffuse via distinct mechanisms within living cells. *Biophys J*, **91**, 2326–36.

[125] A. Michelman-Ribeiro, D. Mazza, T. Rosales, T. J. Stasevich, H. Boukari, V. Rishi, C. Vinson, J. R. Knutson, and J. G. McNally (2009). Direct measurement of association and dissociation rates of DNA binding in live cells by fluorescence correlation spectroscopy. *Biophys J*, **97**, 337–46.

[126] U. Meseth, T. Wohland, R. Rigler, and H. Vogel (1999). Resolution of fluorescence correlation measurements. *Biophys J*, **76**, 1619–31.

[127] J. Elf, G.-W. Li, and X. S. Xie (2007). Probing transcription factor dynamics at the single-molecule level in a living cell. *Science*, **316**, 1191–4.

[128] J. Gorman, A. J. Plys, M.-L. Visnapuu, E. Alani, and E. C. Greene (2010). Visualizing one-dimensional diffusion of eukaryotic DNA repair factors along a chromatin lattice. *Nat Struct Mol Biol*, **17**, 932–8.

[129] S. E. Halford and J. F. Marko (2004). How do site-specific DNA-binding proteins find their targets? *Nucleic Acids Res*, **32**, 3040–52.

[130] R. T. Koerber, H. S. Rhee, C. Jiang, and B. F. Pugh (2009). Interaction of transcriptional regulators with specific nucleosomes across the Saccharomyces genome. *Mol Cell*, **35**, 889–902.

[131] A. Abu-Arish, P. Kalab, J. Ng-Kamstra, K. Weis, and C. Fradin (2009). Spatial distribution and mobility of the Ran GTPase in live interphase cells. *Biophys J*, **97**, 2164–78.

[132] B. N. Kholodenko, J. B. Hoek, and H. V. Westerhoff (2000). Why cytoplasmic signalling proteins should be recruited to cell membranes. *Trends Cell Biol*, **10**, 173–8.

[133] B. M. Fontoura, G. Blobel, and N. R. Yaseen (2000). The nucleoporin Nup98 is a site for GDP/GTP exchange on ran and termination of karyopherin beta 2-mediated nuclear import. *J Biol Chem*, **275**, 31289–96.

[134] P. Fanara, M. R. Hodel, A. H. Corbett, and A. E. Hodel (2000). Quantitative analysis of nuclear localization signal (NLS)-importin alpha interaction through fluorescence depolarization. Evidence for auto-inhibitory regulation of NLS binding. *J Biol Chem*, **275**, 21218–23.

[135] Y. Hao and I. G. Macara (2008). Regulation of chromatin binding by a conformational switch in the tail of the Ran exchange factor RCC1. *J Cell Biol*, **182**, 827–36.

[136] A. Arnaoutov and M. Dasso (2005). Ran-GTP regulates kinetochore attachment in somatic cells. *Cell Cycle*, **4**, 1161–5.

[137] J. Sambrook, E. Fritsch, and T. Maniatis (1989). *Molecular Cloning. A Laboratory Manual.* Cold Spring Harbor Laboratory Press.

[138] C. L. Fisher and G. K. Pei (1997). Modification of a PCR-based site-directed mutagenesis method. *Biotechniques*, **23**, 570–1, 574.

[139] F. Sanger, S. Nicklen, and A. R. Coulson (1977). DNA sequencing with chain-terminating inhibitors. *Proc Natl Acad Sci U S A*, **74**, 5463–7.

[140] D. Gerlich, J. Beaudouin, B. Kalbfuss, N. Daigle, R. Eils, and J. Ellenberg (2003). Global chromosome positions are transmitted through mitosis in mammalian cells. *Cell*, **112**, 751–64.

[141] P. Kapusta (2009). *Absolute Diffusion Coefficients: Compilation of Reference Data for FCS Calibration*. PicoQuant GmbH, Berlin.

[142] G. Rabut and J. Ellenberg (2004). Automatic real-time three-dimensional cell tracking by fluorescence microscopy. *J Microsc*, **216**, 131–7.

Abbreviations

ATP	adenosine triphosphate
DNA	deoxyribonucleic acid
EGFP	enhanced green fluorescent protein
ER	endoplasmic reticulum
FCS	fluorescence correlation spectroscopy
FCCS	fluorescence crosscorrelation spectroscopy
FG Nup	phenyl-glycine rich nucleoporin
FRAP	fluorescence recovery after photobleaching
FRET	fluorescence resonance transfer
GAP	GTPase activating protein
GEF	guanine nucleotide exchange factor
GDP	guanosine diphosphate
G-protein	guanine nucleotide binding protein
GTP	guanosine triphosphate
GTPase	guanosine triphosphate hydrolase
H1	histone H1
H2B	histone H2B
MT	microtubule
NE	nuclear envelope
NLS	nuclear localization sequence
NPC	nuclear pore complex
NTF	nuclear transport factor
NT-GFP	the first 27 amino acid residues of RCC1 γ fused to GFP
Nup	nucleoporin
paGFP	photoactivatable green fluorescent protein
RCC1	regulator of chromosome condensation 1
RCC1Δ27	RCC1 γ lacking its first 27 amino acid residues
SAF	spindle assembly factor
WT	wildtype

Acknowledgments

I would like to thank Prof. Philippe Bastiaens for the opportunity to work in his laboratory.

I thank Prof. Alfred Wittinghofer for being the second examiner of this thesis.

I was lucky to receive help and supervision from several people. These were Piet Lommerse, who introduced me to FCS, Ali Kinkhabwala who made crucial suggestions on how to analyze FCS data, and Hernan Grecco, who supported me in data analysis and programming. I also want to thank all the lab's technicians, from whom I've received a great deal of support, especially Kirsten Michel, Hendrike Schütz, Jutta Luig, Petra Glitz, and Anette Langerak.

For generously providing reagents, I thank Jan Ellenberg and Nathalie Daigle (EMBL Heidelberg) for RCC1 and Histone H2B coding sequences, Alfred Wittinghofer, Ingrid Vetter, Carolin Körner and Doro Vogt for various DNA constructs, most importantly human Ran, Leif Dehmelt for mCherry-Tubulin, and Mark Hink for the EGFP-p38-mCherry construct.

I thank Astrid Krämer and Tanja Forck for keeping the boss (and everything else) well organized.

For working together, having lunch, sharing gossip, enjoying football, mastering rock climbing, studying dynamomorphotopological aspects of living systems, and occasionally having a laugh, I thank all the members of the department II and co-workers at the MPI Dortmund, especially and in no particular order Ola Sabet, Jian Hou, Kirstin Walther, Justine Mondry, Thies Klüßendorf, Johann Jarzombek, Christina Hecker, Constantin Brinkmann, Björn Papke, Pedro Roda-Navarro, Rahul Ravindran, Eulashini Chuntharpursat, Shehab Ismail, Christian Schmees, Malte Schmick, Lisa Karajannis, Sven Müller, Márton Gelléri, Maja Sinn, and Sven Fengler.

Special thanks to Ola and Hernan for their helpful comments on this manuscript.

Von ganzem Herzen danke ich meinen Eltern und Verena.